Copyright

by

Gholamreza Garmeh

2010

The Dissertation Committee for Gholamreza Garmeh Certifies that this is the approved version of the following dissertation:

Investigation of Scale Dependent Dispersivity and Its Impact on Upscaling Miscible Displacements

Committee:

Russell T. Johns, Supervisor

Larry W. Lake

Kamy Sepehrnoori

Steven L. Bryant

James W. Jennings

Investigation of Scale Dependent Dispersivity and Its Impact on Upscaling Miscible Displacements

by

Gholamreza Garmeh, B.S.; M.S.

Dissertation

Presented to the Faculty of the Graduate School of
The University of Texas at Austin
in Partial Fulfillment
of the Requirements
for the Degree of

Doctor of Philosophy

The University of Texas at Austin
May 2010

Dedication

To my devoted parents for their endless love and support

Acknowledgements

I would like to thank my supervisor Dr. Russell T. Johns for his support, guidance and encouragement throughout my research. I have learned a lot from his insightful questions, enthusiastic observations and vast knowledge. I also thank him for encouraging independent thinking.

I would like to extend my appreciation to all my committee members, Dr. Larry W. Lake, Dr. Kamy Sepehrnoori, Dr. Steve L. Bryant and Dr. James W. Jennings for taking time to review my dissertation and for their guidance and comments, which had a significant impact on the progress of this project.

I would like to acknowledge the staff in our department: Roger Terzian, Joanna Castillo, Cheryl Kruzie, Mary Pettengill and Nina Schenck.

I also extend my appreciation to the member of our gas flooding research group, Meghdad Roshanfekr, Kaveh Ahmadi, Ryosuke Okuno, Khyati Rai, Ashwin Venkatraman, Gurpreet Singh, Saeedeh Mohebbinia, Ali Moeinfar and Olaoluwa Adepoju for friendship and valuable discussions that we had.

Special thanks to my friends and fellow graduate students Abraham John and Raman Jha for their technical discussion and suggestion on dispersion.

It has been a great pleasure working with several colleagues. I would like to thank my colleague and friends at the department of petroleum and geosystem engineering, specially Abdoljalil Varavei, Arash Dahi, Peyman Pourafshary, Yosef Ghomian, Farhad Tarahom, Morteza Sayarpour, Rohollah Abdolahpour, Maryam Mousavi, Mohabbat Ahmadi, Siyavash Motealleh, Nariman Fathi, Waleed

Fazelipour, Farshad Lalehrokh, Rouzbeh Ghanbarnezhad, Javad Behseresht, Ehsan Saadatpour, Mehdi Haghshenas, Alireza Mollaei, Ali Goudarzi, Medi Shirdel, Amin Ettehad, Amirreza Rahmani, Abdolhamid Hadibeik, Zoya Heidari and Mohsen Taghavifar.

Finally, I would like to thank my parents, sisters and brother for their love, affection and patience during this study. It would not have been possible without their support.

I also acknowledge the funding of this project provided by the US Department of Energy (DOE grant No. DE-PS26-04NT15450-3F) and the member companies of the Gas Flooding Research Group.

Investigation of Scale Dependent Dispersivity and Its Impact on Upscaling Miscible Displacements

Publication No._____________

Gholamreza Garmeh, Ph.D.
The University of Texas at Austin, 2010

Supervisor: Russell T. Johns

Mixing of miscible gas with oil in a reservoir decreases the effective strength of the gas, which can adversely affect miscibility and recovery efficiency. The mixing that occurs in a reservoir, however, is widely debated and often ignored in reservoir simulation, where very large grid blocks are used. Large grid blocks create artificially large mixing that can cause errors in predicted oil recovery.

Reservoir mixing, or dispersion, is caused by diffusion of particles across streamlines of varying velocities. Mixing is enhanced by any mechanism that increases the area of contact between the gas and the oil, thereby allowing the effects of diffusion to be magnified. This is, in essence, the cause of scale-dependent dispersion. The contact area grows primarily because of variations in streamlines and their velocities around grains and through layers of various permeabilities (heterogeneity). Mixing can also be enhanced by crossflow, such as that caused by gravity and by the effects of other neighboring wells.

This dissertation focuses on estimation of the level of effective local mixing at the field scale and its impact on oil recovery from miscible gas floods. Pore-level simulation was performed using the Navier-Stokes and convection-diffusion equations to examine the origin of scale dependent dispersion. We then estimated dispersivity at the macro scale as a function of key scaling groups in heterogeneous reservoirs. Lastly, we upscaled grid blocks to match the level of mixing at the pattern scale. Once the contact area ceases to grow with distance traveled, dispersion has reached its asymptotic limit. This generally occurs when the fluids are well mixed in transverse direction.

We investigated a variety of pore-scale models to understand the nature of scale dependency. From the pore-scale study, we found that reservoir mixing or dispersion is caused by diffusion of particles across streamlines. Diffusion can be significantly enhanced if the surface area of contact between the reservoir and injected fluid are increased as fluids propagate through the reservoir. Echo and transmission dispersivities are scale dependent. They may or may not reach an asymptotic limit depending on the scale of heterogeneities encountered. The scale dependence results from an increase in the contact area between solute (gas) and resident fluid (oil) as heterogeneities are encountered, either at the pore or pattern-scale.

The key scaling groups for first-contact miscible (FCM) flow are derived and their impact on mixing is analyzed. We examine only local mixing, not apparent mixing caused by variations in streamline path lengths (convective spreading). Local mixing is important because it affects the strength of the injected fluid, and can cause an otherwise multicontact miscible (MCM) flood to become immiscible.

We then showed how to upscale miscible floods considering reservoir mixing. The sum of numerical dispersion and physical dispersion associated with the reservoir heterogeneities, geometry and fluid properties must be equal at both the fine- and large-scales. The maximum grid-block size allowed in both the x- and z-directions is determined from the scaling groups. Small grid-blocks must be used for reservoirs with uncorrelated permeabilities, while larger grid blocks can be used for more layered reservoirs. The predicted level of mixing for first-contact miscible floods can be extended with good accuracy to multicontact miscible (MCM) gas floods.

Table of Contents

List of Tables

List of Figures

Chapter 1: Introduction and Literature Review

1.1 BACKGROUND

Dispersion (mixing process) in porous media is the dilution process that is caused by molecular diffusion and mechanical spreading. Molecular diffusion is the phenomenon of mass transport of a component in the direction of decreasing concentration within a single phase. Diffusion is characterized by a random motion of molecules when two miscible fluids are in contact. The diffusion model for diffusive flux was first proposed by Fick (1855) and is analogous to Fourier's heat transport, also known as Fickian diffusion. According to Fick's first law, the diffusive flux for component *i* is given by

$$J_i = -D_i^o \nabla C_i \,, \tag{1.1}$$

where D_i^o is the molecular diffusion coefficient of component *i*, and C_i is the concentration of component *i*. Molecular diffusion is a function of pressure, temperature and composition (Sigmund, 1976).

For the case of a porous medium, the diffusive flux is based on the path length and cross-sectional area available for diffusion. To account for this apparent diffusion, porosity and formation factor of corresponding porous media are incorporated analogous to the electrical conductivity. Perkins and Johnston (1963) defined effective diffusivity for porous media by

$$J_i = -\frac{D_i^o}{\phi F} \nabla C_i , \tag{1.2}$$

where F is the formation resistivity factor and ϕ is the formation porosity. The product (ϕF) is the effective tortuous path that a particle must travel in porous media and is called tortuosity. Effective diffusion in porous media has also been investigated by various researchers (Sorbie and Tomlinson 1993; Boving and Grathwohl, 2001).

Molecular diffusion coefficients are of the range of 10^{-7} m^2/s for gases to 10^{-9} m^2/s for liquids (Sigmund, 1976; da Silva and Belery, 1989). For multi-component systems molecular diffusion depends on the phase where diffusion takes place. In gas systems effective diffusion depends on the component molar density; however, for liquid mixtures, effective molecular diffusion depends on the phase viscosity and molar density (Wilke and Chang 1955; Sigmund, 1976; da Silva and Belery, 1989; Riazi and Whitson 1993).

1.1.1 Hydrodynamic Dispersion in Porous Media

Hydrodynamic dispersion is defined as the combination of molecular diffusion and mechanical dispersion for dispersive transport in porous media (Aris 1959; Bear, 1972). Mechanical dispersion is the spreading of components in a single phase within a porous medium caused by velocity variations (Bear, 1972). Velocity fluctuations in porous media are a consequence of flow through different pore geometries, parabolic velocity distributions for viscous flow through a pore, and variations in flow direction with respect to the bulk flow. Figure 1.1 schematically illustrates hydrodynamic dispersion owing to mechanical dispersion and molecular diffusion (Bear and Bachmat, 1990).

Bear (1969) provides several physical and chemical phenomena that cause hydrodynamic dispersion in porous media such as the impact of external forces on liquids, complex structure of pore geometry, molecular diffusion, flow pattern variations owing to change in fluid density and viscosity, chemical and physical process within the phase, and fluid and solid phase interactions. Greenkorn (1983) presents detailed mechanisms that cause dispersion in porous media. They are:

1) Molecular diffusion due to random motion of molecules in miscible flow
2) Mixing because of obstructions
3) Autocorrelation in flow conductivity
4) Recirculation caused by local regions of reduced pressure
5) Dispersion due to non-idealities in porous media
6) Hydrodynamic dispersion due to velocity fluctuation in porous media
7) Eddies due to turbulent flow within channels in porous media
8) Dead-end pores that increase molecular diffusion
9) Adsorption of solute concentration onto pore walls

The mechanisms described by Bear (1969) and Greenkorn (1983) confirm that, when a solute flow through a porous medium, mixing is greater than what would be estimated by diffusion alone. This additional mixing is caused by any mechanism that enhances fluid surface contact area. Heller (1972) shows the influence of diffusion on reservoir mixing and its impact on flow reversibility.

1.1.2 Dispersive Flux

According to the Fickian representation of solute transport in porous media, dispersive flux in a permeable medium is analogous to diffusive flux given in Equation (1.1).

$$J_i = -\vec{\vec{D}}_i \cdot \nabla C_i, \tag{1.3}$$

where $\vec{\vec{D}}_i$ is the dispersion coefficient tensor of component *i*, and C_i is the concentration of component *i*. The negative sign indicates that mass flux is in the direction of decreasing concentration. The dispersion coefficient includes both molecular diffusion and mechanical spreading (Aronofsky and Heller 1957). Klinkenberg (1951) discussed the analogy between diffusion and electrical conductivity in porous media. The molecular diffusion part of dispersion in porous media is given as

$$D_i = \frac{D_i^o}{\phi F} = \frac{D_i^o}{\tau} \tag{1.4}$$

and the mechanical spreading part (local velocity gradients) of dispersion is presented as:

$$D_i = \frac{D_p v}{2}, \tag{1.5}$$

where D_p is the grain diameter and v is the pore velocity.

Assuming that two terms are additive, the total dispersion in porous media is expressed as:

$$D_i = \frac{D_i^o}{\phi F} + \frac{D_p v}{2}. \tag{1.6}$$

Equation (1.6) is accurate for uniform and homogeneous grain packing porous media. Real porous media are more complicated than uniform grain packs. Perkins and Johnston (1963) showed that an inhomogeneity factor is required to correlate with experimental measurements because presence of more than one phase, unequal viscosities and densities, and turbulent flow will increase the longitudinal dispersion.

Considering inhomogeneity factors, for one-dimensional flow, the longitudinal dispersion coefficient D_i, is presented as (Perkins and Johnston, 1963):

$$\frac{D_i}{D_i^o} = C_1 + C_2 \left(\frac{D_p v}{D_i^o} \right)^{\beta}, \tag{1.7}$$

where C_1, C_2 and β are properties of the porous media and flow regime. For very small velocities, the second term in the above equation is negligible and dispersion is proportional to molecular diffusion. Thus mixing is dominated by molecular diffusion; however for greater velocities the second term in equation (1.7) becomes significant. Perkins and Johnston (1963) showed through experiments that β is in the range of 1.0 to 1.25.

If interstitial velocity is greater than 3 cm/day, the second term in equation (1.7) dominates the first term and the longitudinal dispersion coefficient can be written as (Lake, 1989):

$$D_l = \frac{D_o}{\phi F} + C_2 \left(\frac{D_p v}{D_o} \right)^{\beta} D_o \approx \alpha_l v, \tag{1.8}$$

where α_l is the longitudinal dispersivity. The longitudinal dispersivity (α_l) quantifies the rate of mixing of an injected gas with reservoir oil. The absence of molecular diffusion term in equation (1.8) does not imply that diffusion is negligible in miscible flow. In fact, without diffusion, there is no mixing in porous media.

1.1.3 Dispersion Tensor

Bear (1961) verified that dispersion has a tensorial form by observing the dissipation of tracer from a point source. The dispersion tensor depends on the geometry of the porous media, flow velocity, and molecular diffusion (Bear, 1979). The general form of the dispersion coefficient tensor is:

$$\vec{\vec{D}}_{ij} = \begin{bmatrix} D_{ij}^{xx} & D_{ij}^{xy} & D_{ij}^{xz} \\ D_{ij}^{yx} & D_{ij}^{yy} & D_{ij}^{yz} \\ D_{ij}^{zx} & D_{ij}^{zy} & D_{ij}^{zz} \end{bmatrix}. \tag{1.9}$$

where $\vec{\vec{D}}_{ij}$ is the dispersion tensor, and each component of the dispersion tensor is defined as (Bear 1972):

$$D_{ij}^{mn} = \frac{D_{ij}^{o}}{\phi F_j S_j}\delta_{mn} + \alpha_{tj}\frac{|u_j|}{\phi S_j}\delta_{mn} + \frac{(\alpha_{lj} - \alpha_{tj})}{\phi S_j |u_j|} u_{mj} u_{nj}, \tag{1.10}$$

where, m and n are the spatial directions, and

D_{ij}^{o} = Molecular diffusion coefficient of component i in phase j

F_j = Formation resistivity factor for phase j

S_j = Saturation of phase j

α_{lj} = Longitudinal dispersivity of phase j

α_{tj} = Transverse dispersivity of phase *j*

$\boldsymbol{u}_j$ = Velocity of phase *j*

where,

$$\left|u_j\right| = \sqrt{u_{xj}^2 + u_{yj}^2 + u_{zj}^2} \tag{1.11}$$

and,

$$\delta_{mn} = \begin{cases} 1 & for\ m = n \\ 0 & for\ m \neq n \end{cases} \tag{1.12}$$

Details about the dispersion tensor and numerical dispersion are given in Appendix C.

1.1.4 Flow and Transport in Porous Media

Convection-Dispersion Equation

The convection-dispersion equation (CDE) is a simplified form of the general conservation equation for multiphase multi-component flow. The convection dispersion equation describes the overall mass transport and reservoir mixing in porous media for single phase flow, equal density, equal viscosity, and without reaction term.

General mass balance equation without reaction and generation terms is given by:

$$\frac{\partial}{\partial t}(\phi\sum_{j=1}^{n_p}\sum_{i=1}^{n_c} x_{ij}\rho_j S_j) + \nabla\cdot(\sum_{j=1}^{n_p}\sum_{i=1}^{n_c} x_{ij}\rho_j \vec{u}_j) - \nabla\cdot(\phi\sum_{j=1}^{n_p}\sum_{i=1}^{n_c} \vec{\vec{D}}_{ij}\cdot\nabla\rho_j x_{ij}) = 0 \text{ ,} \tag{1.13}$$

where x_{ij} is the mole fraction of component *i* in phase *j*, and ρ_j is the mass density of phase j. According to the convection dispersion equation assumptions, $n_c = 1$, $n_p = 1$, and $x_{ij}\rho_j = C_{ij} = C$; thus, the conservation equation is reduced to

$$\frac{\partial}{\partial t}\phi C + \nabla \cdot uC - \nabla \cdot \phi \vec{\vec{D}}(\nabla \cdot C) = 0 . \tag{1.14}$$

For 1-D solute transport in porous media the convection dispersion equation (CDE) is in the form of

$$\phi \frac{\partial C}{\partial t} + u \frac{\partial C}{\partial x} = \phi D_l \frac{\partial^2 C}{\partial x^2} , \tag{1.15}$$

where $C(x,t)$ is the solute concentration, and D_l is the longitudinal dispersion coefficient. CDE assumes incompressible fluid in porous media, no volume change upon mixing and spatially constant porosity.

In dimensionless form, CDE is written as:

$$\frac{\partial C_D}{\partial t_D} + \frac{\partial C_D}{\partial x_D} = \left[\frac{1}{N_{pe}} \right] \frac{\partial^2 C_D}{\partial x_D^2} . \tag{1.16}$$

Dimensionless parameters for equation (1.16) are given by

$$C_D = \frac{C - C_I}{C_J - C_I} , \tag{1.16-a}$$

$$t_D = \frac{ut}{\phi L} , \tag{1.16-b}$$

$$x_D = \frac{x}{L} , \tag{1.16-c}$$

and,

$$N_{Pe} = \frac{uL}{\phi D_l}. \tag{1.16-d}$$

where C_D is the dimensionless mass concentration normalized to the injection concentration, t_D is the dimensionless time (pore volume injected), x_D is the dimensionless distance traveled, and N_{Pe} is the Peclet number. The Peclet number is the ratio of the characteristic time for dispersive transport of a particle in the longitudinal direction to convective transport in the same direction. Thus for large Peclet number (low dispersion coefficients or high velocities) convective transport dominates dispersive mixing and for low Peclet number (high dispersion coefficients or low velocities) dispersive mixing dominates convective transport.

Analytical Solution of CDE

Many analytical solutions are possible for one-dimensional CDE depending on the initial and boundary conditions. The most common solution is for a medium with semi-infinite boundary condition. The boundary conditions for a semi-infinite model are

$$\begin{aligned} &C_D(x_D,0)=0 \quad at \qquad x_D \ge 0 \\ &C_D(\infty,t_D)=0 \quad at \qquad t_D \ge 0 \\ &C_D(0,t_D)=1 \quad at \qquad t_D \ge 0. \end{aligned}$$

The analytical solution of Eq. (1.16) combined with the above B.C. is (Lake, 1989)

$$C_D(x_D, t_D) = \frac{1}{2} erfc\left(\frac{x_D - t_D}{2\sqrt{\frac{t_D}{N_{Pe}}}} \right) + \frac{e^{x_D N_{Pe}}}{2} erfc\left(\frac{x_D + t_D}{2\sqrt{\frac{t_D}{N_{Pe}}}} \right). \tag{1.17}$$

Here *erfc* is the complementary error function given by:

$$erfc(x) = 1 - erf(x)$$

and, (1.18)

$$erf(x) = \frac{2}{\sqrt{\pi}} \int_0^x e^{-x^2} dx$$

The second term in equation (1.17) is negligible for large t_D or x_D. The analytical solution to the CDE for injection of a tracer of fixed volume is

$$C_D = \frac{1}{2}\left[erf\left(\frac{x_D - (t_D - t_{Ds})}{2\sqrt{\frac{(t_D - t_{Ds})}{N_{Pe}}}} \right) - erf\left(\frac{x_D - t_D}{2\sqrt{\frac{t_D}{N_{Pe}}}} \right) \right], \tag{1.19}$$

where t_{Ds} is the pore volumes of the injected slug.

1.1.5 Echo and Transmission Dispersions

Depending on the method of measurement, scale of observation, and flow direction, three different types of dispersion can occur in a permeable medium (see Fig. 1.2). Echo dispersion is defined as the reservoir mixing that is observed when flow is injected from an injector and is produced from the same injector after flow reversal. Transmission dispersion is defined as the observed dissipation when a tracer is injected from one end of a reservoir and is produced from the other end (interwell tracer test). That is, transmission dispersion is obtained when the fluid is transmitted through the reservoir without flow reversal.

Local dispersion is defined as the reservoir mixing that is observed from concentration history at a point or grid block in a permeable medium, where velocity fluctuations and multi-dimensional spreading does not impact reservoir mixing.

In the following sections we present echo and transmission dispersivities for various permeable media and discuss its significance. There is no fluid drift caused by other wells in all cases.

Homogeneous permeable media

In a homogeneous reservoir, echo dispersivity is equal to the longitudinal dispersivity. Echo dispersivity is the measure of mixing due to pore-scale heterogeneity of the porous medium and it remains constant with distance traveled (Mahadevan *et al.*, 2003).

Correlated heterogeneous permeable media

Consider a set of particles that are released at time zero from a source. Particles take many jumps based on discrete time step sizes to arrive to their destination point at time t. In case of correlated heterogeneous porous medium, each particle's jump depends on its previous jump. Thus when flow is reversed, particles do not take the previous path; consequently, echo and transmission dispersivities are not equal (Mahadevan *et al.*, 2003). The reversal of flow cancels out convective spreading owing to velocity variation and only retains dispersive mixing, which is not reversible.

Transmission dispersion includes both convective spreading caused by velocity variation and dispersive mixing. Dispersive mixing is caused by molecular diffusion and is enhanced by microscopic and macroscopic heterogeneity of the porous medium. In this case, transmission dispersivity is larger than echo dispersivity.

Layered permeable media

Layered permeable medium is a limiting case of correlated heterogeneous porous media. In this case, transport properties perfectly correlate in the bulk flow direction and are perfectly uncorrelated in the perpendicular direction. Assuming no transverse dispersion (no transverse movement), jumps that a particle takes are identical to jumps taken to reach that point, and the movement of each particle across the medium depends on the layer's permeability variation.

When flow is reversed each particle takes the same path and reaches the inlet at the same time. Flow reversal cancels out the variation of concentration owing to velocity variations across a cross section leaving contributions only due to mixing within each layer. Echo dispersivity is similar to longitudinal dispersivity of a homogeneous medium whereas transmission dispersivity is larger than echo dispersivity.

Effect of transverse dispersion

The main effect of transverse dispersion in porous media is to equalize concentrations in the transverse direction with respect to the bulk flow (Lake and Hirasaki, 1981). The effect of transverse dispersion in heterogeneous porous media is analogous to the effect of molecular diffusion observed in Taylor's dispersion theory (Leroy *et al.*, 1992; Auriault and Adler, 1995). In layered porous media, transverse dispersion tends to equalize concentration variations caused by velocity variations and may or may not become Fickian depending on the contrast between layers permeabilities, transverse dispersion coefficient and distance traveled (Lake and Hirasaki, 1981; Garmeh *et al.*, 2009). In this case, echo dispersivity is larger than the longitudinal dispersivity of a homogeneous medium. Once dispersion becomes Fickian, echo and transmission dispersivities are equal (Rigord *et al.*, 1990).

Field and laboratory-scale echo dispersion

Numerous studies have investigated echo dispersivity at the field and laboratory-scale. Hulin and Plona (1989) performed laboratory echo dispersion tests to investigate the reversibility of echo dispersion. They found that in homogeneous porous media, echo dispersion is the same as transmission dispersion at all Peclet numbers, and dispersion is completely irreversible. In a heterogeneous medium, echo dispersion is partially reversible and its magnitude is less than transmission dispersion. The irreversibility of dispersion corresponds to the combined effect of heterogeneity and molecular diffusion. Pickens and Grisak (1981) investigated echo and local dispersion at the field- and laboratory-scale, and concluded that dispersivities are scale dependent. Their measurements show that local dispersivities are greater than laboratory scale. This was attributed to greater inhomogeneity (lamination within individual layers) than at core scale. They also showed that echo dispersivities are scale dependent and are greater than local dispersivities mainly because of transverse migration of tracer between layers (crossflow). Mahadevan *et al.* (2003) showed that dispersivities obtained from single-well tracer test (SWTT) data (Majoros and Dean, 1980) are scale dependent and agree with the published trend of the longitudinal dispersivities by Arya *et al.* (1988). They showed through simulations that local dispersivities are always less than transmission dispersivities and greater than echo dispersivities depending on the amount of heterogeneity, the autocorrelation structure of the permeability field, and vertical permeability.

1.2 DISPERSION IN FIELD SCALE POROUS MEDIA

Field and experimental dispersivities at microscopic and macroscopic scales are generally measured by matching the concentration history with the solution of the one-dimensional convection-dispersion equation. At well pattern scale, a conservative tracer is injected into the reservoir and is measured at a production well. This concentration profile is matched with the solution of one-dimensional convection-dispersion equation by varying the dispersivity. Measured dispersivity from interwell tracer tests is therefore called field-scale transmission dispersivity.

Dispersivities measured at the pore-scale from core-flood experiments are owing to microscopic heterogeneities and tortuosity of the permeable media (Bear, 1972; Sternberg *et al.*, 1996). The measured dispersivities are in the range of *0.1* to *10 mm* (see Fig. 1.3); however, dispersivities measured at field-scale are much larger than core-scale by two to four orders of magnitude. This fact indicates that field-scale dispersivities are caused by macroscopic heterogeneities, layering and crossflow rather than microscopic heterogeneity (Lake and Hirasaki, 1981; Pickens and Grisak, 1981a,b; Gelhar *et al.*, 1992; Sternberg and Greenkorn, 1994).

Arya *et al.* (1988) has collected various field and laboratory measured data of dispersivity versus distance traveled as shown in Figure 1.3. They presented a trend for the field and laboratory-scale transmission dispersivities as a function of traveled distance.

For the field-scale, the longitudinal transmission dispersivity is given by

$$\alpha_l = 0.299L^{0.755} \tag{1.20}$$

whereas for laboratory and field-scale measured data, the longitudinal transmission dispersivity is

$$\alpha_l = 0.44L^{1.13} \tag{1.21}$$

where L is the length traveled. The trend in Figure 1.3 indicates that transmission dispersivity increases with distance traveled (Freeze and Cherry, 1979; Arya *et al.*, 1988; Gelhar *et al.*, 1992; Gelhar, 1993); however, it is difficult to distinguish if dispersivity increases with distance traveled indefinitely or if it approaches an asymptotic limit.

Dispersion has been extensively studied for decades but there are still theoretical and conceptual challenges (Sternberg *et al.*, 1996; Berkowitz and Scher, 1995; Kitanidis, 1992). Taylor (1922, 1953) for the first time suggested a Fickian representation for dispersion (constant dispersivity in the convection-dispersion equation). This model is widely used in solute transport in porous media. Several studies have shown that this assumption is not valid in porous media (Smith and

Schwartz, 1980; Domenico and Robbins, 1984; Sternberg *et al.*, 1996). Numerous other studies suggest that dispersivity depends on the mean travel distance and/or the scale of the observations (Peaudecerf and Sauty, 1978; Sudicky and Cherry, 1979; Pickens and Grisak, 1981a). These results imply that a unique dispersivity for the entire medium is not adequate to describe solute dispersion in porous media. This is because dispersivity depends on the observation scale (Schwartz, 1977; Wheatcraft and Scott 1988; Sternberg and Greenkorn 1994). Several studies have derived mathematical dispersivity models that account for scale dependency of dispersivities that vary with time and distance traveled. Examples include continuous time random walk models (Berkowitz and Scher, 1995; Bijeljic and Blunt, 2006; Rhodes *et al.*, 2007), non-local dispersion (Koch and Brady, 1987; Sternberg *et al.*, 1996), fractional derivative models, and time and scale dependent model (Benson *et al.*, 2000; Berkowitz *et al.*, 2002; Cortis *et al.*, 2004; Dentz *et al.*, 2004; Su *et al.* 2005). The lack of clear physical meaning of the parameters used to describe these models is the main drawback.

Heterogeneity in general is the primary cause of spreading and dissipation in field scale miscible displacement. The magnitude of dispersivity in heterogeneous media depends on the correlation structure of the conductivity, heterogeneity (Schwartz, 1977), and aspect ratio for field scale dispersion (Arya *et al.* 1988).

Pickens and Grisak (1981a,b) showed that dispersivity is scale dependent and increases with distance traveled. They summarized their results from numerical modeling, field and laboratory scale tracer tests. Gelhar *et al.* (1992) provided an extensive review of dispersivity observations for the longitudinal, horizontal transverse and vertical transverse dispersion. Their longitudinal dispersivities are in the range of 10^{-2} to 10^{4} m for length scales from 10^{-1} to 10^{5} m. Their data indicates that vertical transverse dispersivities are smaller than horizontal transverse dispersivities by an order of magnitude.

Coats *et al.* (2009) recently suggested to use a value on the order of 0.01 ft at the slim-tube scale, but also stated that dispersivity is not scale dependent. They suggested using this same value of 0.01 ft at the field scale. Mahadevan *et al.* (2003), however, showed that dispersivities from single-well tracer tests, which minimize convective spreading by reversing flow, are nearly two to three magnitudes greater (1.0 to 10.0 ft) than those values. Although reported otherwise by Coats *et al.*, Mahadevan *et al.* (2003) used the third-order total variation diminishing (TVD) method in UTCHEM so that numerical dispersion is a negligible part of their estimated dispersivities.

John *et al.* (2008) recently used particle tracking simulations to show that dispersivity is scale dependent. They demonstrated that velocity variations coupled with molecular diffusion cause local dispersivities on the order of those estimated by Mahadevan *et al.* (2003). A small value for dispersivity of 0.01 ft could only be used if reservoir heterogeneities are accurately known and simulated at that very small scale, something that is currently not possible at the pattern scale.

1.3 SPREADING VERSUS MIXING

It is difficult to distinguish between convective spreading and mixing based on the averaged breakthrough curves. Field and laboratory data presented in Figure 1.3 are not reliable in the sense that they are obtained by matching the effluent concentration to the solution of the convection-dispersion equation, whereas effluent concentration includes both convective spreading and dispersive mixing.

One way to distinguish between convective spreading and dispersive mixing is by flow reversal. Convective spreading is reversible; however, dispersive mixing is irreversible. Hulin and Plona (1989) performed laboratory experiments to investigate the reversibility of tracer dispersion in porous media and observed that in homogeneous media echo dispersion is the same as transmission dispersion and dispersion is fully irreversible. However, in heterogeneous media, dispersion is partially reversible and echo dispersion is less than transmission dispersion. Rigord *et al.* (1990) observed that for large penetration length, dispersion has become fully irreversible (same as transmission values), and at very small penetration distances echo dispersion is largely reversible and its value is 20 or 80 times less than its asymptotic limit. Leroy *et al.* (1992) showed that large fluid transports in the transverse direction can homogenizes concentrations across the sample, so that echo and transmission dispersivities become equal. Berentsen *et al.* (2005, 2007) extended Taylor dispersion for flow in stratified porous media to account for the partial reversibility of the spreading that occurs in flow reversal.

Another method is for distinguishing between convective spreading and mixing is to use local measurements of dispersion to distinguish between convective spreading and dispersive mixing. Kitanidis (1994) defined the concept of dilution index to recognize spreading from mixing. The rate of increase of mixing depends on the small-scale dispersion coefficient and also depends on the degree of irregularity in the shape of the plume. Cirpka and Kitanidis (2000) and Jose *et al.* (2004) used the breakthrough curve of a point within a domain to get information about convective spreading and mixing. Jha *et al.* (2006) showed by experiment that there is a local mixing occurring in porous media. Fiori (2001) showed that interplay between local-scale dispersion and large-scale advective displacement owing to long range correlated permeability is the cause of anomalous transport in porous media. Dentz and Carrera (2007) used the information of local scale mixing to estimate the effective solute mixing using an analytical model and random walk simulations. They used the local spatial moment with a Green function formulation to quantify enhanced solute mixing in a spatially non-homogeneous flow field.

1.4 IMPACT OF DISPERSION ON MISCIBLE DISPLACEMENT

Oil recovery from miscible gas floods is highly dependent on the magnitude of mixing at the field or pattern scale. Mixing of reservoir and injected fluids can decrease the strength of the injected fluid, and can cause early breakthrough. All multicontact (MCM) floods develop two-phase flow because mixing drives the composition route deeper into the two-phase region (Fig. 1.4), potentially reducing the local displacement efficiency significantly (Baker 1977; Walsh, and Orr, 1990; Fayers and Lee, 1994; Johns *et al.*, 1994, 2002; Stalkup, 1990, 1998; Barker and Fayers 1995; Solano *et al.*, 2001; Jessen *et al.* 2002).

Figure 1.5 presents ultimate oil recovery versus level of reservoir mixing in a 1-D model of MCM displacement after 2.0 HCPVI gas flood. Reservoir dimensions of this model are 200x1x1 of 1 ft grid-block sizes. Oil and gas compositions are given in Table 1.1. The level of reservoir mixing is increased by adding input physical dispersivity. Immiscible floods are least affected by dispersion because fluid compositions are relatively constant with negligible mass transfer between phases and shocks tend to be more self-sharpening. Mixing becomes more important as displacements become MCM and then first contact miscible (see Fig. 1.6).

If reservoir mixing is large, good recovery efficiency may require operating at pressures well above the minimum miscibility pressure (MMP) or even beyond the minimum enrichment for miscibility (MME) (Johns *et al.*, 2002; Solano *et al.*, 2001; Stalkup, 1998; Haajizadeh *et al.* 1999, 2000; Jerauld, 1998). This is because reservoir mixing can cause a multicontact miscible flood (MCM) to develop some two-phase flow; however, richer gases that mix closer to the critical locus in the two-phase zone, produce smaller and slower lean gas banks (Pande and Orr, 1989; Lake, 1989; Chang *et al.*, 1993).

1.5 DESCRIPTION OF THE PROBLEM

Dispersivity, which has units of length, measures mixing in a porous media. Numerous studies have observed that dispersivity grows with distance traveled (Pickens and Grisak, 1981a; Gelhar and Axness, 1983; Arya *et al.*, 1988; Berentsen *et al.* 2005; John *et al.* 2008). Conversely a few research studies stated that dispersion is solely the mixing that occurs at pore-scale; the large observed mixing at the field scale is only a result of heterogeneity, flow drifts and crossflow (Coats *et al.*, 2009).

Dispersivities estimated from field observations are often much larger than those measured in the laboratory for the same type of porous material. Dispersivities are small near the source and increase an order of magnitude with increasing travel distance from the source. The apparent large dispersivities observed at field-scale are a consequence of reservoir heterogeneity, lamination, flow pattern and crossflow. A key problem to be solved in this research is to identify the parameters that significantly affect dispersivity values from micro-scale to field-scale.

Mixing in a miscible displacement can significantly decrease oil recovery (Haajizadeh and Fayers, 2000; Johns *et al.* 2002; Stalkup, 1998; Jessen *et al.* 2002). Unfortunately the level of dispersion at which to evaluate mixing in a reservoir by numerical simulation is not well known. The total or "apparent" dispersivity modeled in numerical simulation of miscible displacements is the sum of physical (input) dispersivity, numerical dispersivity associated with grid-block sizes, and dispersivity owing to heterogeneities. The apparent dispersivity should be equal to field-scale dispersivity in all directions to accurately model a field-scale miscible displacement. This research determines appropriate grid-block sizes to be used to model field-scale and pattern-scale miscible displacements.

Numerous studies have been performed to understand scale-dependent dispersivity and to determine dispersivity at field and laboratory-scale (Sternberg and Greenkorn, 1994; Gelhar and Axness, 1983; Arya *et al.* 1988). Gelhar and Axness (1983) presented dispersivity as a function of stochastic reservoir heterogeneity at field-scale. Although the predicted dispersivity from the stochastic theory is consistent with field experiments, it cannot predict local mixing and echo dispersivities. The effective strength of the injected gas is only affected by dispersive mixing not convective spreading of velocity variation in transmission dispersion. Sternberg and Greenkorn (1994) determined dispersivity as a function of advective velocity, permeability, viscosity, length traveled and layering; however, the statistical correlation failed to model dispersion in heterogeneous porous media. Therefore, an appropriate dispersivity model that determines reservoir mixing as a function of stochastic reservoir heterogeneity and reservoir properties is needed to estimate the physical level of reservoir mixing occurring in a permeable medium.

1.6 OBJECTIVES

Based on an extensive literature review, problem description and the gap between the understanding of dispersion and its impact on miscible displacement, the objectives of this study are to:

1. Understand the origin of scale dependent dispersivity from micro-scale to macro-scale and finally at the field-scale.
2. Determine dispersivity (reservoir mixing) as a function of reservoir parameters and stochastic heterogeneity of the reservoir.
3. Determine appropriate grid-block sizes that should be used in compositional simulations to accurately predict oil recovery from miscible displacements.

1.7 ORGANIZATION OF THE DISSERTATION

Chapter 2 demonstrates an understanding of the origin of scale dependent dispersivity in porous media. It presents pore-scale simulations of dispersion in porous media for various configurations and heterogeneities. In chapter 2 we also study transverse dispersion and discuss the ratio of transverse to longitudinal dispersivity at pore-scale porous medium. The dispersion-dependence on the pore-Peclet number is shown in this chapter.

In chapter 3, we undertake a comprehensive inspection of the key scaling groups and how they impact reservoir mixing. Inspectional analysis shows that reservoir mixing depends on the aspect ratio, the mobility ratio, the dispersion number, the Peclet number, and heterogeneity parameters; such as the horizontal and vertical correlation lengths and the variation of the medium's permeability in the bulk-flow direction. This research examines only effective local mixing, not apparent mixing caused by variations in streamline path lengths (convective spreading). Dispersivity is estimated from the response function based on well spacing and other major reservoir parameters.

In Chapter 4, we introduce a method to upscale flow and transport in porous media. This chapter deals with numerical dispersion and equivalent grid-block size. We show through simulations of both first-contact miscible (FCM) and multi-contact miscible (MCM) floods that grid-block size can be significantly increased if reservoir mixing is large. To properly upscale miscible floods, the sum of numerical dispersion and dispersion associated with reservoir heterogeneities must be equal at both fine and large-scales. We develop a novel method to identify the maximum grid-block size that can be used to accurately predict ultimate oil recovery.

Chapter 5 summarizes the contribution of this research on upscaling miscible floods in heterogeneous reservoirs considering reservoir mixing. It contains an overview of this research, results, conclusions and recommendations.

Component	Reservoir Oil	Lean Gas	Solvent	MI 65%
CO_2	0.015	0.0815	0.2120	0.1663
C_1	0.5069	0.8305	0.2770	0.4707
C_2	0.0587	0.062	0.2050	0.1550
C_3	0.0358	0.0225	0.2560	0.1743
C_4	0.0192	0.0035	0.0500	0.0337
C_5	0.0161			
C_6-C_7	0.0379			
C_8-C_{10}	0.0725			
C_{11}-C_{14}	0.0639			
C_{15}-C_{19}	0.0614			
C_{20}-C_{29}	0.0639			
C_{30+}	0.0487			

Table 1.1: Oil and gas compositions used in the MCM displacement model.

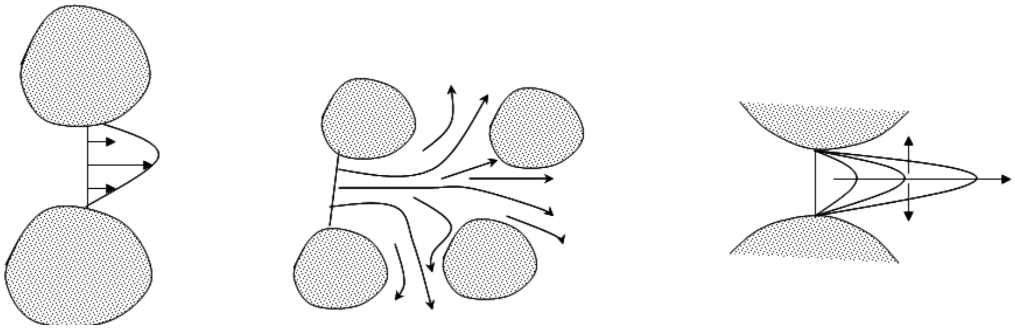

Parabolic distribution of velocity

Variation in flow respect to bulk flow

Molecular diffusion effect

Figure 1.1: Hydrodynamic dispersion owing to mechanical spreading and molecular diffusion (Bear and Bachmat, 1990).

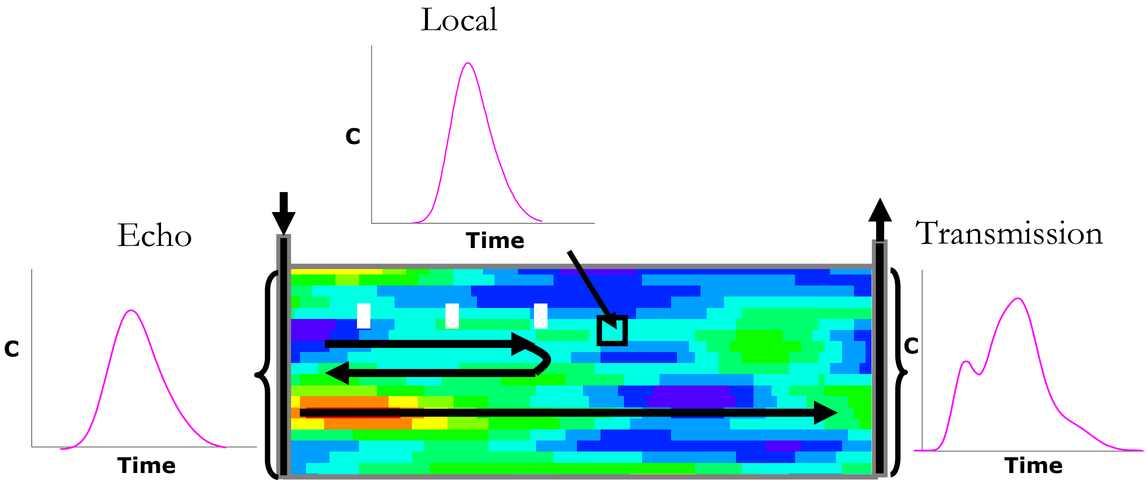

Figure 1.2: Echo, transmission and local dispersion in a 2-D cross section.

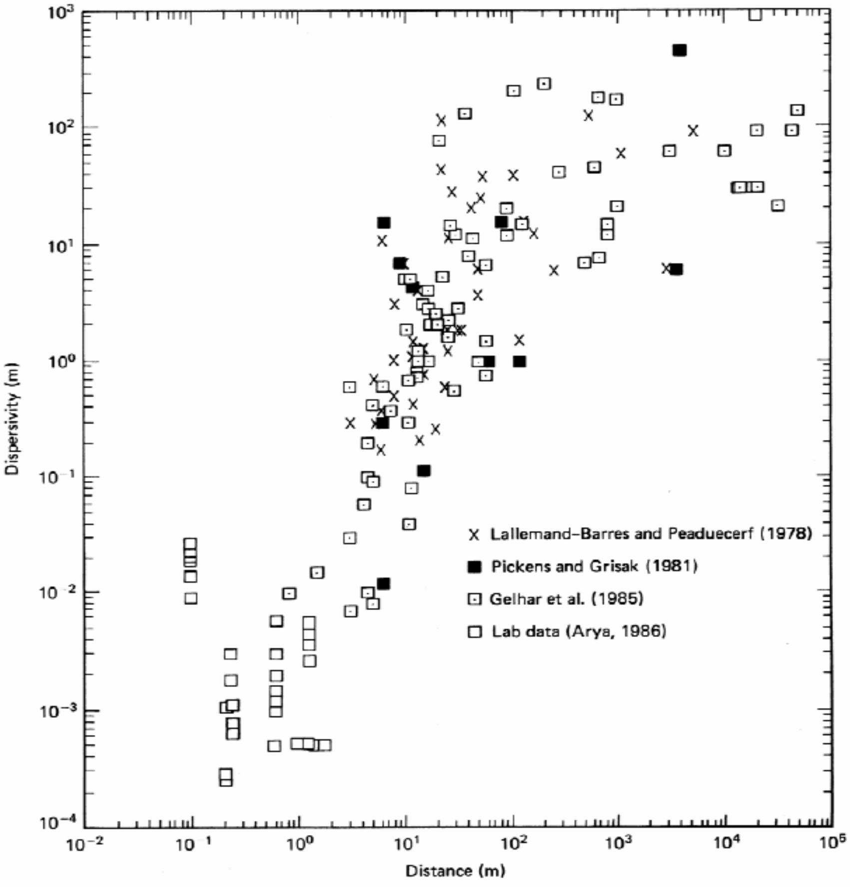

Figure 1.3: Field and laboratory measured dispersivities (from Lake, 1989, Arya *et al.*, 1988)

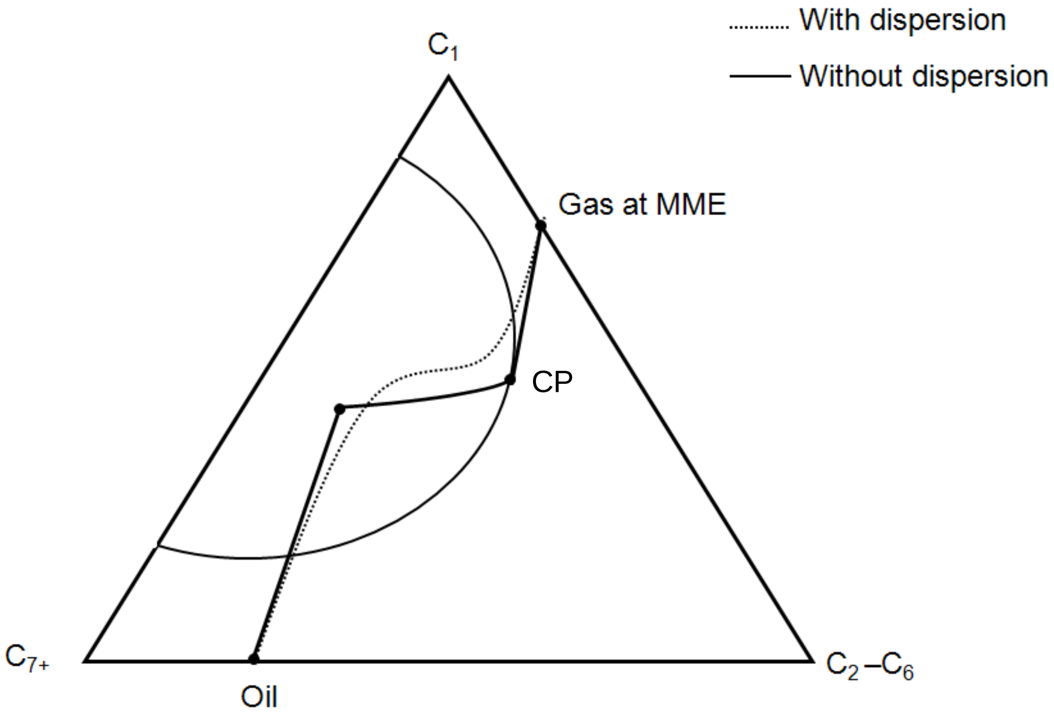

Figure 1.4: Schematic representation of the impact of dispersion on the composition route of a MCM displacement ternary diagram (Solano, 2000).

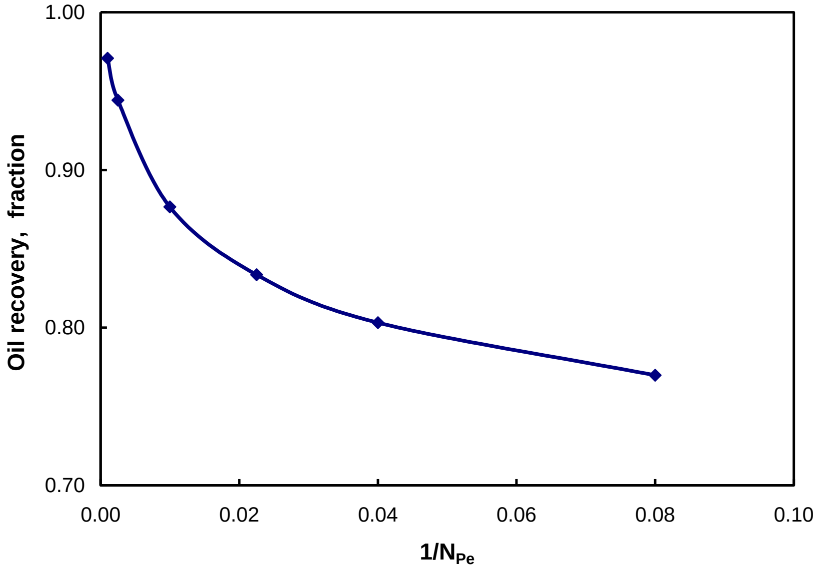

Figure 1.5: Impact of reservoir mixing on ultimate oil recovery from a 1-D MCM displacement after 2.0 HCPVI gas flood.

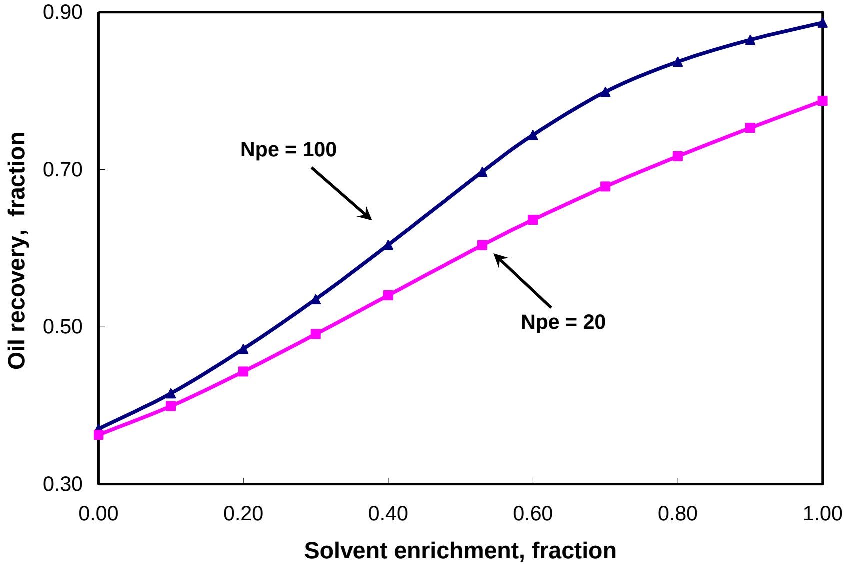

Figure 1.6: Impact of gas enrichment and dispersion (mixing) on ultimate oil recovery from a 1-D MCM displacement after 2.0 HCPVI gas flood. The influence of reservoir mixing on ultimate oil recovery is increased as gas is enriched.

Chapter 2: Pore-Scale Simulation of Dispersion in Porous Media

This chapter examines the mixing that occurs in porous media by solving for single-phase flow in a connected network of pores. This work differs from network models in that we directly solve the Navier-Stokes equation and the convection-diffusion equation to determine the velocities and concentrations at any location within the pores. Flow in series and layered heterogeneous porous media are modeled by using many grains in different arrangements. We consider slug and continuous injection as well as echo tests (single-well tracer tests) and transmission tests (interwell tracer tests). We match the concentrations from the pore-scale simulations to the analytical convection dispersion solution that includes both transverse and longitudinal dispersion coefficients.

The results show that for flow in series and in layers, echo and transmission longitudinal dispersivities become equal and reach an asymptotic value if complete mixing over a cross section perpendicular to flow has occurred. In practice, the asymptotic value of dispersivity may never be reached depending on pattern-scale heterogeneity and well spacing. Transverse dispersion coefficients also are scale dependent, but they decrease with traveled distance. We further demonstrate that the classical Perkins-Johnston relationship between longitudinal dispersion coefficient and fluid velocity is obtained.

2.1 OVERVIEW

Mixing in a reservoir is primarily caused by molecular diffusion of solute (or gas) from one streamline to the next within the pores. Mixing causes dilution of the gas, which can decrease oil recovery in a miscible flood. Reservoir mixing is enhanced by any mechanism that increases the area of contact between the gas and the oil, thereby allowing the effects of diffusion to be magnified. This is in essence the cause of scale-dependent dispersion. The longer the distance traveled of a solute the greater the area exposed to diffusion and the longer time diffusion has to work. The contact area grows primarily because of variations in streamlines and their velocities around grains and through layers of various permeabilities (heterogeneity). Crossflow, such as that caused by gravity, can also allow for greater mixing when a fluid of different density than the reservoir oil is injected. Mixing can also be enhanced by the effects of other neighboring wells (fluid drift), and by differences in chemical potentials between components in different phases, that is, by phase mass transfer.

The level of mixing in a reservoir is generally quantified by measuring the dispersion coefficient and its associated dispersivity. Transmission dispersivities include both actual dilution (mixing) and convective spreading. Convective spreading at the pore scale occurs solely because of solute taking different streamlines with varying velocities and arriving at different times to a fixed location. Convective spreading in continuum porous media is caused by flow through layers of differing permeability. Lake and Hirasaki (1981) considered this case and showed that complete mixing across layers occurs when the transverse dispersion number is greater than five. For layered flow with transverse dispersion numbers less than 0.2, transmission dispersion coefficients will never approach an asymptotic limit no matter the distanced traveled. The transverse dispersion number is the ratio of the time required for solute to cross the medium longitudinally owing to convection to the time required for solute to cross the transverse direction owing to dispersion.

Measured concentrations are typically made in well-mixed boreholes where differentiation between convection spreading and actual mixing is not possible. Differentiation is only possible when local measurements of dispersion in the reservoir can be made (Kitanidis, 1994; Cirpka and Kitanidis, 2000; Jose *et al.,* 2004; Dentz and Carrera, 2007).

Figure 2.1 illustrates the differences between convective spreading and actual mixing for two levels of diffusion in a reservoir that contains four layers of varying permeability, and hence fluid velocity. The injection well (at the left of Fig. 2.1) introduces a concentration pulse that travels through the formation according to the velocity in each layer. For zero diffusion (Fig. 2.1a), there is no actual mixing of injected fluids with reservoir fluids, and the concentration pulse travels through each layer without losing its peak strength. Local measurements of mixing (in a given layer) or that measured by an echo test would show one concentration pulse as is illustrated in the concentration profile of Figure 2.1a. The concentration profile at the production well (outlet as measured during a transmission test), however, indicates that mixing occurred in the reservoir. This apparent mixing is what we term convective spreading. When diffusion is present, as it always is, mixing occurs between layers and at fronts (see Fig. 2.1b). Mixing is enhanced in this case by the increased area of contact between layers. True mixing is not reversible by an echo test, as is shown in the concentration profile of Figure 2.1b. True mixing can only be differentiated from apparent mixing by comparing the overall composition profile (from a transmission test) to local measurements made by an echo test.

When mixing is complete in the transverse direction, mixing-zone growth scales with the square root of time. This type of dispersion is Fickian, as opposed to nonFickian. NonFickian dispersion is caused by the presence of convective spreading, and therefore does not scale with the square root of time. Purely convective spreading, such as that indicated in Figure 2.1a, gives mixing-zone growth for layered flow that scales linearly with time. The goal of reservoir engineers should be to understand how much mixing is occurring at the field scale compared to convective spreading because of their different impact on miscible gas and chemical-enhanced oil recovery. Only true mixing causes the effective strength of a mixing gas to be decreased or surfactant concentrations to be reduced.

Mixing is an irreversible phenomenon (Hulin and Plona, 1989; Rigord *et al.* 1990; Leroy *et al.* 1992; Jha *et al.* 2006a); in that flow reversal will not cause the fronts to move back together at the injection well. Thus, echo tests (single-well tracer tests), which reverse flow, measure a level of mixing that is equal to or less than that obtained from transmission tests. This is because echo tests eliminate convective spreading that occurs in a porous media.

Mahadeven *et al.* (2003) examined single-well tracer tests (echo tests) that were specifically selected because of their small fluid drifts. Dispersivities estimated from those tests were on the order of 2.0 to 3.0 ft substantially greater than laboratory dispersivities of approximately 0.01 to 0.03 ft. Thus, those field tests are a direct proof of the scale dependency of dispersion.

There are hundreds of papers that examine the scale dependence of dispersion for solute transport in homogeneous and heterogeneous aquifers (Picken and Grisak, 1981 a,b; Gelhar *et al.*, 1992; Sternberg *et al.* 1996; Sternberg 2004). A variety of complex-dispersivity models and methods have been generated that exhibit scale-dependent dispersion in heterogeneous aquifers. Examples include random-walk models, fractional derivative models, time-dependent dispersivities, and nonlocal dispersivity models (Sternberg 2004; Sternberg *et al.* 1996; Berkowitz and Scher 1995; Berkowitz *et al.* 2002; Cortis *et al.* 2004, Dentz *et al.* 2004). Transmission dispersion in heterogeneous-porous media has been well documented to depend on the permeability heterogeneity (correlation length and standard deviation), aquifer aspect ratio, and diffusion level (solute diffusion in gas vs. water) (Arya *et al.* 1988). Asymptotic values of dispersivity (Fickian dispersion) have been observed with continuum porous media simulations, and predicted by stochastic modeling studies (Gelhar and Axness 1983). Very few papers have discussed measurement of transverse dispersion, but transverse dispersivity is also likely dependent on the pore structure, grain size, and heterogeneity (Grane and Gardner 1961; Van Gulijk, 1998; Theodoropoulou *et al.* 2003; Gaganisa *et al.* 2005; Bijeljic and Blunt 2007).

In this chapter, we examine both transmission and echo dispersion at the pore scale to illustrate scale dependency of dispersion for a variety of boundary conditions and heterogeneities. We first present the simulation model and the equations that are used to solve for velocities and concentrations within the pores. Next, continuum simulations are performed to examine further the differences between convective spreading and mixing, and to better explain echo and transmission results. We then demonstrate for pore-scale models that the classical Perkins and Johnston dispersion curves are obtained as a function of the pore Peclet number. Results for more realistic non-uniform, series, and layered pore-scale models are also given. Both two-dimensional and three-dimensional pore morphologies are considered as well as transverse and longitudinal dispersion coefficients (D_L and D_T). Last, conclusions are presented.

2.2 MATHEMATICAL MODEL

We model solute transport for both continuum porous media and pore-scale models using the commercially available code COMSOL. When the continuum option is used, velocities and longitudinal/transverse dispersivities for each layer are specified and COMSOL only solves the convection-dispersion equation. Continuum simulations are not the focus of this chapter, but are used to illustrate spreading and mixing in layered media, as well as to explain the differences between echo and transmission tests.

For pore-scale simulations, COMSOL uses finite-element methods to solve first for the steady-state single-phase velocities in each pore using the Navier-Stokes and continuity equations. After velocities are calculated, solute concentrations are determined by solving the convection-diffusion equation in two or three-dimensions.

Fluid mass balance is described using the continuity equation for steady-state incompressible flow:

$$\nabla \cdot \mathbf{v} = 0 \tag{2.1}$$

where **v** is the pore velocity vector. Simulations are at the pore-scale in that grain boundaries are explicitly modeled as no-slip boundaries. No-slip boundaries give zero velocity both normal and tangential to the grain surface. For most simulations, we continuously injected solute at a constant velocity v_{inj}. At the injection boundary there are no grains so that the mean pore velocity must increase within the pores as grains are encountered. Pore velocities can vary significantly over small distances depending on the size of the grains and pores. The pressure at the outlet is constant at atmospheric pressure.

A momentum balance of the fluid is modeled using the incompressible Navier-Stokes equation:

$$\rho \frac{\partial \mathbf{v}}{\partial t} - \mu \nabla^2 \mathbf{v} + \rho(\mathbf{v} \cdot \nabla)\mathbf{v} + \nabla P - \rho \mathbf{g} = 0 . \tag{2.2}$$

where ρ is fluid density, μ is fluid viscosity, P is the medium pressure and g is the gravity constant. For steady state flow where gravity is also negligible, the Navier-Stokes equation further reduces to

$$\mu \nabla^2 \mathbf{v} = \rho(\mathbf{v} \cdot \nabla \mathbf{v}) + \nabla P \ . \tag{2.3}$$

Equation (2.3) is used in this research where the fluid density and viscosity are taken to be constant, and therefore independent of concentration.

The solution of Equations (2.1) and (2.3) give the pore velocities at each node of the finite element model. Typically, we used 20,000 to 100,000 elements to reduce discretization errors to negligible levels. Once pore velocities are determined, the solute concentrations are found by solving the time-dependent convection-diffusion equation:

$$\frac{\partial C}{\partial t} + \nabla \cdot (-D_0 \nabla C + C\mathbf{v}) = 0 , \tag{2.4}$$

where D_o is the diffusion coefficient of solute in the single-phase fluid and is generally taken to be $10^{-9}\, m^2/s$. We typically injected solute over the entire length of the pore-scale model, except as noted in the text. The strength of the solute is set to C_O at the injection boundary, while the initial solute concentration is zero within the pore-scale model. Solute flow owing to both convection and diffusion is zero at the top and bottom of the model, as well as at all grain boundaries. Zero diffusive flux is assumed at the outlet.

From Equations (2.1) through (2.4) and the specified boundary conditions, the solution concentrations for two-dimensional pore-scale simulations are functions of six dependent variables, and six parameters. That is,

$$C = f(x, y, t, v_x, v_y, P; v_{inj}, \mu, \rho, D_P, D_O, C_O) \ . \tag{2.5}$$

where v_x and v_y are velocity components in x- and y-directions, D_P is the grain diameter. We can combine the parameters to form dimensionless groups. For example, the dimensionless concentration is a function of six dimensionless variables and two dimensionless groups:

$$C_D = f(x_D, y_D, t_D, v_{Dx}, v_{Dy}, P_D; \mathrm{Re}, N_{Pe}), \tag{2.6}$$

where the dimensionless variables and parameter groups are defined as,

$$C_D = \frac{C}{C_O} \tag{2.7-a}$$

$$x_D = \frac{x}{D_P} \tag{2.7-b}$$

$$y_D = \frac{y}{D_P} \tag{2.7-c}$$

$$t_D = \frac{v_{inj} t}{D_P} \tag{2.7-d}$$

$$v_{Dx} = \frac{v_x}{v_{inj}}, \tag{2.7-e}$$

$$v_{Dy} = \frac{v_y}{v_{inj}}, \tag{2.7-f}$$

$$\mathrm{Re} = \frac{\rho v_{inj} D_P}{\mu}, \tag{2.7-g}$$

$$N_{Pe} = \frac{v_{inj} D_P}{D_o} \quad . \tag{2.7-h}$$

The pore Peclet number (N_{Pe}) is the ratio of the time for diffusion to cross a distance of one grain diameter to the time for convection to travel the same distance. Thus, large Peclet numbers imply a convection-dominated process.

The Reynolds number (*Re*) relates inertial forces to viscous forces. Small Reynolds numbers occur in laminar flow, while turbulent flow occurs at relatively large values. In general, Reynolds numbers are small in porous media and flow is laminar. Figure 2.2, for example, shows flow around one circular grain for large and small Reynolds numbers. The results show that all streamlines are reversible for small Reynolds number, but are irreversible for large Reynolds numbers in which inertial effects are more important (see Fig. 2.3). In this research, we only consider laminar flow so that streamlines are always reversible, regardless of the number of grains and their configuration. Thus, for uniform packing of grains the dimensionless concentrations are only functions of one parameter group, the pore-Peclet number. We can still have irreversible dispersion even though streamlines are reversible.

2.3 CONVECTIVE SPREADING AND MIXING

In this section, we further illustrate the difference between convective spreading and mixing by use of continuum porous media simulations. We consider a ten-layer porous media in which the velocities in each layer are constant temporally but vary in each layer. The velocities vary by a factor of 2.0, in which the smallest velocities represent layers with lower permeabilities. Table 2.1 gives the velocities for each layer in which the first layer corresponds to the bottom layer. Dispersion coefficients are calculated by use of $D_L = \alpha_L v$. For each layer, the transverse and longitudinal dispersivities are equal and constant at 1.0E–4 m; thus, the dispersion coefficients in each layer vary by only a factor of 2.0. The dimensions of the 2-D model are 1.0 m x 0.25 m. We used 20,000 finite elements to reduce numerical dispersion to negligible levels.

Figure 2.4a shows the concentration profile at 0.3 pore volumes injected (PVI) for injection of a solvent slug of size 0.025 PVI. The injection well is at the left of the model, and the production well to the right. Figure 2.4b gives the transmission concentration histories for the local concentrations in layer 6 and the overall concentrations averaged over the cross section at x = 0.3 m. As shown, the local response is less mixed than the overall concentrations, which is similar to the illustration in Figure 2.1 for transmission tests. The overall concentrations appear to be well mixed, although in this case there is very little mixing, as is evident from the concentration profile (see Fig. 2.4a). The overall concentration curves for Figure 2.4b are clearly non-Fickian.

Figure 2.5a illustrates the same displacement except where the input physical dispersivities are larger by a factor of 100. In this case, the local and overall concentration histories are nearly equal, indicating that mixing is nearly complete over the transverse direction to flow. This is clearly evident in the concentration profile of Figure 2.5a. Thus, dispersion for this case is Fickian and the level of dispersion (mixing) has reached its asymptotic limit. Once the asymptotic values are reached, dispersivities no longer increase with distance traveled.

Concentration histories from echo tests performed by reversing the flow at 0.3 PVI for the same ten-layer model of Figure 2.4 is illustrated in Figure 2.6. As shown, the non-Fickian features of the layered model in Figure 2.4 are no longer present in the echo concentrations because flow reversal compensates for convective spreading in each layer. Mixing from the overall concentration history, however, is greater than mixing for the local concentrations (taken at the inlet in layer 6). The greater level of mixing for the overall concentrations is the result of additional mixing made possible by diffusive crossflow between the layers. For both displacements in Figures 2.4 and 2.5, whether large or small mixing, echo tests give estimates of true mixing for the overall ten-layer model. That is, no differentiation between convective spreading and true mixing is necessary with echo tests for these cases.

Echo tests for a greater travel distance (larger PVI at reversal) than in Figure 2.6 show even more mixing from the overall concentration history compared to the local concentration history. This scale dependency results from more time and contact area available for crossflow between the layers when flow is reversed at 0.5 PVI instead of 0.3 PVI. We will show this same scale dependency through use of pore-scale simulations.

2.4 PORE-SCALE SIMULATION IN HOMOGENEOUS POROUS MEDIA

Pore-scale porous media was modeled by solving for single-phase flow in a connected network of pores and grains (Fig. 2.7). The medium consists of a rectangular plate and circular holes, which represent grains. Fluids can flow through the pore space between grains. The Navier-Stokes equation is solved to obtain the steady-state velocity field inside the pore-scale porous medium.

2.4.1 Two Dimensional Model

Figure 2.7 shows the steady-state velocity field in a 2-D homogeneous packing of spherical grains of size 0.02 mm. Fluid is injected at a constant velocity of 10^{-5} m/s at the inlet face, and the outlet face is maintained at the atmospheric pressure. Bottom and top boundaries are at no-flow condition and grain boundaries are no-slip. Figure 2.8a shows the concentration profile in the pore space for continuous injection at about 0.4 PVI. As shown, the level of mixing in this example is small, corresponding to a pore Peclet number of $N_{Pe} = 3$.

The longitudinal dispersion coefficient for the displacement in Figure 2.8a is calculated by matching the analytical convection-dispersion equation to the transmission concentrations at the production well ($x_D = 1$). That value along with those calculated using various levels of mixing are plotted in Figure 2.8b normalized by the diffusion coefficient. As shown, the dispersion coefficient increases with the pore Peclet number. The ratio of D_L/D_O approaches the tortuosity coefficient for the pore-scale model at small values of the Peclet number, where diffusion dominates. At large values of the Peclet number, convection dominates and the increase in D_L/D_O with the Peclet number shows the conventional Perkins and Johnston (1963) response. The slope, however, for this case is 1.89 instead of the classical 1.1 – 1.3 value for well-packed porous media (Bijeljic *et al.* 2004; Sahimi *et al.* 1982; Sorbie and Clifford 1991).

The difference in slope is likely the result of uniform grain distribution (Plumb and Whitaker, 1988; Whitaker, 1999) and the large porosity of 61% in our pore-scale model, as well as that flow is 2-D here. Jha (2008) showed that use of an irregular grain distribution reduces the slope to approximately 1.2. The slope also decreases towards the classical range as the porosity is reduced by filling in the pore space of Figure 2.8a by adding grains of smaller size (see Figs. 2.9 and 2.10). The Peclet number ranges from 0 to 500 for these values. Figure 2.11 shows that the slopes decrease further for larger Peclet numbers, as was also observed by Bijeljic and Blunt (2006).

The echo longitudinal dispersion for displacement of Figure 2.8 was calculated by matching the reversed flow and concentration at $x_D = 0$. The calculated values using various levels of mixing are compared with transmission dispersion and plotted in Figure 2.12. As shown, the echo dispersion has the same behavior as transmission dispersion in homogeneous uniform grain pack.

Figure 2.13 shows that the ratio of D_L/D_O decreases linearly with increasing porosity. This is the result of greater mixing in the pores owing to larger velocity fluctuations within the pore-scale model as porosity is reduced. Mixing is also greater when the mean pore velocity is increased owing to greater variations in velocity within the pores as well. When the mean pore velocity v is small, velocity variations within the pores are small, and mixing is primarily the result of diffusion.

Next, we performed transmission tests by continuous injection of solute into the homogeneous and uniform pore-scale model shown in Figure 2.14a. The pore Peclet number for this displacement is 20. We matched the longitudinal dispersivity from the transmission concentrations at various measured distances using the analytical CD solution (Lake 1989). As shown in Figure 2.14b, the calculated transmission dispersivity increases with mean distance traveled, but eventually approaches a constant value (asymptotic limit). Figure 2.14b also shows the longitudinal dispersivities estimated from the echo tests, where flow was reversed after some mean travel distance into the pore-scale model. Thus, for echo tests, the total travel distance out and back is plotted in Figure 2.14b. As shown, the echo dispersivities also show scale dependence, but are always equal or less than the transmission values. Echo dispersivities do eventually approach the transmission dispersivities at the asymptotic limit. The echo dispersivities are generally smaller than the transmission values because flow is reversed in echo tests, which eliminates convective spreading caused by variations in streamline paths. The behavior at the pore-scale is similar to what is observed for permeability variations (or streamline variations) at larger scales (Rigord *et al.*, 1990; Leroy *et al.*, 1992; Jha *et al.*, 2006; John, 2008).

2.4.2 Three Dimensional Model

Consider the homogeneous three-dimensional model given in Figures 2.15 and 2.16. Very few spherical grains are modeled because of the computational time required in the COMSOL simulations.

We calculated the longitudinal dispersivity for the three-dimensional model by averaging the concentrations over a cross-section. We compared those estimated dispersivities to the 2-D model shown in Figure 2.15b where the injection velocity was kept the same. The 2-D model corresponds to the horizontal cross section through the midpoint of the 3-D model. The transmission longitudinal dispersivities are somewhat greater in the 3-D model than in the 2-D model, likely the result of greater contact area between the solute and the uncontaminated fluid in 3-D. Furthermore, breakthrough of solute occurs earlier in the 2-D model owing to differences in porosity (75% in 3-D and 64% in 2-D). In general, we expect that mixing and dispersivities from 3-D flow should be greater than in 2-D (see Figs. 2.16, 2.17).

2.5 PORE-SCALE SIMULATION IN HETEROGENEOUS POROUS MEDIA

In this section we demonstrate the scale dependence of dispersion that results from series and parallel layers in the pore-scale simulations. Figure 2.18a shows a parallel model where two homogeneous and uniform grain packs of different sizes are placed on top of each other. The pore-scale model is therefore doubled in height from the previous models. The grain sizes differ by a factor of two in the parallel model, and in the series model.

The results show that there is a large region where crossflow and diffusive mixing takes place between the layers (see Fig. 2.18a). Figure 2.18b shows that the echo dispersivities with crossflow increase without bound. When the layers are separate (no crossflow), the echo dispersivities are constant with distance traveled. The echo dispersivities with crossflow do not reach an asymptotic limit in this case because the rate of increase in the length of the crossflow region with time is much faster than rate of diffusive transport of solute across the layers. If this trend in echo dispersivities were to continue indefinitely, the dispersivity would be about 0.01 ft for a 3-ft core. Although extending this trend forward is speculative, it does indicate that the levels of dispersivities calculated from the pore-scale simulations are consistent with those measured at the scale of laboratory cores. If one would continue the extrapolation even further, the trend predicts smaller value, but on the order of mixing estimated from single well tracer tests (Mahadevan *et al.* 2003). More heterogeneous pore models would likely give greater echo dispersivities.

This scale dependency results from more time and contact area available for crossflow between the layers as evident from Fig. 2.19. It can be observed that echo dispersivities are increased linearly with increased average surface contact area. This is because of enhanced impact of diffusion by traveled distance.

Figure 2.20 shows the concentration profiles for a pore-scale model with series layers or zones. Mixing in the first zone proceeds as if the model were homogeneous. That is, the transmission dispersivities quickly reach an asymptotic limit for this case at about 0.0105 mm (see Fig. 2.21). The pore velocities in that zone, however, increase prior to reaching the boundary of the next larger grain size zone. This occurs because there is a large pore space immediately in front of the first zone, and the velocities respond to that (i.e. there is no distinct boundary here). The transmission dispersivities, therefore, increase before reaching the second zone. A similar, but opposite effect occurs between the second and third zone. Once the solute is within the second zone, the transmission dispersivities increase to the larger asymptotic limit corresponding to the second layer (the second layer has a pore Peclet number twice as large as the first layer). The transmission dispersivities in the third zone, however, do not decrease rapidly to the asymptotic limit of the third zone, which is identical to the first zone. That is, the effects of the middle layer are retained for a significant distance into the third zone.

The echo dispersivities in the series model (Fig. 2.21) have similar trends as the transmission values, but they are sometimes greater than the transmission dispersivities. This is because the middle zone is traversed twice by the echo dispersivities when flow is reversed at mean distances greater than 12 mm. Both the transmission and echo dispersivities in these cases represent true mixing, but over the portions of the pore-scale model that were investigated.

2.6 TRANSVERSE DISPERSION

Consider next the continuous injection of solute, but only in the lower 1/10th of the injection well. The pore-scale model is still homogeneous with uniform grain size and packing as shown in Figure 2.22a. As shown, the concentrations first move horizontal, but then must move around a grain in a decidedly vertical track. This behavior continues as the solute moves into the pore-scale model.

The concentrations were matched to the 2-D analytical convection-dispersion solution (Cleary and Ungs 1978; Javandel *et al.* 1984) for a continuum porous medium to obtain the "best fit" longitudinal and transverse dispersion coefficients (see Appendix A). Figure 2.22b shows that the transverse dispersion coefficient D_T decreases with distance traveled owing to the significant initial vertical movement around grains, where as the longitudinal dispersion coefficient D_L increases somewhat to its transmission asymptotic limit.

The ratio of D_T/D_L is exactly equal to the ratio of the dispersivities (α_T / α_L) for the pore-scale model when diffusion is neglected. This result takes the pore-scale model as a continuum so that the mean pore velocity in the vertical direction is zero. In Figure 2.22b the ratio of α_T / α_L is between about 2.0 to 6.0 instead of the classical values between 0.01 and 0.5 for well packed porous media. The large dispersivity ratio is solely the result of large porosity, in this case around 61%. If the displacements are repeated for smaller porosity and non-uniform grain sizes, the transverse dispersion coefficient is less than the longitudinal value and the ratio is decreased by an order of magnitude to values between 0.1 and 0.5 (see Fig. 2.23). This is the result of the smaller grains, which are now in the centers of the previously large pores of Figure 2.22, blocking movement of the solute in the vertical direction.

2.7 CONCLUDING REMARKS

In this chapter, we examined a variety of pore-scale models to demonstrate that dispersivities (or dispersion) are scale dependent. We also defined and explained the differences between convective spreading and mixing. Our main conclusions are

- The pore-scale simulations produce similar features that are observed in experimental measurements of mixing. That is, the simulations demonstrate the classical Perkins-Johnston relationship between longitudinal dispersion and pore Peclet number.
- Single well tracer tests (echo tests) determine the true mixing in a reservoir. Interwell tracer tests (transmission tests) are not reliable indicators of mixing.

- Both echo and transmission dispersivities increase with distance traveled. They may or may not reach an asymptotic limit depending on the heterogeneities encountered. The scale dependence results from an increase in the contact area between solute (gas) and resident fluid (oil) as heterogeneities are encountered, either at the pore scale or at the pattern scale. Mixing is increased with increasing contact area because the effect of diffusion is enhanced. That is, dispersivity increases as increased scales of heterogeneity are encountered.
- Convective spreading is not mixing, but can cause mixing by diffusion to be enhanced.
- Transverse dispersivities are also scale dependent, but decrease with distance traveled. The ratio of the transverse dispersivity to the longitudinal dispersivity becomes small as porosities are reduced in pore-scale models.

Layer #	Velocity, 10^{-5} m/sec	Layer #	Velocity, 10^{-5} m/sec
1	2.0	6	1.6
2	1.1	7	1.3
3	1.2	8	1.4
4	1.5	9	1.3
5	2.1	10	1.6

Table 2.1: Continuum model velocities in each layer.

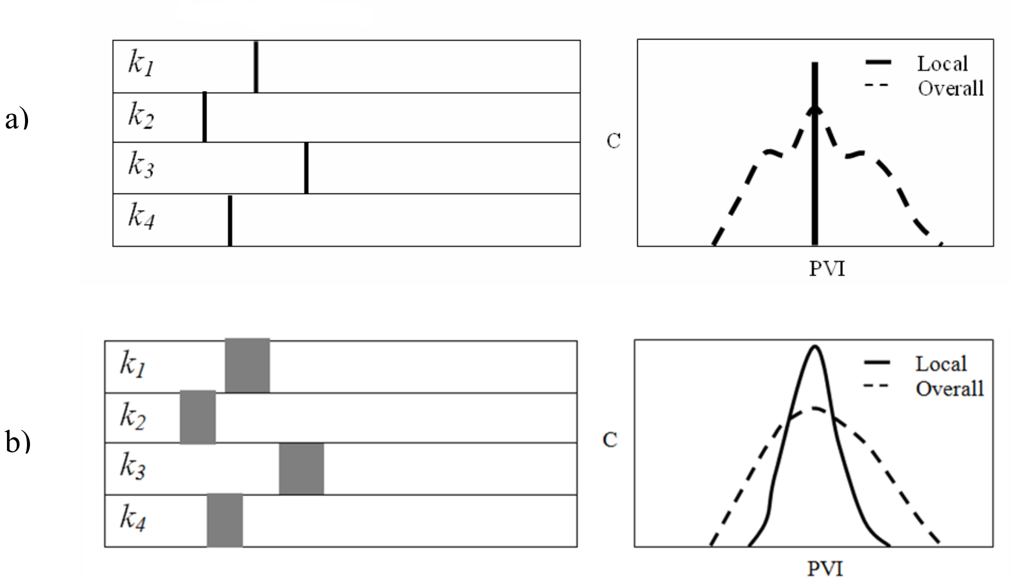

Figure 2.1: Illustration of the differences between convective spreading and mixing for a four-layered porous media with $k_3>k_1>k_4>k_2$. Convective spreading causes no actual mixing. a) No mixing, b) Some mixing.

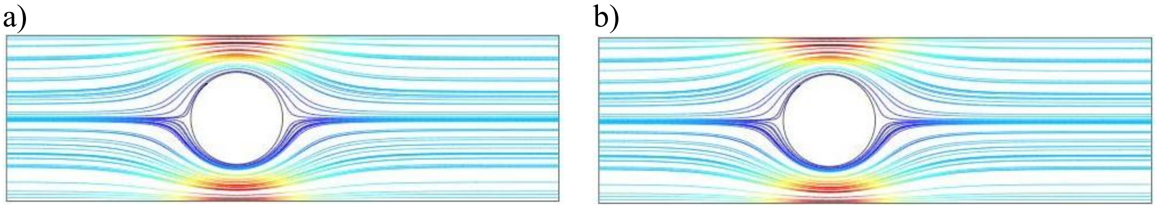

Figure 2.2: Streamlines for flow around one spherical grain with small Reynolds number, *Re*=*0.2*, (a) Direction of flow is to the right; (b) Direction of flow is to the left. The streamlines are reversible.

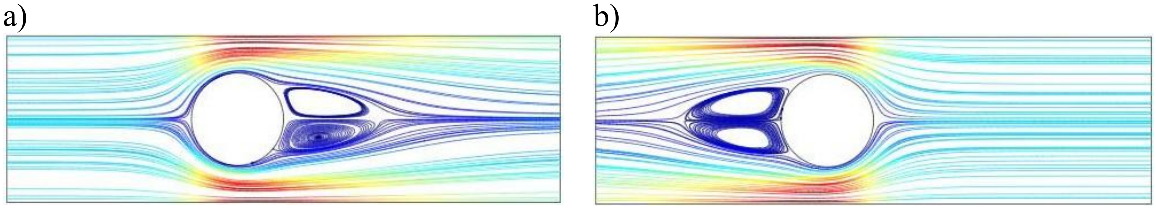

Figure 2.3: Streamlines for flow around one spherical grain for large Reynolds number, *Re*=*20*. (a) Direction of flow is to the right; (b) Direction of flow is to the left. Streamlines are irreversible in that flow eddies result owing to large inertial forces.

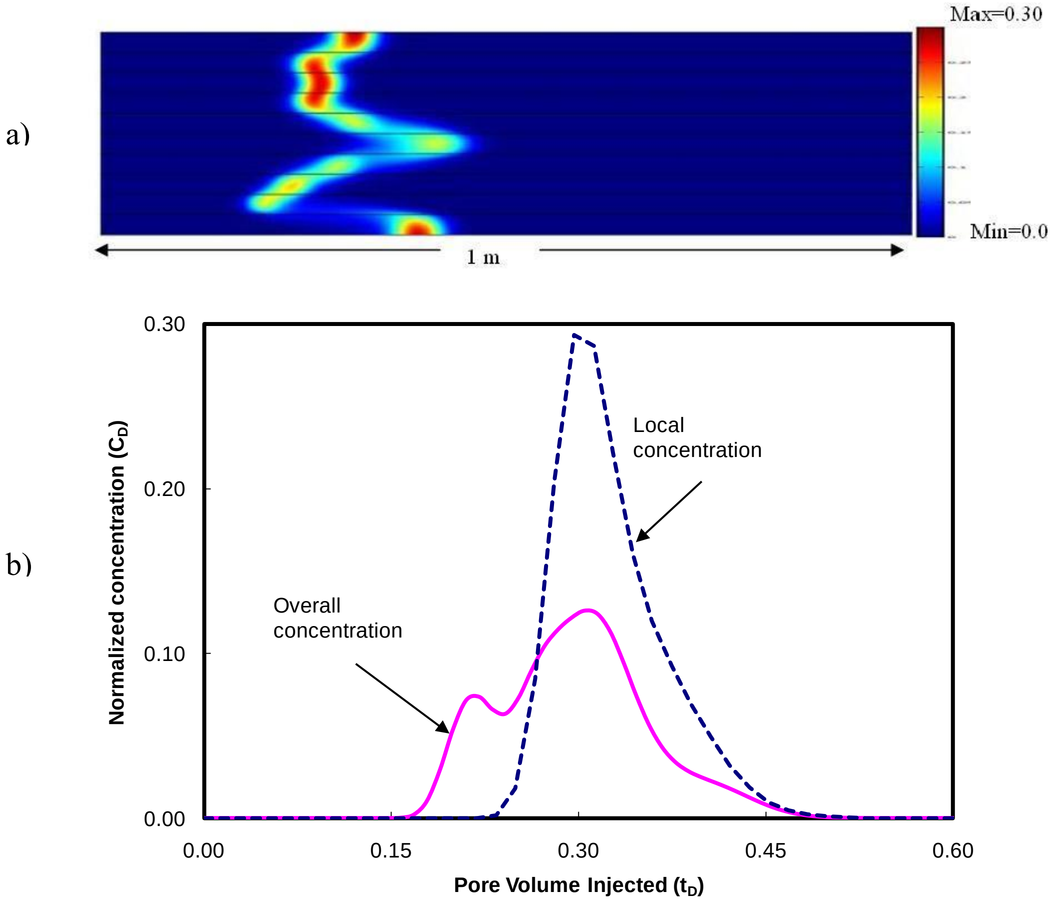

Figure 2.4: Comparison of transmission concentrations in porous media with ten uniform layers, for the case of small mixing. a) Concentration profile scaled to injected concentration, b) Concentration histories at $x = 0.3$ m. The local concentration is the effluent from layer 6.

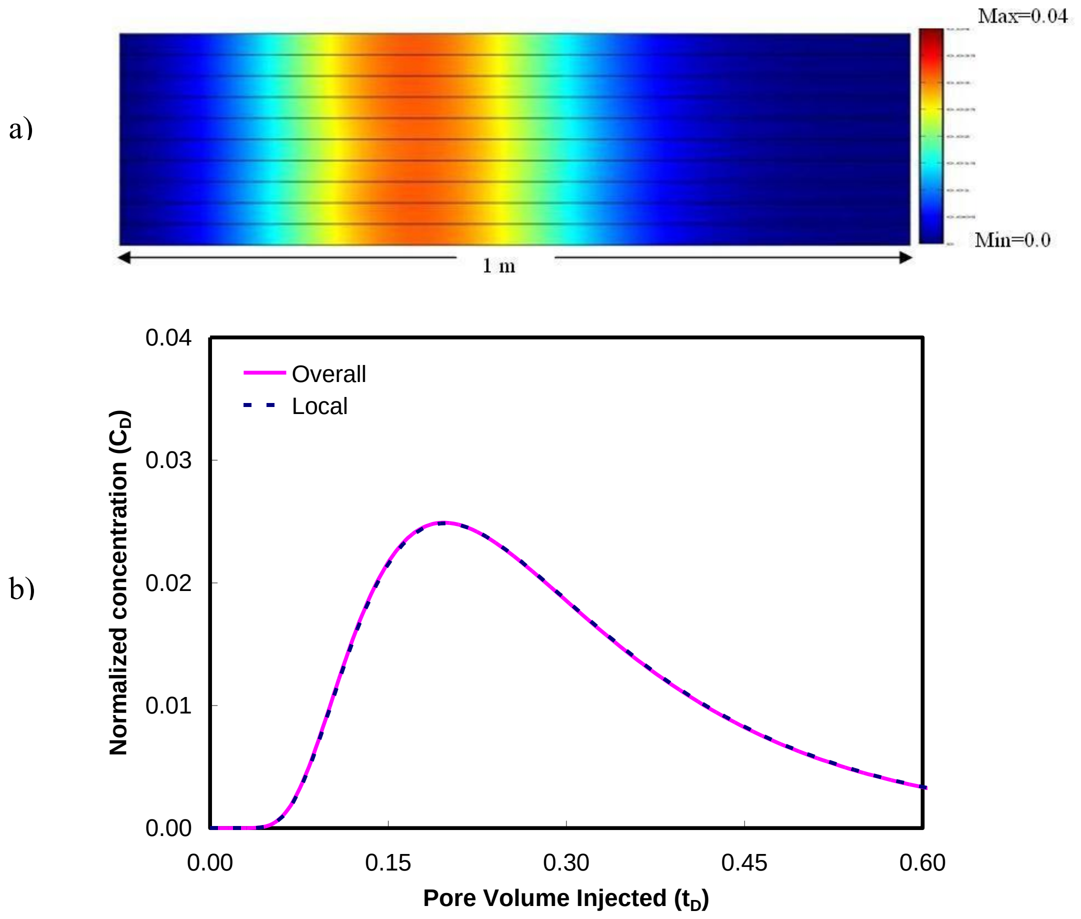

Figure 2.5: Comparison of transmission concentrations in porous media with ten layers, for the case of large mixing. a) Concentration profile scaled to injected concentration, b) Concentration histories at $x = 0.3$ m. The local concentration is the effluent from layer 6.

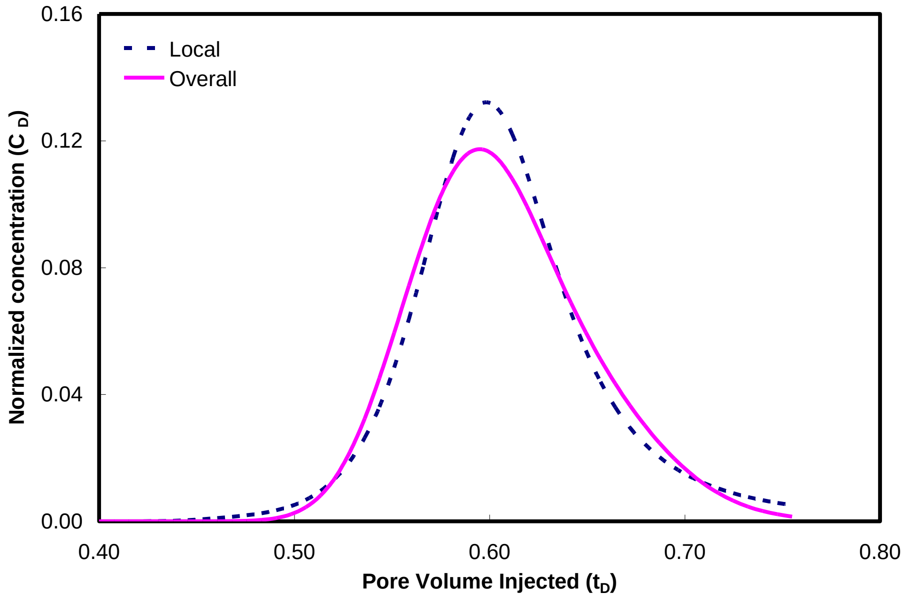

Figure 2.6: Comparison of local and overall echo concentrations measured at x=0.0 m (the inlet) for the same model as Fig. 2.4 when flow reversal occurs at *0.3 PVI*. The overall concentration history shows slightly more mixing than the local curve owing to crossflow. The local concentration is the effluent from layer 6.

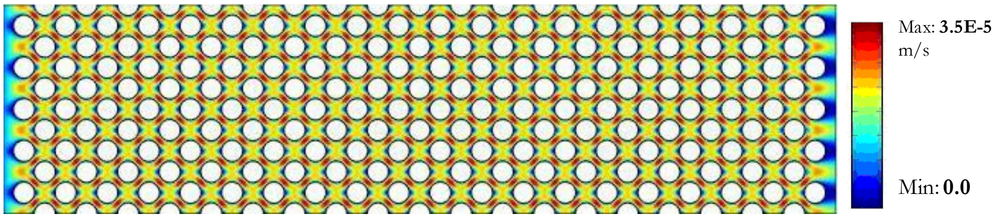

Figure 2.7: Pore velocity in 2-D pore-scale model. The local velocity is large at the pore throat and small near the grain wall.

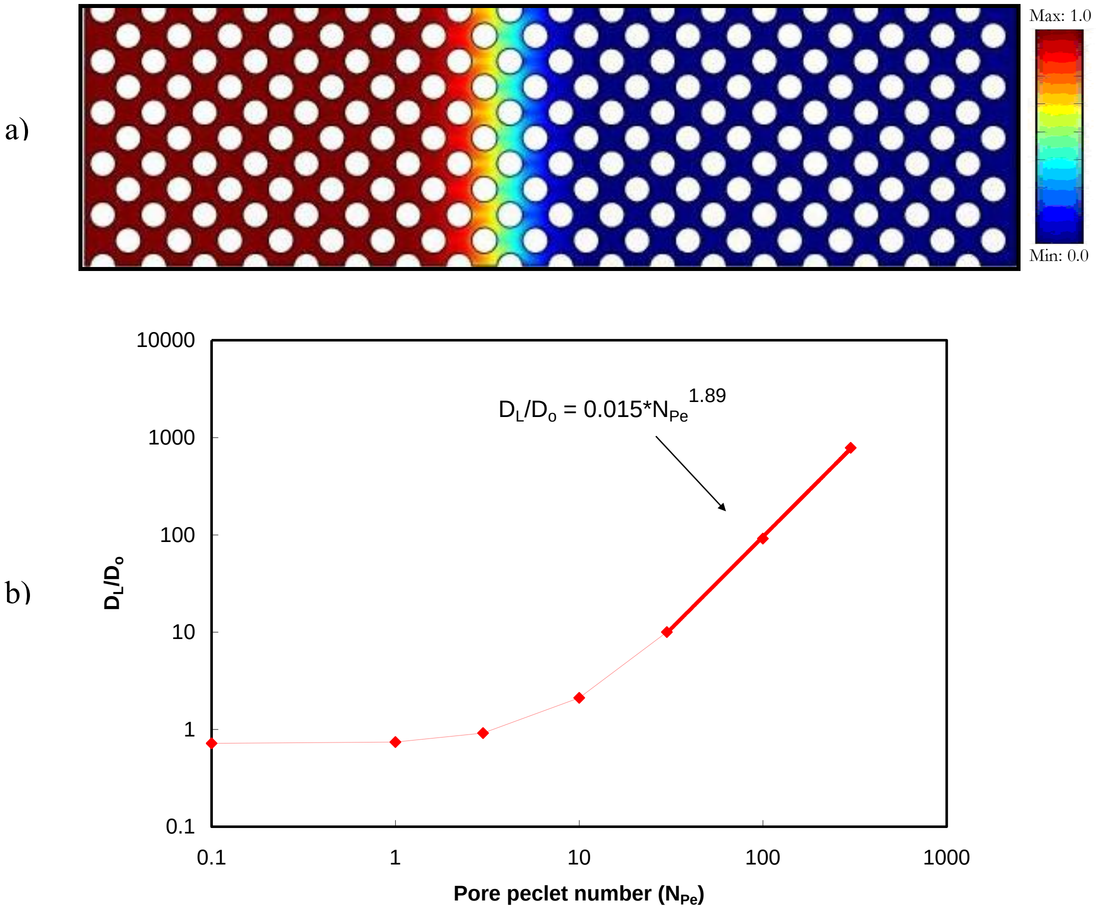

Figure 2.8: Transmission tests in homogeneous pore-scale model with uniform packing and ϕ =0.61. a) Concentration profile at 0.4 *PVI* for N_{Pe} = 3.0, b) Increase in mixing (longitudinal dispersion coefficient) with increasing pore Peclet number for concentrations at the outlet. The solid line gives the data regressed in the determination of slope.

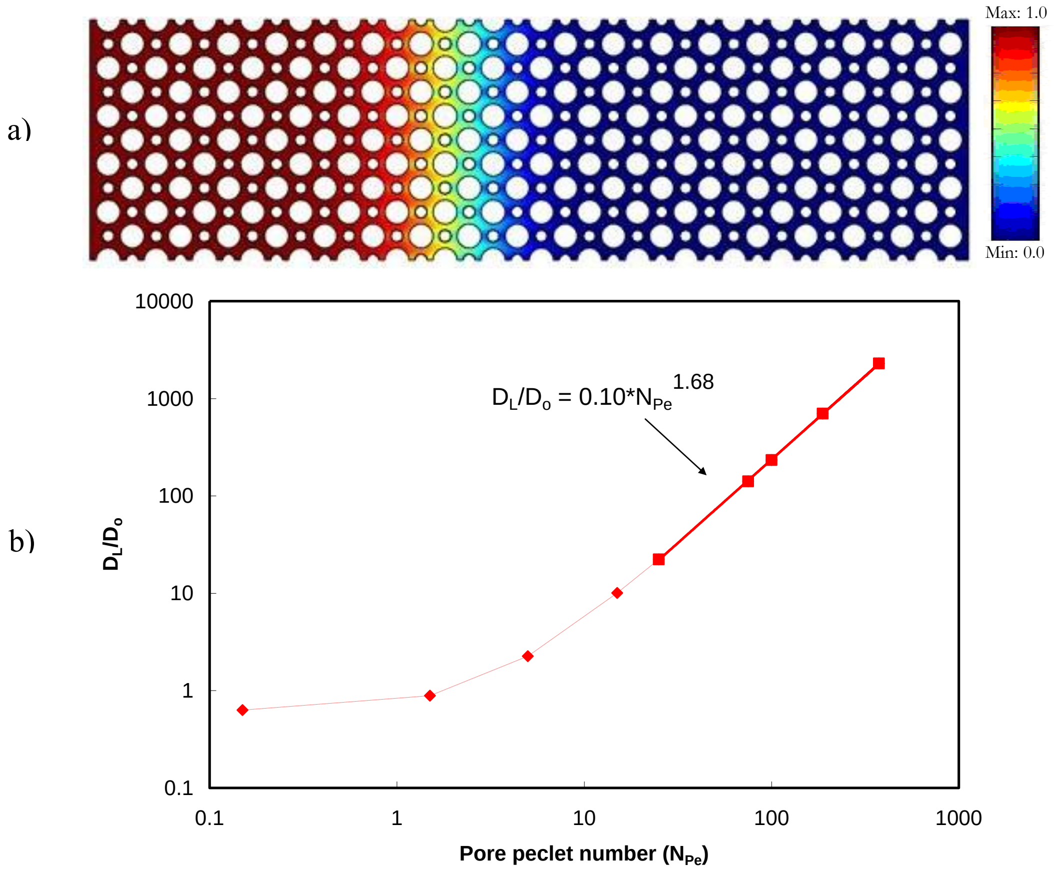

Figure 2.9: Transmission tests in homogeneous pore-scale model with non-uniform packing and ϕ =0.51. a) Concentration profile at 0.4 *PVI* for N_{Pe} = 10.0, b) Increase in mixing (longitudinal dispersion coefficient) with increasing pore Peclet number for concentrations at the outlet. The solid line gives the data regressed in the determination of slope.

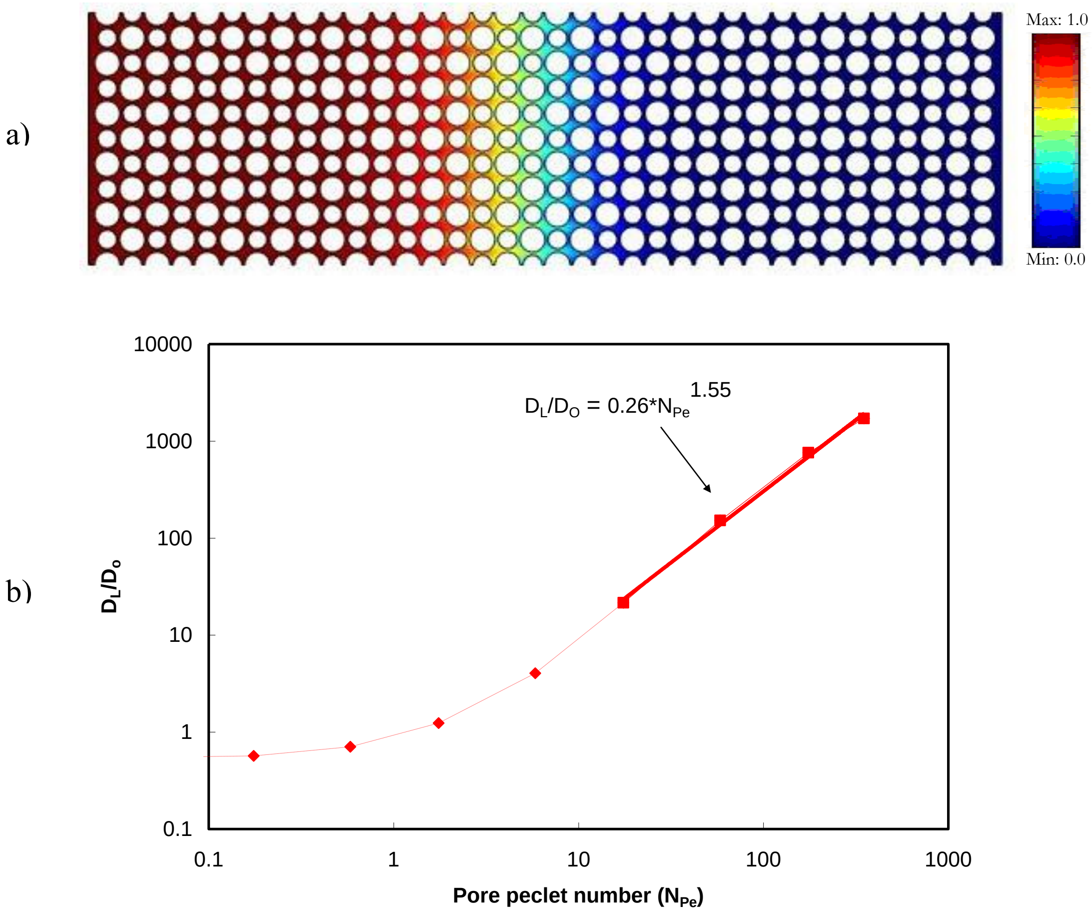

Figure 2.10: Transmission tests in homogeneous pore-scale model with non-uniform packing and ϕ =0.39. a) Concentration profile at 0.4 *PVI* for N_{Pe} = 10.0, b) Increase in mixing (longitudinal dispersion coefficient) with increasing pore Peclet number at the outlet. The solid line gives the data regressed in the determination of slope.

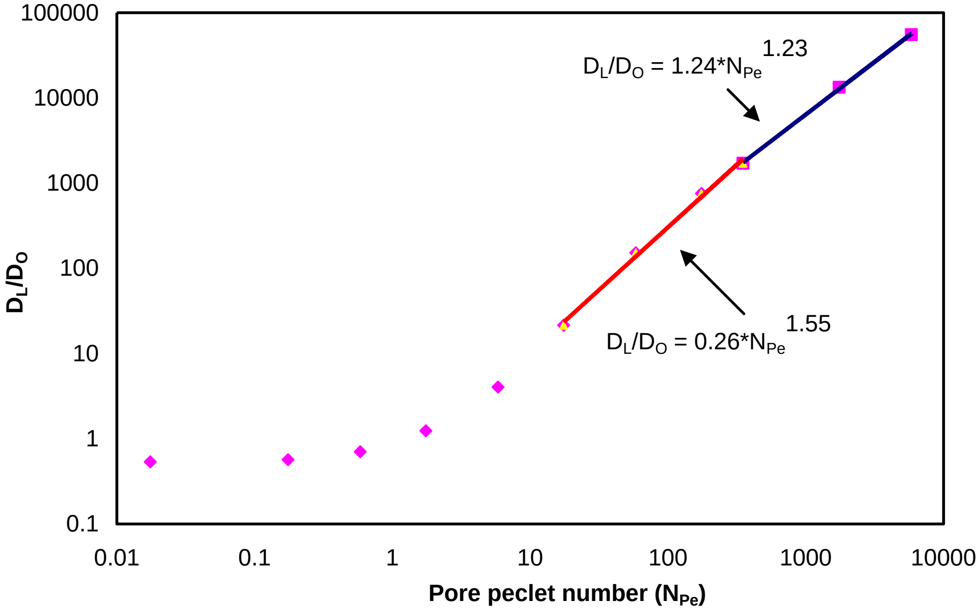

Figure 2.11: Transmission tests in homogeneous pore-scale model with non-uniform packing and ϕ=0.39. For $N_{Pe} > 400$, the scaling coefficient decreases further.

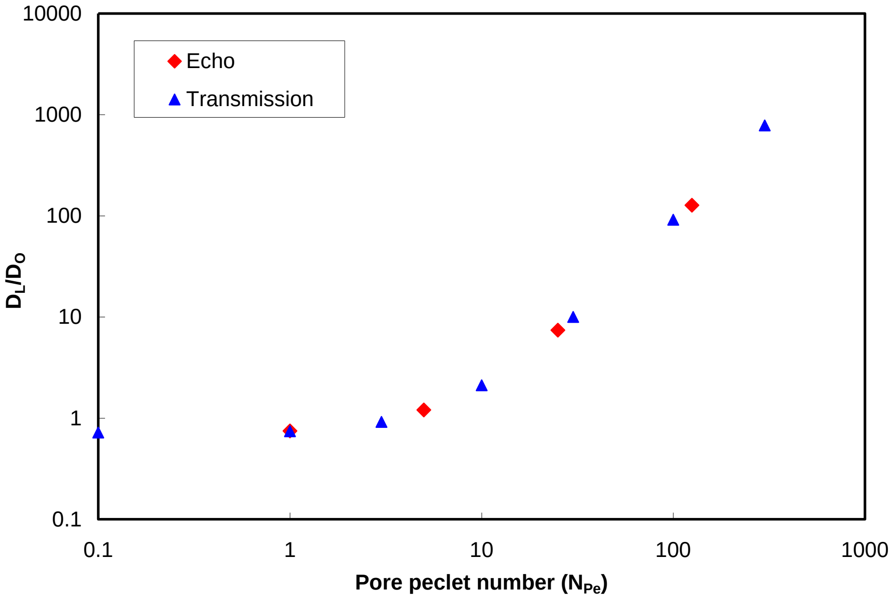

Figure 2.12: Comparison of echo and transmission dispersion at various pore Peclet numbers.

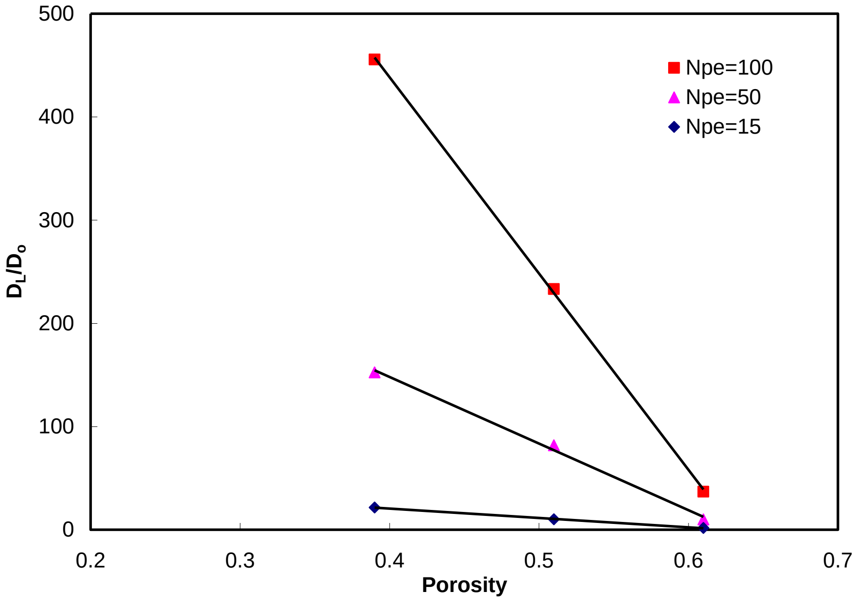

Figure 2.13: Comparison of the longitudinal dispersion coefficient with porosity and the pore Peclet number from pore-scale simulations. For fixed pore-Peclet number, the dispersion coefficient increases linearly with decreasing porosity.

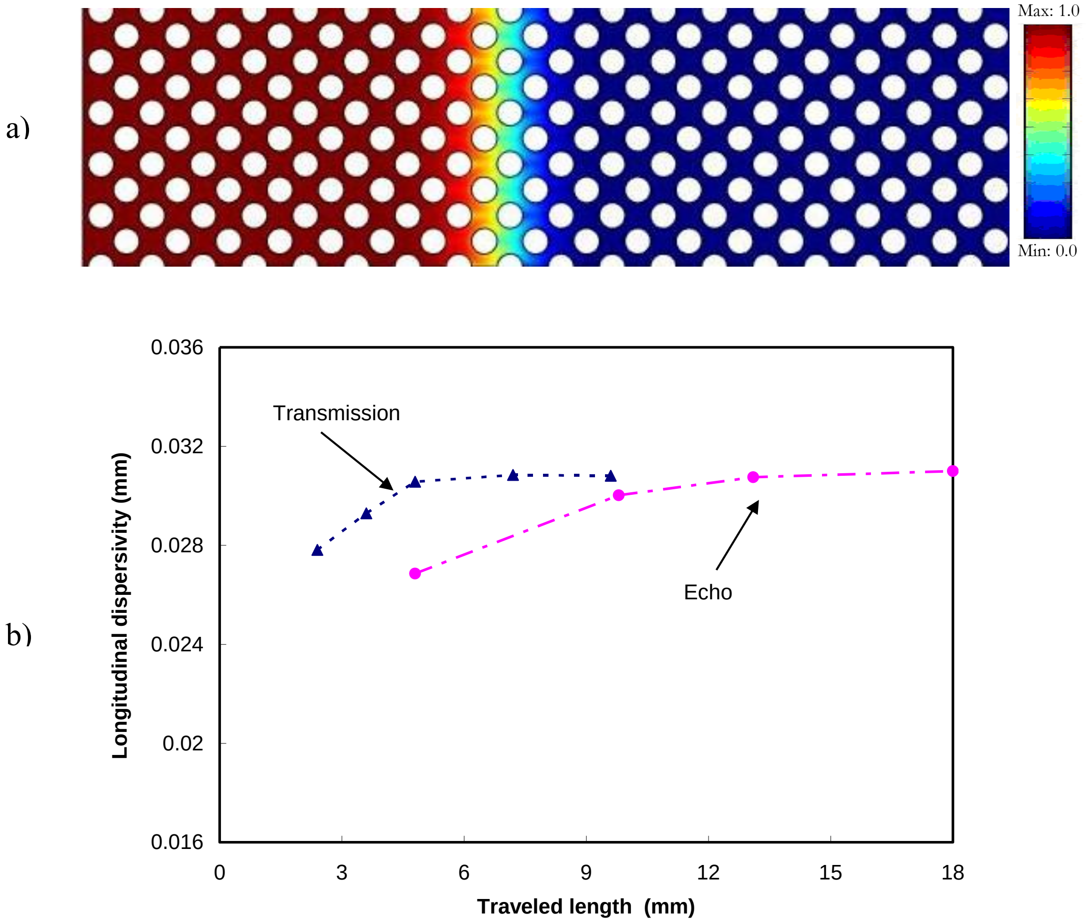

Figure 2.14: Continuous injection of solute across the entire injection well. a) Concentration profile of pore-scale model with uniform packing at *0.4 PVI*, b) Resulting echo and transmission dispersivities versus mean distance traveled by the solute.

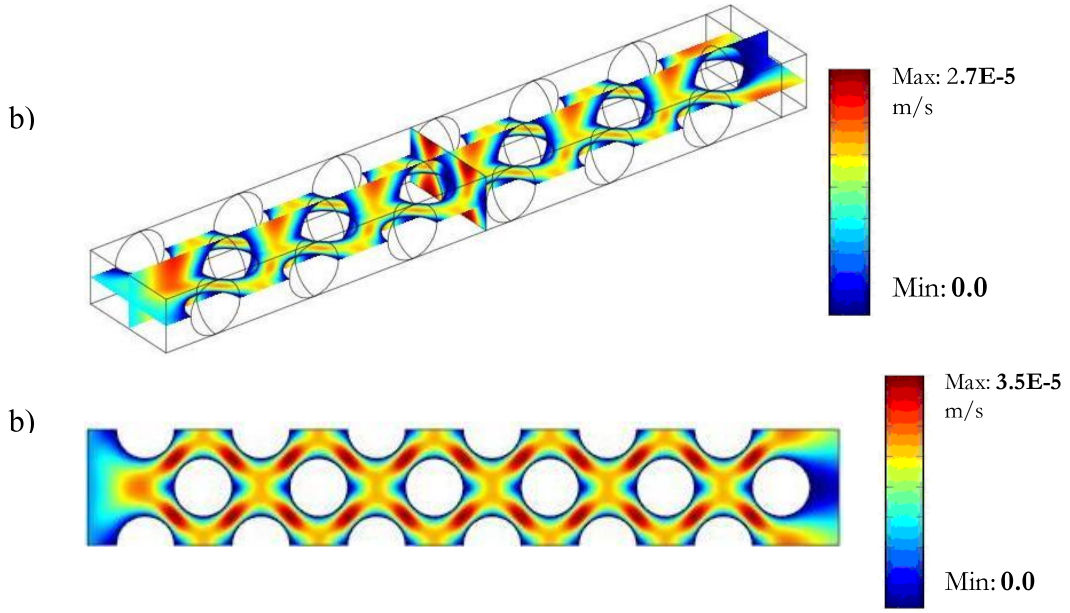

Figure 2.15: a) Pore velocity in three-dimensional pore-scale model, and b) cross-section at the mid-point of the three-dimensional model.

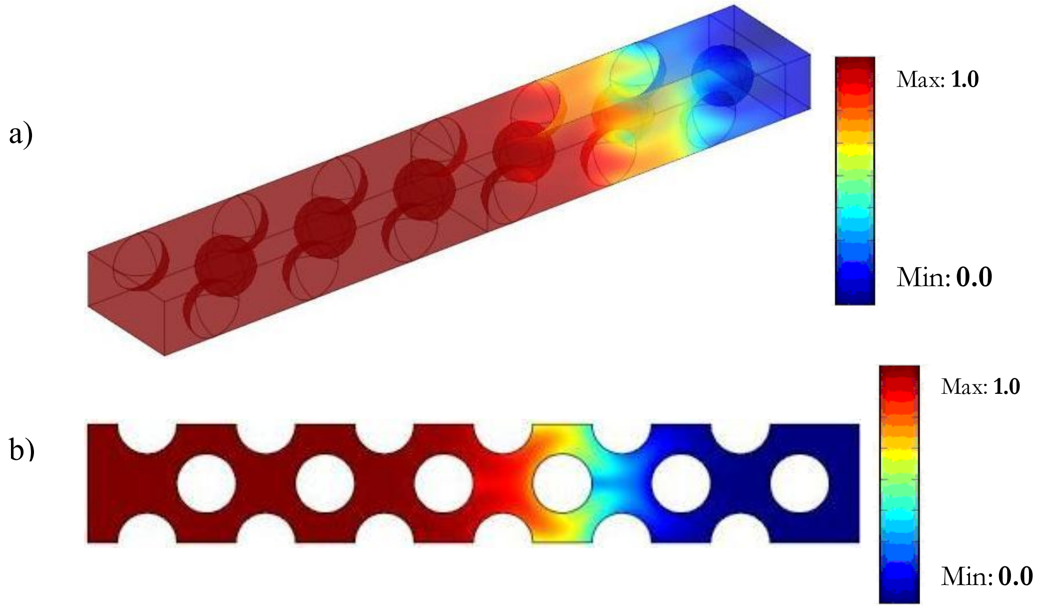

Figure 2.16: Concentration profile in a) three-dimensional model at *0.8 PVI*, and b) concentration profile in cross-section at the mid-point of the three-dimensional pore-scale model.

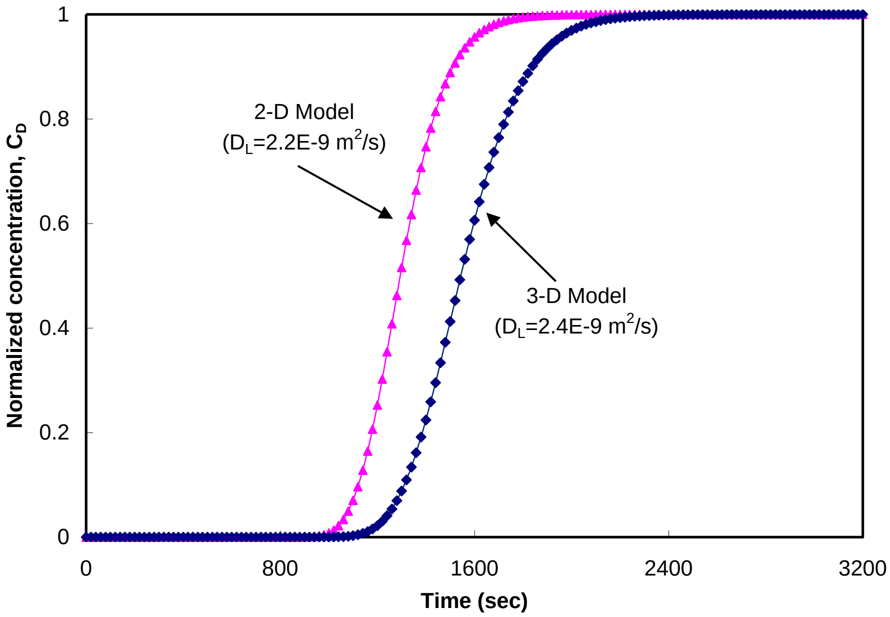

Figure 2.17: Comparison of two-dimensional and three-dimensional concentration histories for models of Figs. 2.16a, and a two-dimensional model similar to the cross-section of Fig. 2.16b.

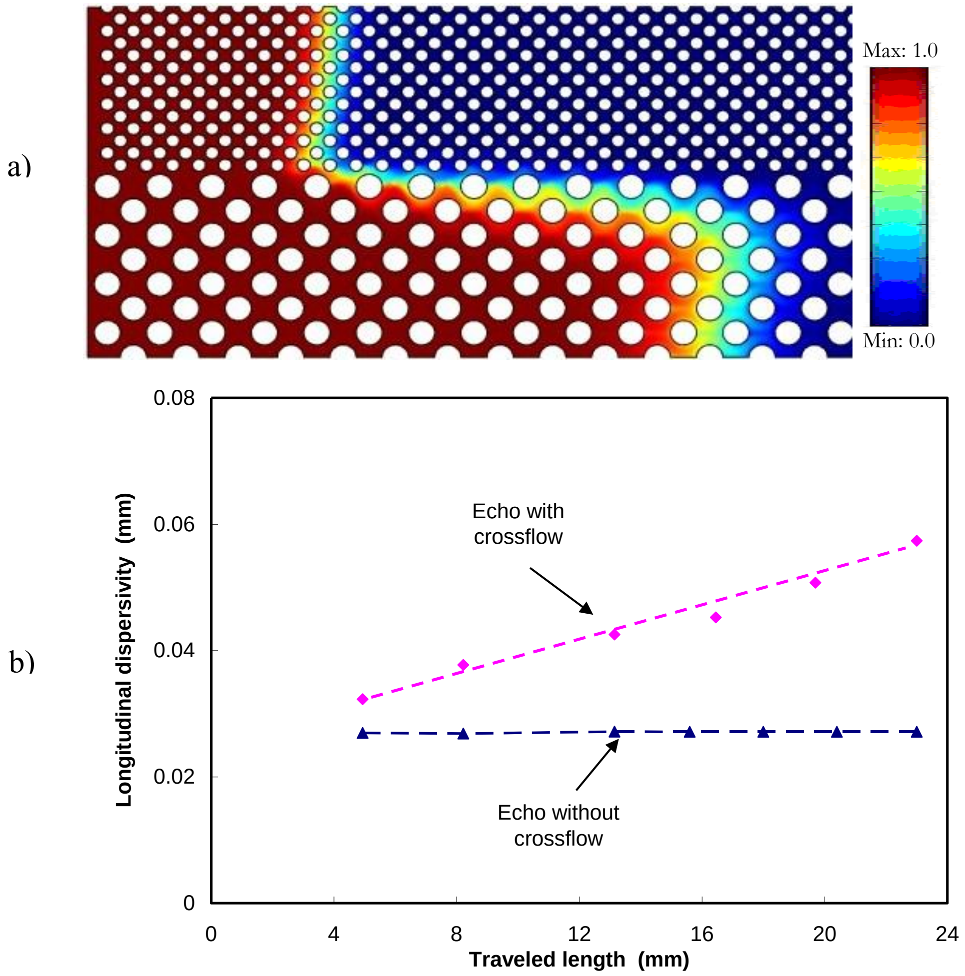

Figure 2.18: Continuous injection of solute across the two-layered pore-scale model. a) Concentration profile of pore-scale model with uniform layered packing at *0.45 PVI*, and b) resulting echo longitudinal dispersivities versus mean distance traveled by the solute.

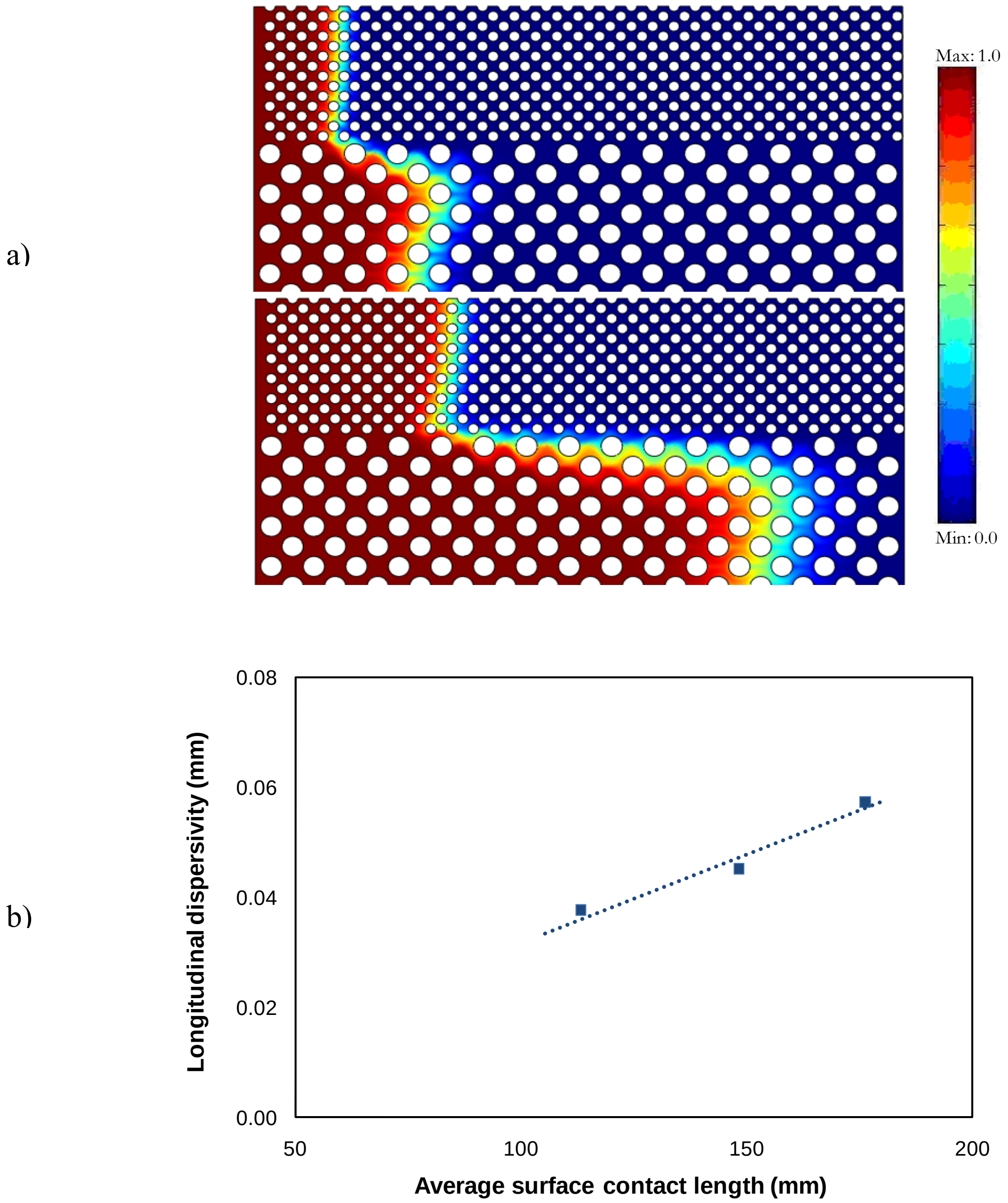

Figure 2.19: Influence of the increased surface contact area on the echo longitudinal dispersivity. a) Concentration profile at different traveled lengths, b) resulting echo longitudinal dispersivities versus mean surface contact area.

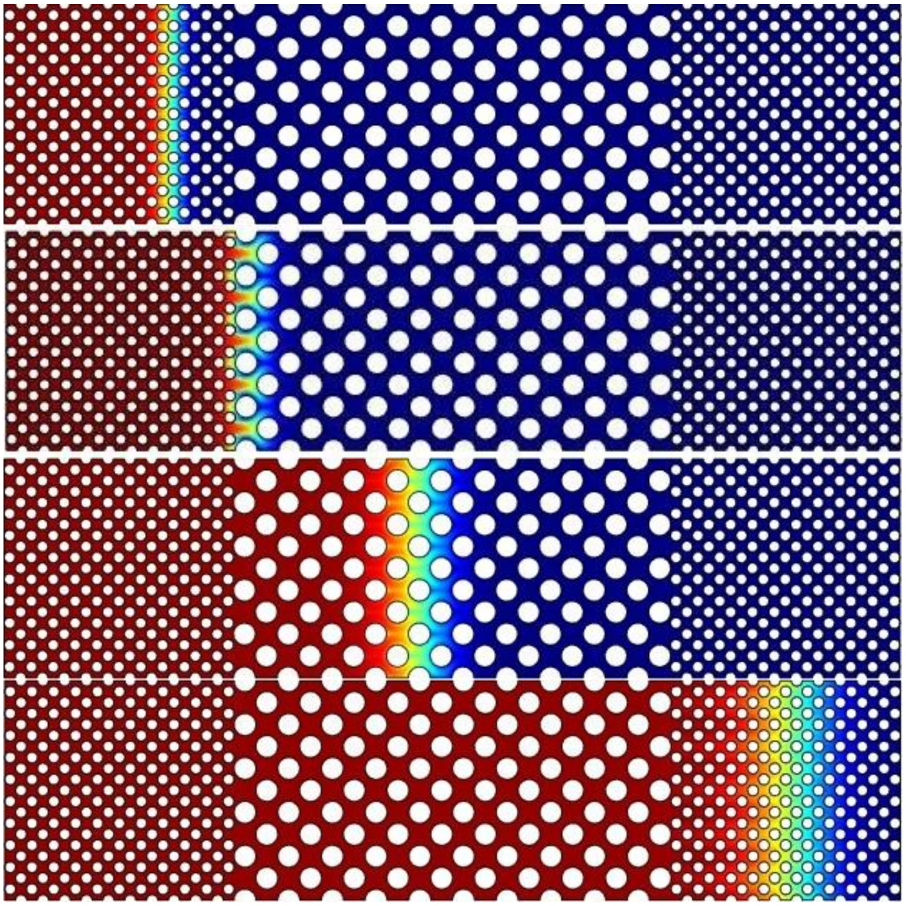

Figure 2.20: Continuous injection of solute across a pore-scale model with a series of changing grain sizes. Concentration profiles at four time injection times (PVI) are given to illustrate mixing with traveled length

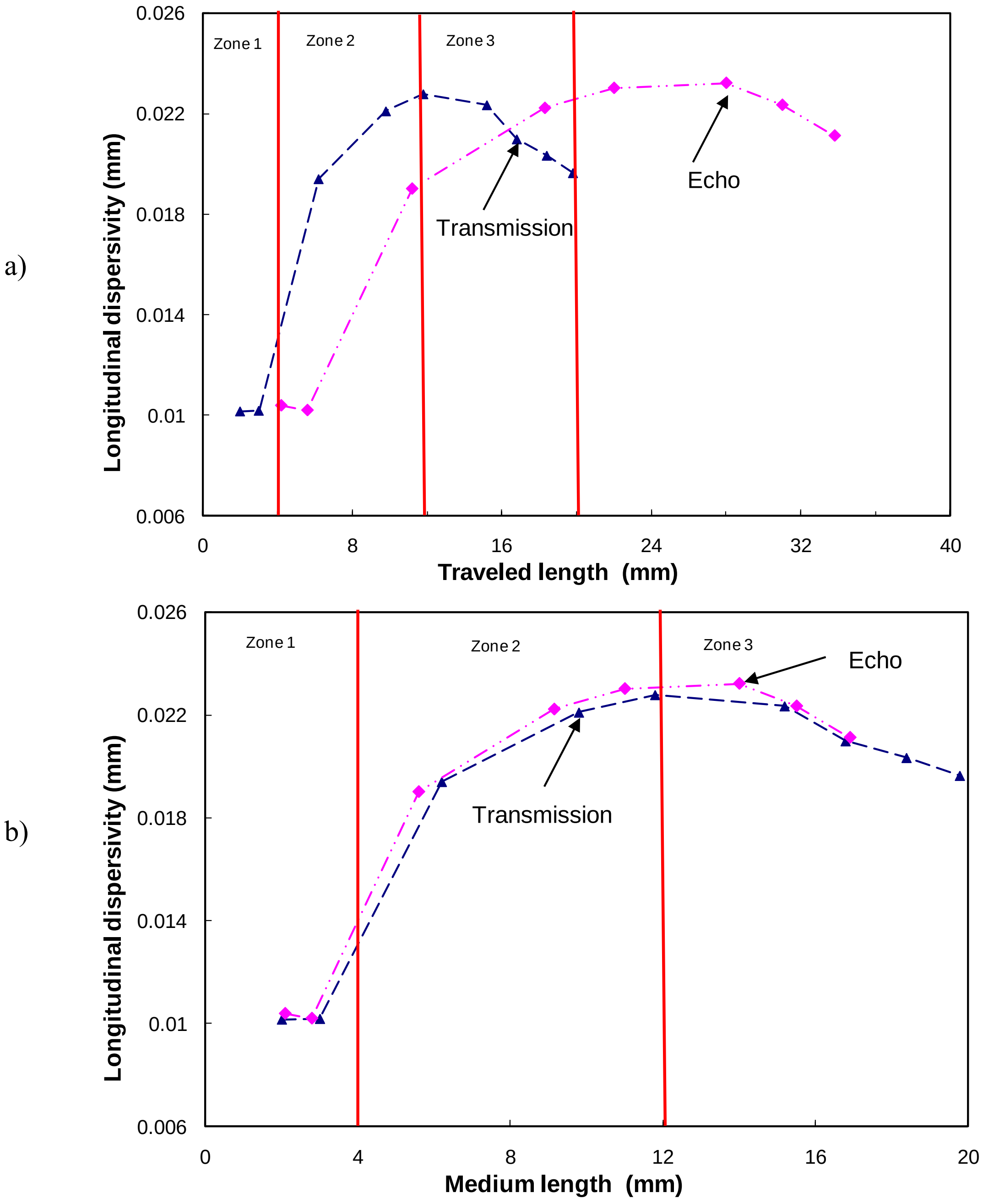

Figure 2.21: Continuous injection of solute into the pore-scale model of Fig. 2.20. Both echo- and transmission-longitudinal dispersivities increase within the middle region, but decrease slowly at the trailing region. a) Solute traveled length, b) porous medium length.

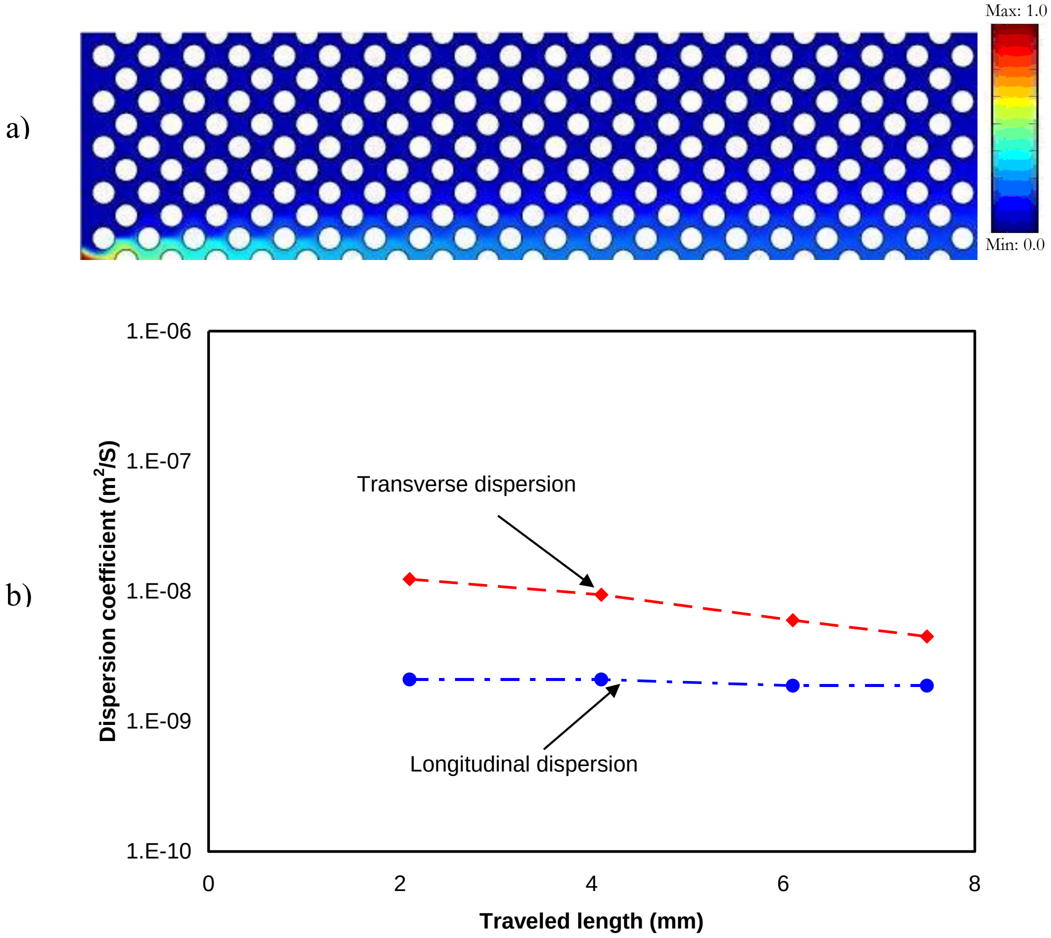

Figure 2.22: Continuous injection of solute in the bottom of an injection well. a) Concentration profile of pore-scale model with uniform packing with ϕ =0.61 at *2.0 PVI*, and b) resulting transverse and longitudinal transmission dispersivities versus mean distance traveled by the solute.

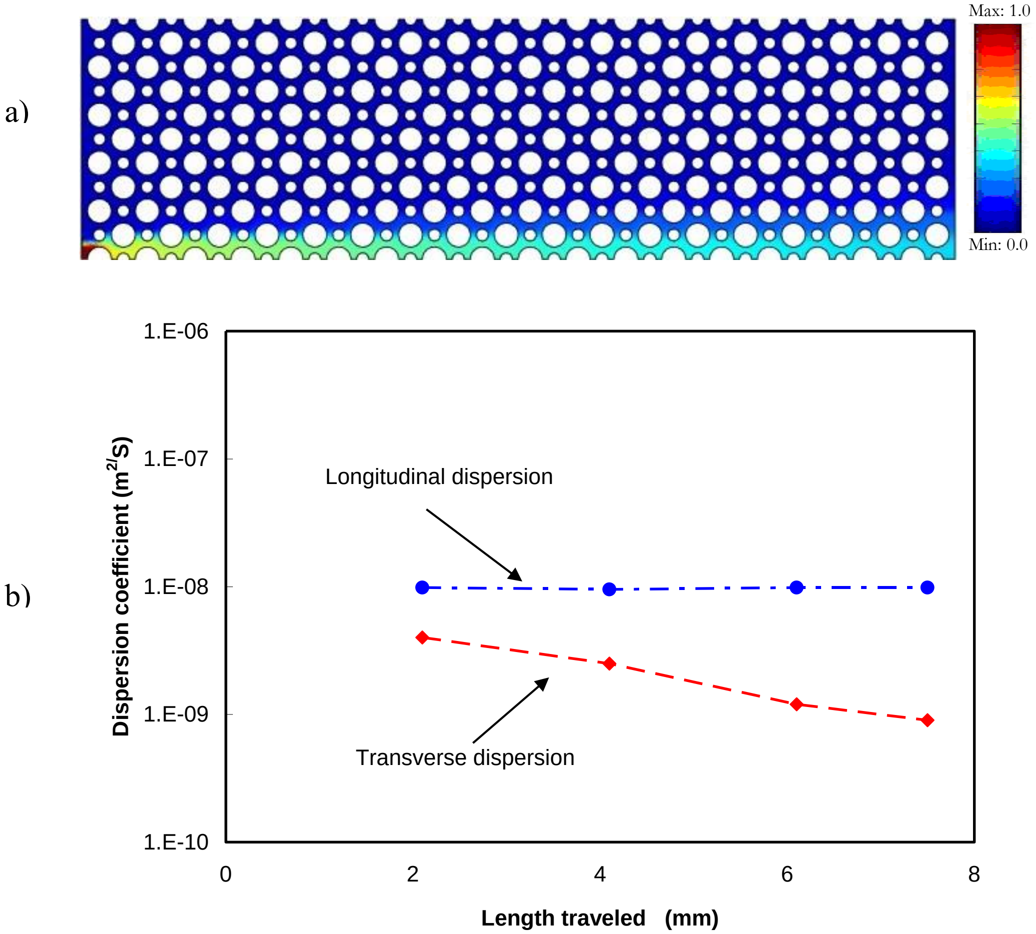

Figure 2.23: Continuous injection of solute in the bottom of an injection well. a) Concentration profile of pore-scale model with non-uniform packing with ϕ =0.51 at *2.0 PVI*, and b) resulting transverse and longitudinal transmission dispersivities versus mean distance traveled by the solute.

Chapter 3: Scaling Dispersion in Heterogeneous Porous Media

This chapter presents a method to estimate local dispersivity in a reservoir as function of scaling groups and major reservoir properties. Dimensionless groups were derived from an inspectional analysis for a first contact miscible (FCM) gas flood in a 2-D heterogeneous reservoir.

3.1 OVERVIEW

It has been well known that dispersion is scale dependent and its magnitude is increased as traveled distance is increased; where, reservoir heterogeneity is the primary reason for scale dependency of dispersivity.

Different approaches have been used to model scale-dependent dispersivity in porous media. In all previous research studies, dispersivity in porous media has been modeled using heterogeneity parameters; and transmission dispersivity is considered as reservoir mixing. Pickens and Grisak (1981a) examined a scale-dependent dispersivity model in heterogeneous porous media. Gelhar and Axness (1983) used stochastic continuum theory to analyze dispersive mixing from 3-D flow in a heterogeneous porous medium. They modeled scale-dependent dispersion in heterogeneous porous media as function of correlation lengths and variation of the medium's conductivity. Arya *et al.* (1988) developed a scale-dependent dispersivity model that scales dispersivity as function of reservoir heterogeneity. Wheatcraft and Tyler (1988) introduced the concept of fractal geometry to explain the scale-dependent dispersivity in heterogeneous porous media. They examined the fractal model to field-scale dispersivity and compared the results with stochastic theories. Their result indicates that most field tracer tests can be predicted using fractal heterogeneity. In all given dispersivity models, transmission dispersivity was considered as reservoir mixing; however, we know that transmission dispersivity is not actual reservoir mixing.

In this chapter we model scale dependent dispersivity as function of reservoir heterogeneity and flow property. We model averaged local dispersivity as reservoir mixing at the sampled traveled distance. Local dispersivity is not transmission dispersivity because it does not include the impact of concentration variation due to convective spreading on the estimation of reservoir mixing. In addition to reservoir heterogeneity, we also include the impact of fluid properties, reservoir dimensions, crossflow and transverse mixing on the evaluation of longitudinal reservoir mixing.

3.2 INSPECTIONAL ANALYSIS FOR FCM DISPLACEMENT PROCESS

Dimensionless scaling groups are an efficient tool to evaluate the performance of a particular process for different reservoir geometries, operating conditions, and rock and fluid properties. Scaling groups can be obtained from inspectional or dimensional analysis (Shook *et al.* 1992; Gharbi *et al.* 1998). Dimensional analysis is often based on Buckingham's π theorem, while inspectional analysis requires the original governing equations and boundary conditions of the process being modeled. In inspectional analysis, scaling factors are introduced into the governing equations and boundary conditions. The factors are then combined into dimensionless groups so that the original form of the equations is retained, and the final numbers of scaling groups are minimized.

Inspectional analysis was carried out for a first contact miscible (FCM) gas flood in a 2-D longitudinal heterogeneous reservoir. The entire demonstration of equations and derivations is given in Appendix B.

3.2.1 Assumptions and Problem Statements

Main assumptions that we made to scale dispersion process are incompressible fluids, single-phase flow, two-dimensional x- and z- geometry, uniform and constant porosity, no chemical reactions, negligible adsorption, and no gravity. Some of these assumptions could be relaxed, but we felt that the most significant factors that affect dispersion are included. The top and bottom of the reservoir are no flow boundaries. The injection well is constant rate, while the producer is constant pressure. We used a simple mixing rule to calculate viscosity of the multi-component single-phase mixtures (see Appendix B).

3.2.2 Governing Equations

The governing equations for FCM flow are given by component material balances, the continuity (pressure) equation, and auxiliary relations such as Darcy's law, the dispersion tensor, and a viscosity mixing rule. The material balance equations using the assumptions stated previously are given by,

$$\frac{\partial}{\partial t}\phi\sum_{i=1}^{n_c} c_i + \nabla\cdot\sum_{i=1}^{n_c} c_i\vec{u} - \nabla\cdot\phi\sum_{i=1}^{n_c}\vec{\vec{D}}_i\cdot\nabla c_i = 0 \qquad i = 1,\ldots,n_c \qquad (3.1)$$

where ϕ is formation porosity, C_i is component's concentration, $\vec{u}$ is velocity vector and $\vec{\vec{D}}_i$ is the dispersion tensor. The continuity equation is given by,

$$\nabla \cdot \vec{u} = 0 \tag{3.2}$$

where the velocity in Eqs. (3.1) and (3.2) is replaced by Darcy's law,

$$\vec{u} = -\frac{k}{\mu_m}(\nabla P) \tag{3.3}$$

where k is the medium's permeability, μ_m is the mixture viscosity and P is the pressure. Equation (3.3) assumes no gravity. The viscosity in Eq. (3.3) is the viscosity of the single-phase mixture, and is estimated by a simple mixing rule equation as shown:

$$\mu_m = \left[\mu_o^{-1/4} + \beta(\mu_s^{-1/4} - \mu_o^{-1/4})\right]^{-4} \tag{3.4}$$

where μ_s is the solvent viscosity and μ_o is the oil viscosity and β is the dimensionless solvent concentration. Last equation is the dispersion equation for flow in porous media and is given by,

$$\vec{\vec{D}}_i = \frac{D_i^o}{\phi F} + \frac{\alpha_i \vec{u}}{\phi}. \tag{3.5}$$

where D_i^o is the molecular diffusion of component i, α_i is the dispersivity of component i, and F is the formation resistivity factor. We neglect the diffusion term of dispersion equation because we assume velocity is larger than 0.03 m/day (Lake, 1989).

3.3 FINAL DIMENSIONLESS SCALING GROUPS

We obtained seven dimensionless parameter groups from the inspection analysis. The first four scaling groups are based on the governing equations for FCM flow and the last three are used to describe the statistical properties of the reservoir heterogeneity. Independent dimensionless groups such as pore-volume injected and dimensionless distances are not needed. The dimensionless pressure group is also not needed because we assume that flow is always FCM (or MCM), and viscosity is only dependent on composition. Changing the mean permeability increases reservoir pressure, but the magnitude and variation of velocities remain constant since our injection velocity is constant. The off-diagonal term of the dispersion tensor (D_{xz}) is also assumed to be negligible, although we do account for velocities in the transverse direction.

3.3.1 Scaling Groups from FCM Flow

From inspectional analysis of the governing equations and boundary conditions we obtained four independent dimensionless groups (Garmeh and Johns, 2009). Scaling groups are given as:

Longitudinal Peclet Number: The first group is the Peclet number, which is given by,

$$N_{pe_l} = \left[\frac{v_{inj} L}{D_{xx}} \right], \tag{3.6}$$

where L is the permeable medium length in the primary flow direction (x-direction), v_{inj} is the injection pore velocity, and D_{xx} is the longitudinal dispersion coefficient.

For petroleum reservoirs, L is typically taken to be the distance between wells. The Peclet number is the ratio of the characteristic times for dispersive transport of a particle in the longitudinal direction to convective transport in the same direction. A Peclet number of zero means that dispersive transport completely dominates over convection.

Equation (3.6) can be approximated to account for the effect of numerical dispersion. Substitution of Eq. (C.34) from Appendix C into Eq. (3.6) gives,

$$N_{pe} \approx \frac{2L}{2\alpha_L + \Delta x} \tag{3.7}$$

where $v_{inj} \approx |v| \approx v_x$, $\alpha_T v_z^2 / |v| << \alpha_L v_x^2 / |v|$, and time step sizes are small. All of these assumptions are excellent since the velocity in the transverse direction is small compared to the longitudinal direction, and we use a Courant number less than 0.05 (see Appendix C). We further assume that the diffusion term in Eq. (3.5) is small compared to the other terms. The dispersivity α_L in Eq. (3.7) is the physical dispersivity that can be input to simulation

Dispersion Number: The next group is the dispersion number,

$$N_d = \left[\frac{L}{H} \sqrt{\frac{D_{zz}}{D_{xx}}} \right], \tag{3.8}$$

where H is the permeable medium thickness in the transverse direction, and D_{zz} is the transverse dispersion coefficient. The dispersion number is the square root of the ratio of the time scales for a particle to be transported a distance H by transverse dispersion to that transported a distance L by longitudinal dispersion. A dispersion number of zero indicates that there is no transverse mixing so that dispersivity will be constant with distance traveled (no scale effect). Larger dispersion numbers give increased scale effects. Equation (3.8) can account for numerical dispersion by substitution of Eqs. (C.34) and (C.36) from Appendix C into Eq. (3.8) to obtain,

$$N_D \approx \frac{L}{H}\sqrt{\frac{2\alpha_L |v_z / v_x|^2 + 2\alpha_T + |v_z / v_x| \Delta z}{2\alpha_L + \Delta x}}, \tag{3.9}$$

where we made the same assumptions as for the Peclet number. The dispersion number therefore is dependent on dispersivities and grid-block sizes in both directions, as well as on the ratio of the transverse to longitudinal velocities. The dispersivities in Eq. (3.9) are physical dispersivities that are input directly to simulation if needed. Typical values of the dispersion number for real reservoirs ranges between about 1.0 and 10.0. For example, $N_D \approx 3.3$ when $\Delta x = \Delta z = 0$, $L/H = 10$, $v_z / v_x = 0.1$, and $\alpha_T / \alpha_L = 0.1$.

Effective Aspect Ratio: Effective aspect ratio also controls the dispersivity, and is given by,

$$R_L = \left[\frac{L}{H}\sqrt{\frac{k_z}{k_x}}\right], \tag{3.10}$$

where k_x is the permeability in the primary direction of flow (longitudinal direction), and k_z is the transverse permeability. The effective aspect ratio is the ratio of the time required for fluid to cross the reservoir in the longitudinal direction to that in the transverse direction. If the aspect ratio is large, fluid fluctuations in the transverse direction decay rapidly compared to the longitudinal direction. An aspect ratio greater than about ten implies that vertical equilibrium can be achieved quickly (Lake 1989). A zero aspect ratio means there can be no cross flow in the reservoir.

Mobility Ratio: The mobility ratio of the reservoir oil and injected solvent also significantly impacts the level of mixing in a reservoir. The mobility ratio often has many definitions, but with the assumptions of constant viscosity and FCM flow, there is only one definition given by,

$$M = \left[\frac{\mu_o}{\mu_s} \right], \tag{3.11}$$

where μ_o is the oil viscosity and μ_s is the solvent or gas viscosity. The mobility ratio is the ratio of oil to solvent viscous forces. Mobility ratios greater than 1.0 are unfavorable in that gas channeling will increase through high permeability layers.

Although we have defined the mobility ratio based on oil and gas, any fluids can be used as long as they are nearly miscible. A completely immiscible phase can also be present as long as it is immobile. For example, our model can also be used to model mixing that occurs in a tracer test of an aquifer, where the mobility ratio is 1.0. It could also be used for a water-soluble tracer test in a reservoir water flooded to residual oil saturation, where the permeability, porosity, and pore velocities are modified to account for the reduction in pore space available for water flow. Similar adjustments could be made for FCM (gas-oil) flow at irreducible water saturation.

3.3.2 Scaling Groups from Reservoir Heterogeneity

Reservoir heterogeneity is included in our scaling groups by introducing the variation and correlation structure of the medium's permeability distribution in a 2-D model. We included the Dykstra-Parsons coefficient for permeability variation and the dimensionless correlation lengths in longitudinal and transverse direction for permeability distribution.

Dykstra-Parsons Coefficient: We use the Dykstra-Parsons coefficient (V_{DP}) to represent the permeability variance within the reservoir. Dykstra-Parsons coefficient (V_{DP}) is a dimensionless number that relates permeability distribution to the standard deviation of its mean (Dykstra and Parsons, 1950). The equation is in the following form:

$$V_{DP} = \frac{\bar{k} - k_\sigma}{\bar{k}}, \tag{3.12}$$

where $\bar{k}$ is the median permeability and k_σ is the permeability at one standard deviation below median on a log-probability plot. An alternative V_{DP} estimator for a log-normal permeability distribution is (Jensen *et al.*, 2000):

$$V_{DP} = 1 - \exp(-\sigma_{\ln k}), \tag{3.13}$$

where $\sigma_{\ln k}$ is the sample standard deviation of *lnk*. The Dykstra-Parsons coefficient must lie between 0.0 and 1.0, and is zero for a completely homogeneous formation, and 1.0 for a completely heterogeneous one. Most reservoirs have Dykstra-Parsons coefficients between 0.4 and 0.9.

Dimensionless Longitudinal Correlation Length: Correlation length is the maximum length of autocorrelation between variables of the same type taken at different locations. This is also called range (correlation range), which is the distance that variables of the same type are still dependent. The auto-correlation structure is modeled using the semivariogram. The semivariogram estimates the mean of the squared difference between pairs of data points that are separated by a given distance in a direction. It is defined as

$$\gamma(\vec{h}) = \frac{1}{2n}\sum_{i=1}^{n}\left[k(\vec{x}_i) - k(\vec{x}_i + \vec{h})\right]^2 , \tag{3.14}$$

where γ is the semivariance of the permeability data, $k(x_i)$ is the permeability value at spatial location x_i, $k(x_i+h)$ is the permeability value at (x_i+h) , $\vec{h}$ is the lag distance vector in a specified direction and n is the number of data pairs used to estimate the semivariance (Deutsch, 2002).

Sill, nugget and range are the components of a semivariogram model. The sill is the maximum value of semivariogram model at large distance. It is the maximum variability of the medium. The nugget is the value of the semivariogram extrapolated to zero lag distance. It shows the uncorrelated variance. The range is the lag distance that a semivariogram approaches to the sill and is normalized by length scale L in longitudinal direction. Appendix E shows the code's user guide and the semivariogram model that is used to generate permeability field.

Dimensionless Transverse Correlation Length: The correlation length in transverse direction has the same property as horizontal direction except that it relates to the correlation of permeability distribution in the vertical direction and is normalized by *H*.

The four dimensionless groups of flow equations are similar to those derived by Gharbi *et al.* (1998). Our result differs in that we allow for transverse velocity and numerical dispersion in the dispersion number.

3.4 SIMULATION MODEL

We performed simulations using the Computer Modeling Group's GEM simulator (User's manual 2008) to validate the scaling groups by changing the parameters that go into each scaling group. Local dispersivities estimated from each simulation should collapse to one curve if the values of the scaling groups are the same.

The reservoir model simulated is a 2-D heterogeneous reservoir as previously described and illustrated in Figure 3.1. The base case model is 1600 ft by 100 ft with a Cartesian grid of 512 x 64 grid-blocks in the *x*- and *z*-directions respectively. For simplicity, the sizes of all grid blocks are equal. The injection pore velocity is held constant at 0.5 ft/day as this value does not affect the estimated dispersivities. We generate permeability fields for the reservoir using FFTSim (Jennings *et al.* 2000) by assigning correlation lengths, mean permeability, and the Dykstra-Parsons coefficient. The permeability realizations are generated with an exponential semivariogram model. The mean permeability in all simulations is 200 md, but as explained previously changing this value does not affect the estimated dispersivities.

All simulations are performed by injecting 2.0 pore volumes of solvent to ensure sufficient increases in the observed concentrations in each grid block. The local concentration histories for each grid-block are then matched to the solution of the 1-D convection-dispersion equation by varying the longitudinal dispersivity. Once a best fit is obtained, the estimated dispersivity is representative of local mixing in that grid block. The estimated dispersivities for each grid-block are then averaged over a cross-section of the reservoir at a fixed longitudinal distance. The averaged local dispersivities are then normalized by L using $\alpha_D = \alpha / L$.

Local dispersivities are estimated at a constant averaged velocity over a cross-section, which is equal to the injection velocity. In a heterogeneous reservoir model local velocity is not constant and it depends on the permeability value of the corresponding grid-block. However, a local velocity is not the representative of the velocity along the streamline to that point; therefore an averaged velocity is used to estimate local dispersivity. Figure 3.2 compares the estimated local dispersivity versus traveled distance for constant and variable local velocities. The comparison shows that the difference is not significant.

For all simulations, we take N_{pe} equal to 512, which represents a constant value of dispersivity present in the simulations. From Eq. (3.7) the Peclet number can be held fixed at this value by changing the value of longitudinal dispersivity input to the simulations and the grid-block size. This constant level of dispersivity is not representative of the actual mixing that occurs in the reservoir, and is therefore subtracted out of the simulated dispersivities. Figure 3.3 shows that for a fixed permeability field similar value of the dimensionless local dispersivities (α_D) are obtained after subtracting out the constant input dispersivity for three different values of the Peclet number. The curves do not exactly collapse onto each other because the velocity variations within the reservoir decrease as the grid-blocks are refined (standard deviation in v_x decreased by 5% from a Peclet number of 1024 to 2048). Smaller velocity variations induce less mixing. There are also small differences resulting from fits to the concentration profiles in each grid block; smaller Peclet numbers tend to have smoother curves and better fits. Because we use a Peclet number of 512 for all simulations, the correction for the dimensionless local dispersivities is small at about 0.002 (inverse of the Peclet number). Figure 3.3 also shows that the local dispersivities increase with distance traveled. The dispersivity at the production well (where $x_D = 1$) is nearly 3% of the distance between the wells. The dispersivity curves show bumps, which are the result of changes in heterogeneity as the gas moves through the reservoir. These features are preserved even for a very small input Peclet number.

3.5 GROUP VALIDATION AND SENSITIVITY TESTS

3.5.1 Group validation

We performed simulations with different input parameters to validate each of the scaling groups. Table 3.1, for example, gives input parameters for five different simulation models, but where the scaling group values are the same. The average velocity anisotropy ratio input into the dispersion number (Eq.(3.9)) is determined from each simulation by calculating the anisotropy ratio for each grid block at 1.2 PVI, and then averaging these over the entire reservoir. Figure 3.4 shows that the estimated dispersivities for all five reservoirs nearly collapse onto each other, indicating the validity of the scaling groups for these simulations. This validation approach was repeated for a variety of different reservoir models and scaling groups.

There is a small difference observed between R-5 and the other cases in Figure 3.4 because the number of grid blocks in the x- and z-directions for R-5 is twice those used in the other models. The heterogeneity for all cases is identical. Thus, the small difference in R-5 is a direct result of a small difference in the ratio of v_z / v_x caused by improved accuracy in the numerical solution.

3.5.2 Sensitivity Test

The sensitivity of the local dispersivity for each scaling group, where they are varied one at a time, is given in Figures 3.5 – 3.10. Figure 3.5 shows that reservoir mixing is increased as the longitudinal correlation length is increased. A larger correlation length increases the fluid contact area with distance traveled owing to increased channeling through the more continuous layers.

The sensitivity of the dispersivities to transverse correlation length is shown in Figure 3.6. It shows that reservoir mixing is decreased as the transverse correlation length is increased, largely because the solvent injected goes into fewer and thicker layers decreasing the contact area between gas and oil.

Figure 3.7 shows that reservoir mixing increases as the Dykstra-Parsons coefficient (more heterogeneous reservoir) is increased. More heterogeneity induces greater velocity variations within the reservoir causing increased contact area between gas and oil.

The sensitivity of the dispersion number is illustrated in Figure 3.8. Reservoir mixing is not dependent on length traveled for a dispersion number of zero. A dispersion number of zero means there is no mixing in the transverse direction, so that any increase in the contact area of gas and oil in that direction does not result in increased mixing. As the dispersion number increases, the potential for scale-dependent dispersion increases. For a very large dispersion number, transverse dispersion dominates over heterogeneities and the porous media behaves as a single layer with a very large level of mixing.

The mobility ratio also greatly impacts the local dispersivities (see Fig. 3.9). Reservoir mixing increases for more unfavorable mobility ratios (larger M) because of increased gas channeling that enhances the contact area.

Last, Figure 3.10 shows that a larger aspect ratio increases reservoir mixing. As the aspect ratio increases, mixing is increased over the cross-sectional area because the transverse length decreases relative to the longitudinal length of the reservoir. Thus, for the same amount of transverse dispersion, concentrations reach the transverse boundaries quicker. Once concentrations reach the transverse boundaries over the entire reservoir, dispersion no longer increases with distance traveled, that is, local dispersivities reach an asymptotic limit. An alternative explanation for the effect of the aspect ratio on mixing is that the vertical to horizontal permeability ratio is larger as the aspect ratio is increased so that velocities in the transverse direction are increased.

3.6 LOCAL DISPERSIVITY PREDICTION FROM SCALING GROUPS

We performed over 800 simulations using GEM to estimate dispersivity as a function of the derived scaling groups. Before dispersivities can be predicted from experimental design, we first quantify and predict the ratio of the transverse to longitudinal velocities from key scaling groups so that the dispersion number in Eq. (3.9) can be explicitly determined.

3.6.1 Experimental Design to Estimate Velocity Anisotropy

From scaling analysis, the velocity ratio is primarily a function of the aspect ratio, mobility ratio, Dykstra-Parsons coefficient, and the dimensionless correlation lengths previously described.

We performed 46 experiments based on a three-factorial Box-Behnken experimental design with five scaling groups (Box and Behnken 1960). Because different permeability realizations are obtained for the same Dykstra-Parsons coefficient and correlation lengths, each experiment is repeated five times and averaged for a total of 330 simulations. This includes 100 additional simulations using random values of the scaling groups that were initially used to test the accuracy of the response function from 46 experiments (this test is given in Appendix D). A Box-Behnken experimental design for an independent quadratic design requires three levels (high, low, and intermediate) for each factor (scaling group) to capture quadratic effects. Table 3.2 lists the ranges of the dimensionless groups used in the experimental design. These values fall approximately within the 5th and 95th percentile of the scaling groups from several databases of reservoir properties (Wood *et al.* 2006, Ghomian 2008). The intermediate values are not always equal to the mean value, but are rather based on the most likely value for reservoirs.

Response surfaces are then developed based on fitting the average velocity anisotropy ratios from the 330 simulations. Figure 3.11 shows that velocity anisotropy ratios are log-normally distributed; therefore, logarithm value of velocity ratios are averaged to estimate mean velocity anisotropy ratio from each of the 330 simulations. Response surfaces are useful to estimate values of the parameter of interest as a function of the key scaling groups (Myers and Montgomery 1995). The response surface function we use is a second order polynomial given by,

$$y = \beta_0 + \beta_1 x_1 + \beta_2 x_2 + \ldots + \beta_n x_n + \sum_{i<j}^{n} \sum_{=2}^{n} \beta_{ij} x_i x_j + \sum_{i=i}^{n} \beta_{ii} x_i^2 , \tag{3.15}$$

where n is the number of scaling groups (five in this case), y is the objective function (velocity anisotropy), β_0 is the intercept constant, β_i are linear coefficients, β_{ij} and β_{ii} are quadratic coefficients, and x_i are the normalized group values. The scaling groups were normalized between -1 and +1 prior to determining the coefficients of the response function. The intermediate value is normalized linearly into a value between upper and lower limit as given

$$\bar{X} = 2 \cdot \left[\frac{(X - L_x)}{(H_x - L_x)} \right] - 1 \tag{3.16}$$

where $\bar{X}$ is the normalized value of the intermediate level, X is the dimensionless group's intermediate value, H_x is the upper level and L_x is the lower level of that dimensionless group. Normalization helps to identify the importance of each scaling group by examining the magnitude of the coefficients.

Prior to fitting, the average velocity anisotropy ratio is normalized with respect to the transverse and longitudinal length to obtain the ratio $v_{ZD} / v_{XD} = \left(L / H \right) \left(v_z / v_x \right)$. All 66 values of the velocity ratio are then used to determine the coefficients of Eq. (3.15) using inverse fitting software. Table 3.3 gives the 21 coefficients of the fitted response function. As shown in Figure 3.12, the predicted values of the dimensionless velocity ratio agree well with the simulated values. The velocity ratio v_z / v_x varies from about 0.01 to 0.16. Low values typically imply small dispersion numbers.

The importance of each group to the estimation of velocity ratio is determined by performing t-tests. Figure 3.13 shows that the longitudinal correlation length, the Dykstra-Parsons coefficient, and the aspect ratio are the most significant groups that impact the velocity anisotropy ratio. The ratio increases for example as the Dykstra-Parsons coefficient increases.

3.6.2 Experimental Design to Estimate Local Dispersivity

We next perform experimental design to predict the local dispersivity using 54 experiments based on a three-factorial Box-Behnken design for six factors. Because different permeability realizations are obtained for the same Dykstra-Parsons coefficient and correlation lengths, each experiment is repeated five times and averaged for a total of 270 simulations. Figure 3.14 presents an illustration of estimated averaged dispersivity from five realizations. Table 3.4 lists the range of the values used for each dimensionless group and their normalized values.

We fit a response surface using Eq. (3.15) to the dimensionless local dispersivities obtained at the production well ($x_D = 1$). Because the inverse of the Peclet number is subtracted from the dispersivities, there are six remaining scaling groups to fit the response function. There are, therefore, 28 coefficients in the response function that must be determined (see Table 3.5). We also determine a response function at intermediate values of the dimensionless distance ($x_D = 0.25,\ 0.50,\ 0.75$). The coefficients for these additional response functions can be found in Appendix D.

Figure 3.15 compares the predicted dispersivity values from the response function (at $x_D = 1$) to the simulated values. The agreement is good. We test the accuracy by performing over 116 new simulations using random values of the scaling groups within the minimum and maximum range given in Table 3.4. This test is severe since the values of the scaling groups from experimental design vary three at a time; whereas in these simulations all scaling groups are varied (values of the scaling groups are given in Appendix D). Figure 3.16a shows that the predicted dispersivities for these test simulations agree reasonably well with the simulated values, although the fit is not as nearly as good as in Figure 3.15. We decided to improve this fit by including all simulations run including the test and validation runs, and refitting the response function to these additional dispersivities at $x_D = 1$. Details of all 150 experiments (750 simulations) used to determine the response function is given in Appendix D. The updated coefficients are given in Table 3.5**.** Figure 3.16b shows the improved dispersivity predictions using all simulations. Figure 3.17 shows that the Dykstra-Parsons coefficient, dispersion number, longitudinal correlation length, and mobility ratio are the most significant scaling groups that impact reservoir mixing (dimensionless local dispersivity).

3.7 SUMMARY AND CONCLUSIONS

Inaccurate modeling of reservoir mixing in compositional simulation can significantly affect recoveries in miscible floods and leads to poor predictions of reservoir performance. We derived the key scaling groups for first-contact miscible (FCM) flow and showed how they impact reservoir mixing. This research examined only local mixing, not apparent mixing caused by variation in streamline path lengths (convective spreading). Effective local mixing is important to consider because it affects the strength of the injected fluid, and can cause an otherwise multicontact miscible (MCM) flood to become immiscible. Over 800 2-D numerical simulations are carried out using experimental design to obtain a response function for dispersivity as a function of the scaling groups. Dispersivity is estimated from the response function based on well spacing and other reservoir and fluid parameters that go into the scaling groups. We also used experimental design to estimate the magnitude of the velocity in the vertical direction compared to the horizontal, because this ratio is required for estimating the dispersion number.

We showed that reservoir mixing can be enhanced as fluids propagate by the reservoir heterogeneities. The most important groups that affect mixing are the mobility ratio, dispersion number, and heterogeneity parameters, such as horizontal and vertical correlation lengths and the variation of medium's permeability. The degree to which dispersion increases with distance traveled depends on the dispersion number; large dispersion numbers can yield large dispersivities away from the injection well.

Additional conclusions are:

- Local dispersivity is scale dependent and is a function of six scaling groups; the Dykstra-Parsons coefficient, the correlation lengths in all directions, the mobility ratio, the aspect ratio, and the dispersion number.
- The scale dependence of dispersion is caused by an increase in the contact area between gas and oil with travel distance. This enhances the effect of diffusion (mixing) across this contact area.

- Mixing is increased as reservoir heterogeneity and longitudinal correlation length increase.
- Mixing is decreased as the dispersion number and aspect ratio decrease. There is no scale dependence of dispersion with distance traveled when the dispersion number is zero.
- Mixing is increased for larger mobility ratio owing to increased channeling of injected gas through the reservoir.
- Mixing is decreased as vertical correlation length increase because the solvent injected goes into fewer and thicker layers decreasing the contact area between gas and oil.

	R-1	**R-2**	**R-3**	**R-4**	**R-5**
λ_{XD}	0.25	0.25	0.25	0.25	0.25
λ_{ZD}	0.10	0.10	0.10	0.10	0.10
V_{DP}	0.60	0.60	0.60	0.60	0.60
N_D	3.30	3.30	3.30	3.30	3.30
M	5.00	5.00	5.00	5.00	5.00
R_L	6.00	6.00	6.00	6.00	6.00
N_{Pe}	512	512	512	512	512
k_z/k_x	1.00	0.36	0.141	0.063	0.063
L/H	6	10	16	24	24
v_z/v_x	0.117	0.070	0.044	0.029	0.029
Nx	512	512	512	512	512
Nz	64	64	64	64	128
Δx	1.17	1.95	3.13	4.69	4.69
Δz	1.56	1.56	1.56	1.56	0.78
α_L	0.586	0.977	1.563	2.344	2.344
α_T	0.256	0.153	0.096	0.064	0.075

Table 3.1: Scaling group values and dimensional property values for scaling groups validation.

Groups	**Low**	**Intermediate**	**High**
λ_{xD}	0.10 (-1)	0.25 (-0.84)	2.00 (1)
λ_{zD}	0.02 (-1)	0.10 (-0.67)	0.50 (1)
V_{DP}	0.40 (-1)	0.60 (0.00)	0.80 (1)
M	1.00 (-1)	5.00 (-0.67)	25.00 (1)
R_L	0.10 (-1)	6.00 (0.19)	10.00 (1)

Table 3.2: Range of the scaling group values (normalized values given in parenthesis) considered for velocity anisotropy estimation

β_0	0.2793	β_{24}	0.0015
β_1	-0.1393	β_{25}	-0.0036
β_2	0.044	β_{34}	-0.0005
β_3	0.1501	β_{35}	0.233
β_4	0.0677	β_{45}	0.0212
β_5	0.2058	β_{11}	0.1952
β_{12}	0.0176	β_{22}	-0.1248
β_{13}	-0.1124	β_{33}	0.0909
β_{14}	0.0099	β_{44}	-0.0267
β_{15}	-0.1342	β_{55}	-0.1017
β_{23}	-0.0248		

Table 3.3: Response surface coefficients for velocity anisotropy estimation. These coefficients should be implemented in equation (3.15) to estimate dimensionless velocity anisotropy.

Groups	**Low**	**Intermediate**	**High**
λ_{xD}	0.10 (-1)	0.25 (-0.84)	2.00 (1)
λ_{zD}	0.02 (-1)	0.10 (-0.67)	0.50 (1)
V_{DP}	0.40 (-1)	0.60 (0.00)	0.80 (1)
N_D	1.00 (-1)	3.30 (-0.49)	10.00 (1)
M	1.00 (-1)	5.00 (-0.67)	25.00 (1)
R_L	0.10 (-1)	6.00 (0.19)	10.00 (1)

Table 3.4: Range of the scaling group values (normalized values given in parenthesis) considered for dispersivity estimation.

β_0	0.2002 (0.1383)	β_{15}	-0.0049 (-0.0011)	β_{46}	-0.0066 (-0.0010)
β_1	0.0173 (0.0204)	β_{16}	0.0016 (-0.0015)	β_{56}	-0.0024 (-0.0001)
β_2	-0.0115 (-0.0149)	β_{23}	-0.0077 (-0.0117)	β_{11}	-0.0407 (-0.0117)
β_3	0.0426 (0.0337)	β_{24}	0.0047 (0.0025)	β_{22}	-0.0211 (-0.0129)
β_4	0.0214 (0.0056)	β_{25}	-0.0037 (-0.0027)	β_{33}	0.0010 (0.0048)
β_5	0.0174 (0.0117)	β_{26}	-0.0001 (-0.0010)	β_{44}	-0.0506 (-0.0346)
β_6	0.0029 (0.0004)	β_{34}	0.0097 (0.0011)	β_{55}	-0.0597 (-0.0360)
β_{12}	-0.0031 (-0.0014)	β_{35}	0.0017 (-0.0043)	β_{66}	-0.0180 (-0.0117)
β_{13}	0.0189 (0.0156)	β_{36}	-0.0033 (0.0019)		
β_{14}	0.0008 (0.0021)	β_{45}	0.0101 (-0.0023)		

Table 3.5: Response surface coefficients for dimensionless local dispersivity estimation at $x_D = 1$ (see Eq. (3.15)). The subscript number is based on the order in Table 3.4. Updated coefficients that include all 750 simulations are shown in parenthesis.

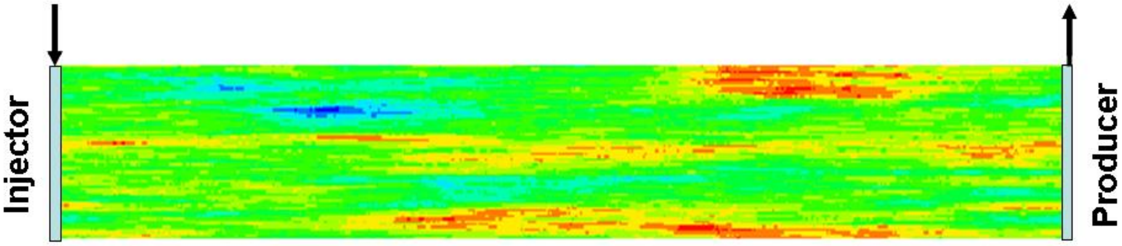

Figure 3.1: Schematic representation of the modeled reservoir

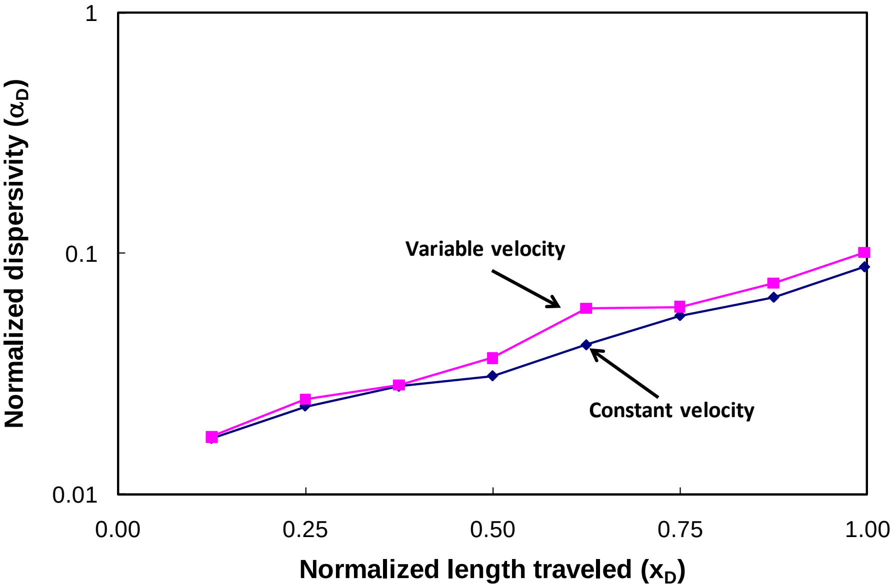

Figure 3.2: Effect of the local velocity on the estimated local dispersivity. The comparison shows that difference is not significant. Scaling groups are constant at $N_D = 3.33$, $R_L = 6.0$, $M = 5.0$, $V_{DP} = 0.60$, $\lambda_{xD} = 0.25$ and $\lambda_{zD} = 0.10$.

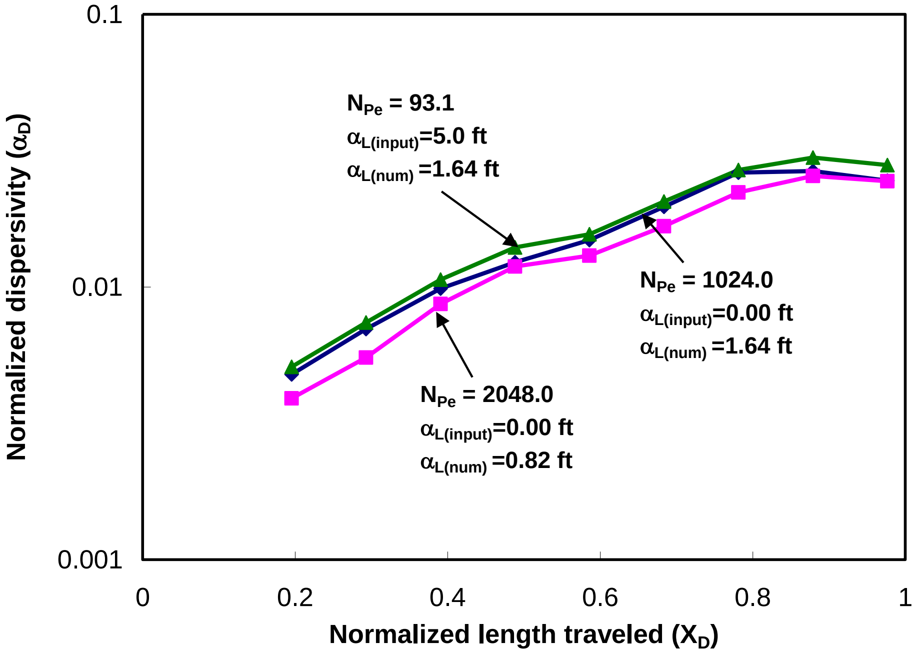

Figure 3.3: Effect of the Peclet number on local dispersivity estimated from simulation. The constant value of dispersivity in the Peclet number is subtracted from simulation results to obtain local dispersivities. Scaling groups are constant at $N_D = 2.52$, $R_L = 8.0$, $M = 1.0$, $V_{DP} = 0.60$, $\lambda_{XD} = 0.25$ and $\lambda_{ZD} = 0.08$.

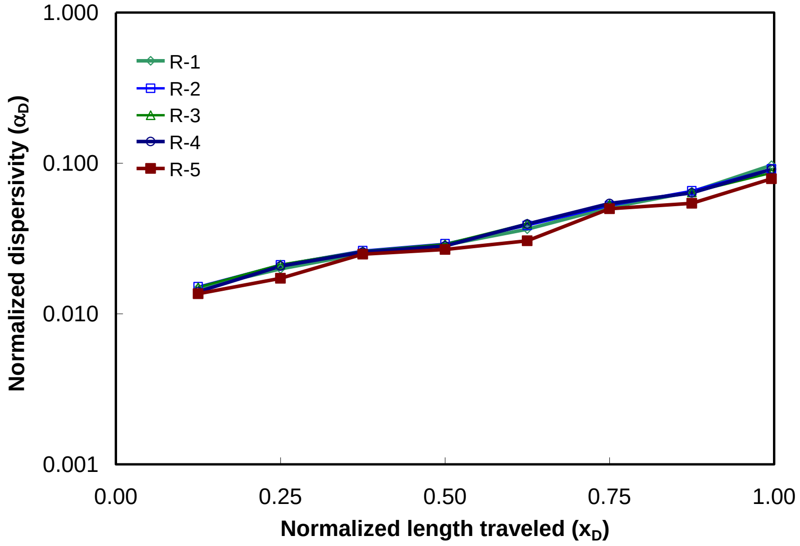

Figure 3.4: Example illustration of how the dispersivity values are nearly identical for the same values of the scaling groups. (see Table 3.1).

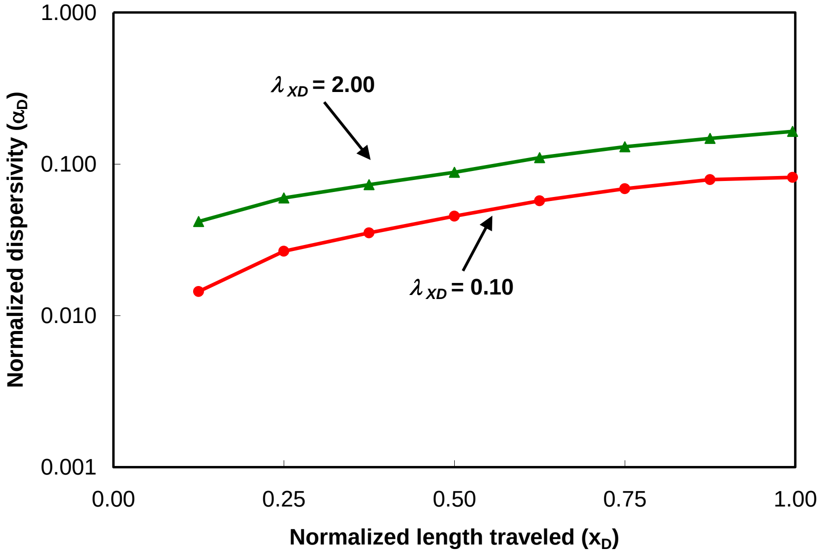

Figure 3.5: Effect of dimensionless correlation length in the longitudinal direction on the local dispersivity. All other scaling groups are held constant: $N_D = 3.30$, and $R_L = 0.10$, $M = 5.0$, $V_{DP} = 0.60$, and $\lambda_{ZD} = 0.10$.

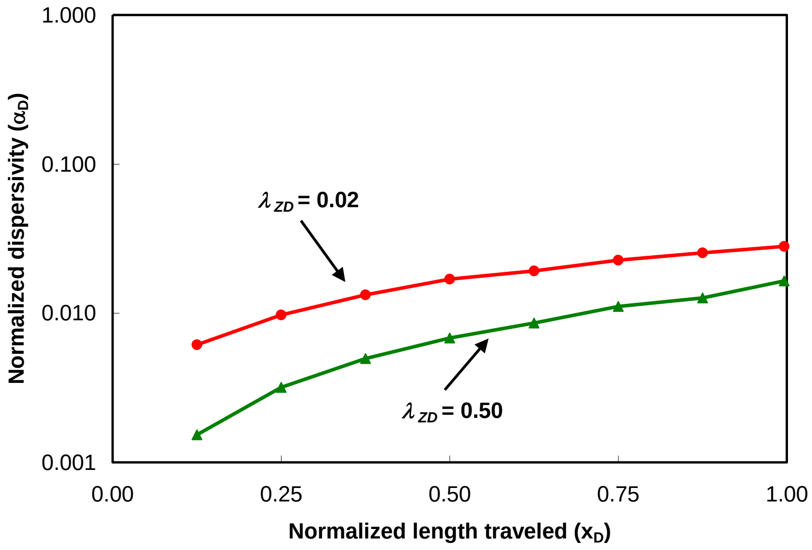

Figure 3.6: Effect of dimensionless correlation length in the transverse direction on the local dispersivity. All other scaling groups are held constant: $N_D = 3.30$, $R_L = 10.0$, $M = 1.0$, $V_{DP} = 0.60$, and $\lambda_{xD} = 0.25$.

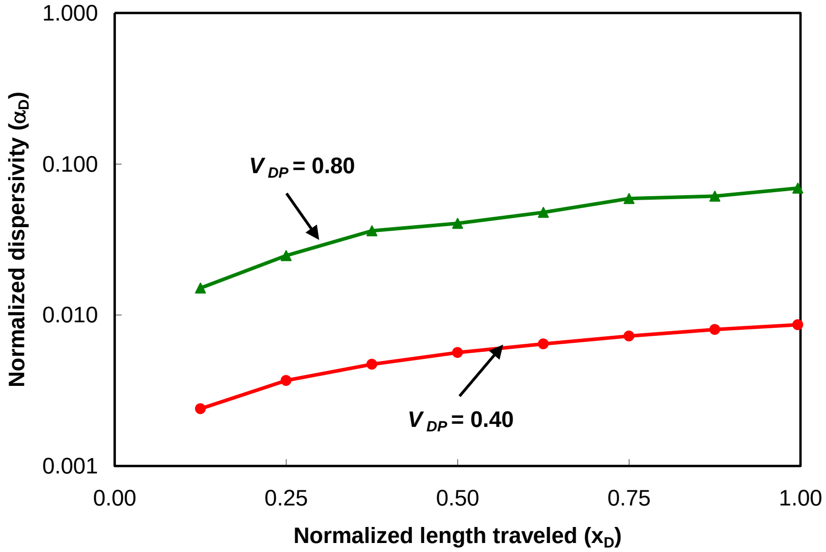

Figure 3.7: Effect of the Dykstra-Parsons coefficient on the local dispersivity. All other scaling groups are held constant: $N_D = 3.30$, $R_L = 6.0$, $M = 1.0$, $\lambda_{xD} = 0.25$, and $\lambda_{zD} = 0.02$.

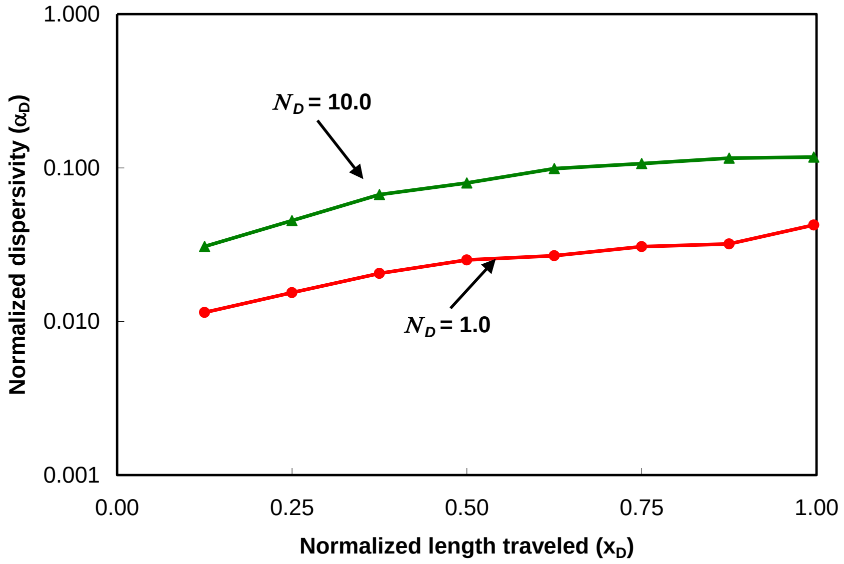

Figure 3.8: Effect of the dispersion number on the local dispersivity. All other scaling groups are held constant: $R_L = 6.0$, $M = 25.0$, $V_{DP} = 0.60$, $\lambda_{XD} = 0.25$, and $\lambda_{ZD} = 0.10$.

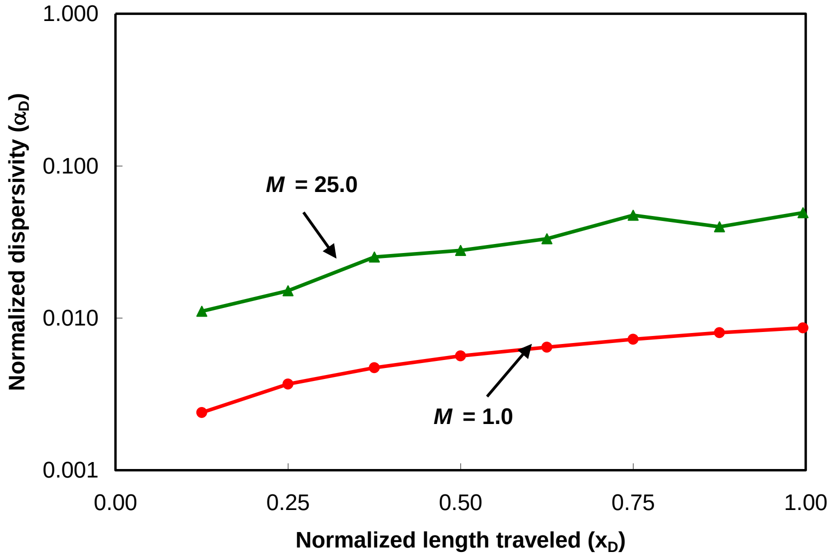

Figure 3.9: Effect of the mobility ratio on the local dispersivity. All other scaling groups are held constant: $N_D = 3.30$, $R_L = 6.0$, $V_{DP} = 0.40$, $\lambda_{XD} = 0.25$, and $\lambda_{ZD} = 0.02$.

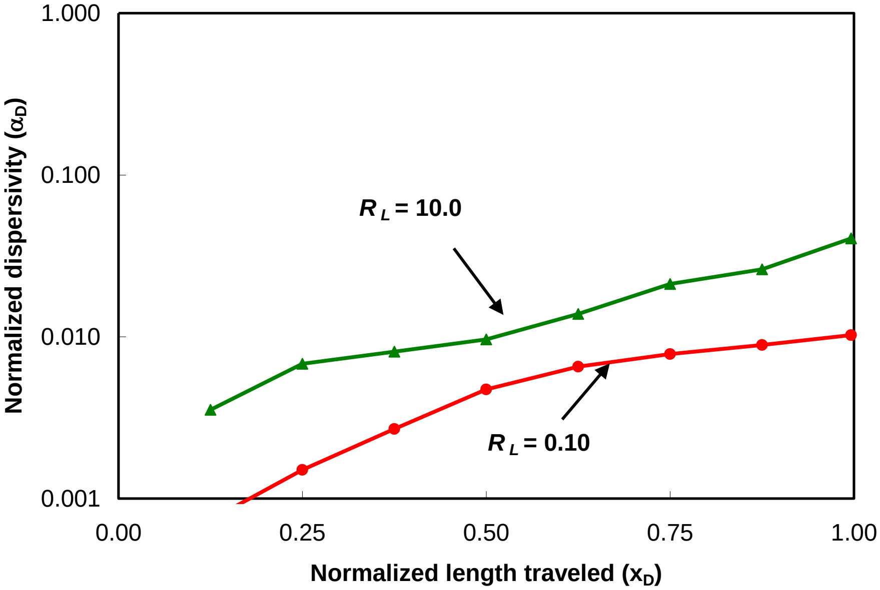

Figure 3.10: Effect of the aspect ratio on the local dispersivity. All other scaling groups are held constant: $N_D = 3.30$, $M = 5.0$, $V_{DP} = 0.40$, $\lambda_{xD} = 0.10$, and $\lambda_{zD} = 0.10$.

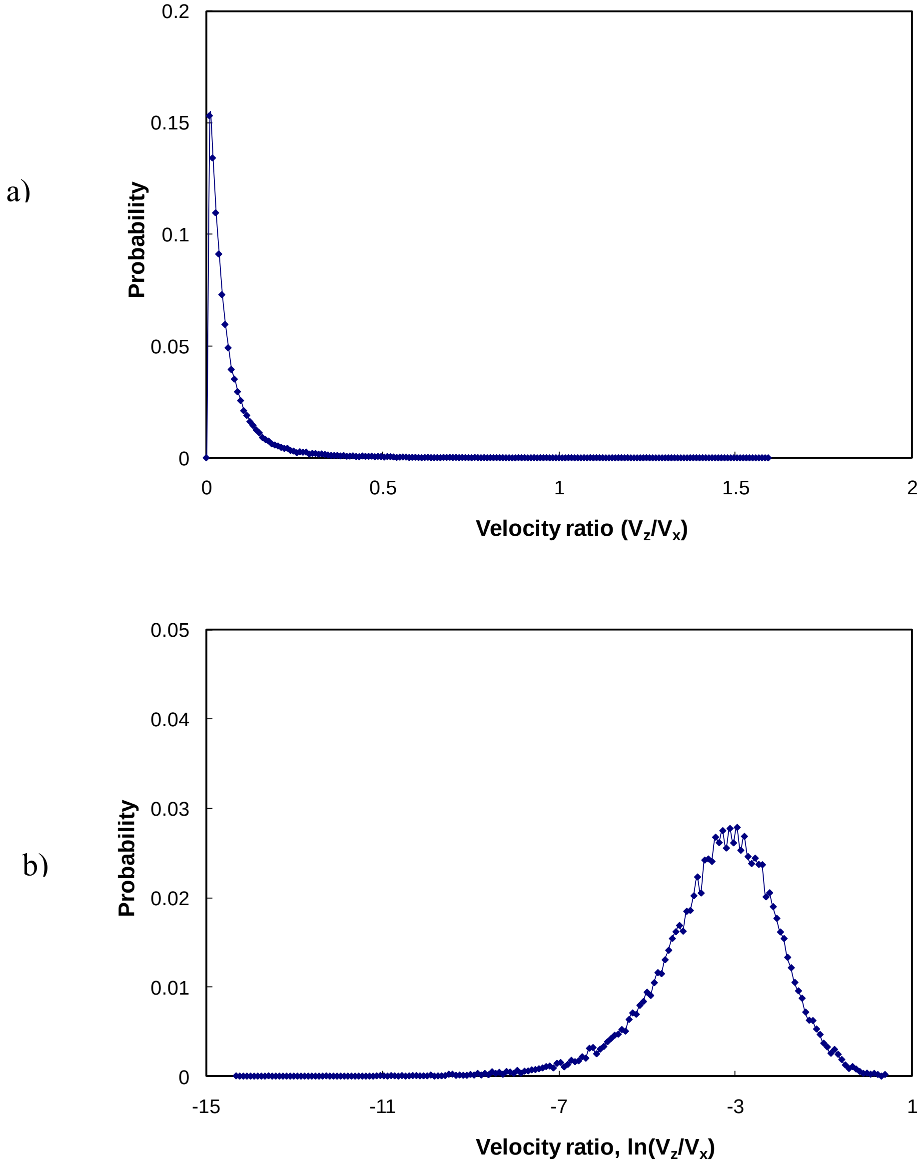

Figure 3.11: Probability distribution function of the velocity anisotropy ratios. a) Normal distribution, b) log-normal distribution. The figure shows that the velocity anisotropy ratios are log-normally distributed; therefore, mean of its log-normal distribution is used from each simulation.

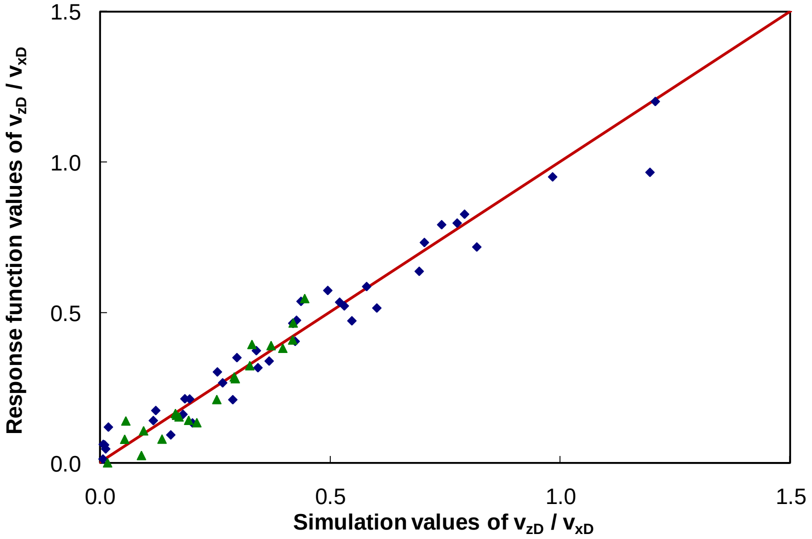

Figure 3.12: Comparison of predicted dimensionless velocity anisotropy ratios using the response function coefficients given in Table 3.3, and those calculated from 330 simulations. Green (triangle) points are the test data and blue (diamond) points are original experimental design results.

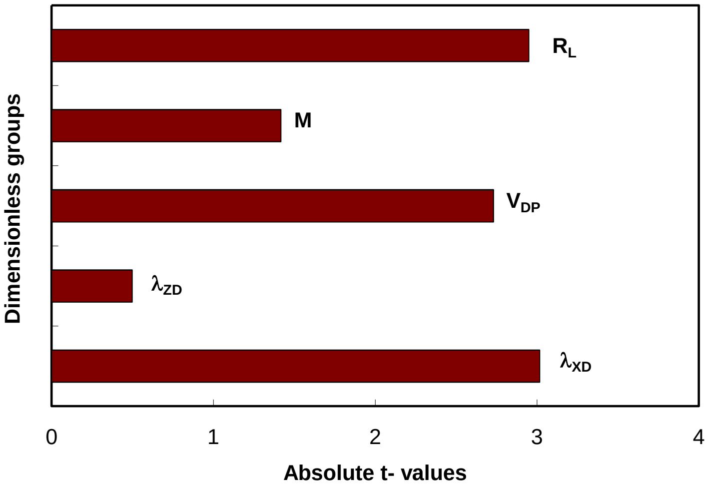

Figure 3.13: Pareto plot showing the significance of each scaling group in the estimation of dimensionless velocity anisotropy. The aspect ratio, longitudinal correlation length, and Dykstra-Parsons coefficients are the three most important groups.

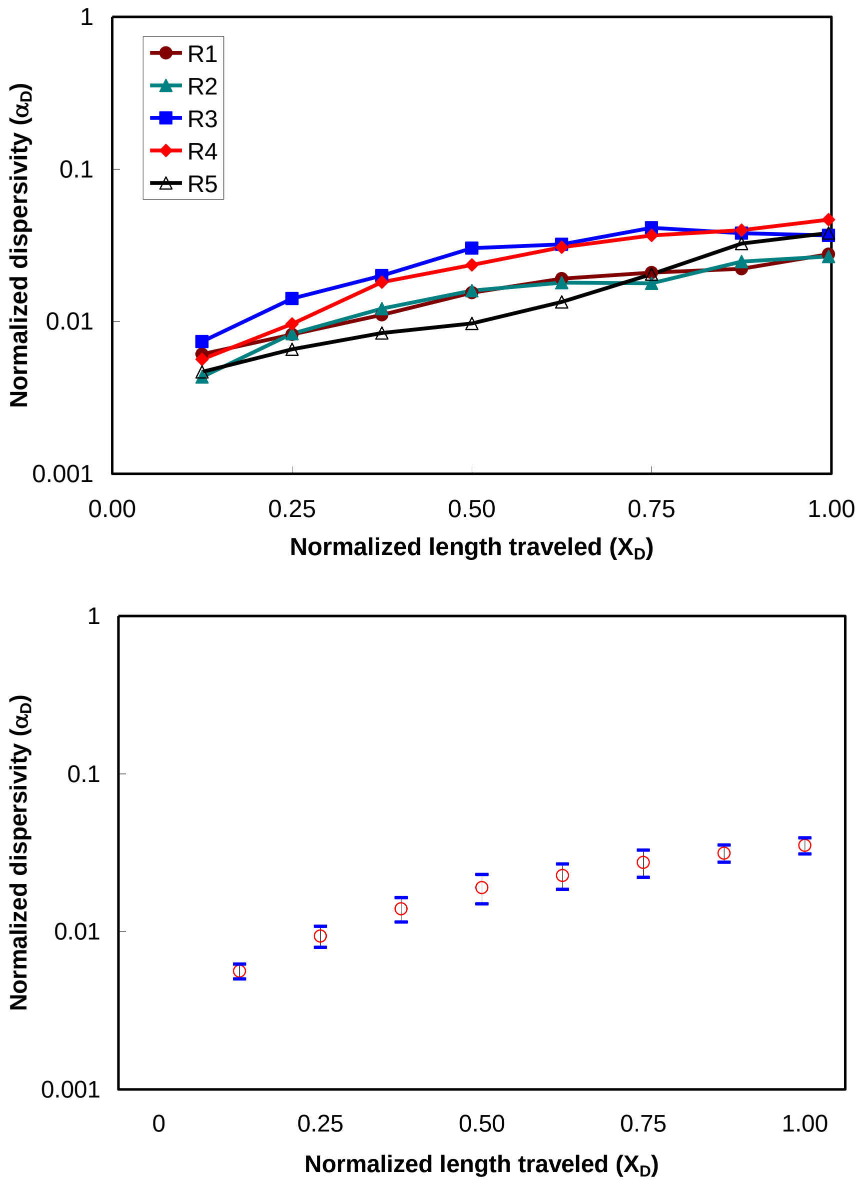

Figure 3.14: Illustration of the averaged dispersivity from five realizations. a) Estimated dispersivity from simulation using five different realizations of permeability distribution. Scaling group values are fixed and are: $N_D = 3.30$, $M = 1.0$, $V_{DP} = 0.80$, $\lambda_{xD} = 0.25$, , $R_L = 6.0$ and $\lambda_{zD} = 0.50$. b) Averaged dispersivity from five realizations and its one standard deviation limit.

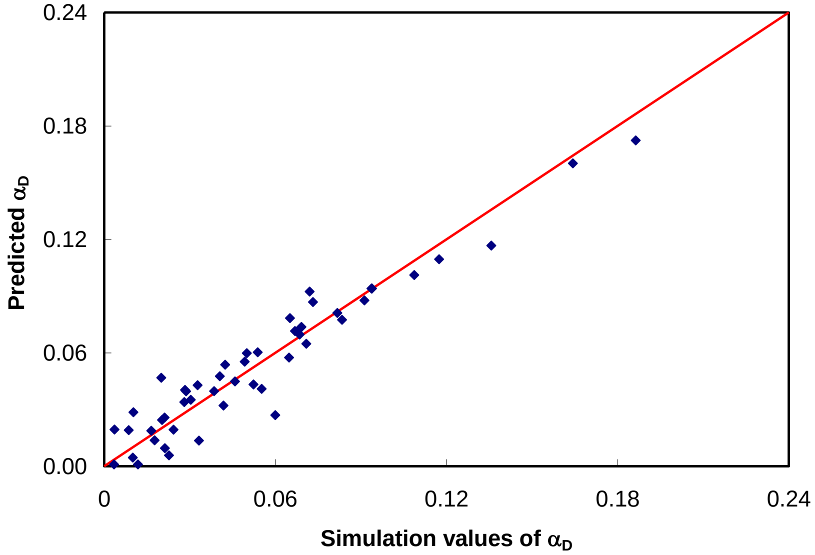

Figure 3.15: Comparison of predicted dimensionless local dispersivities at x_D =1.0 using the response function coefficients given in Table 3.5, and those calculated from 54 simulations (270 total since five different realizations were averaged for each experiment).

a)

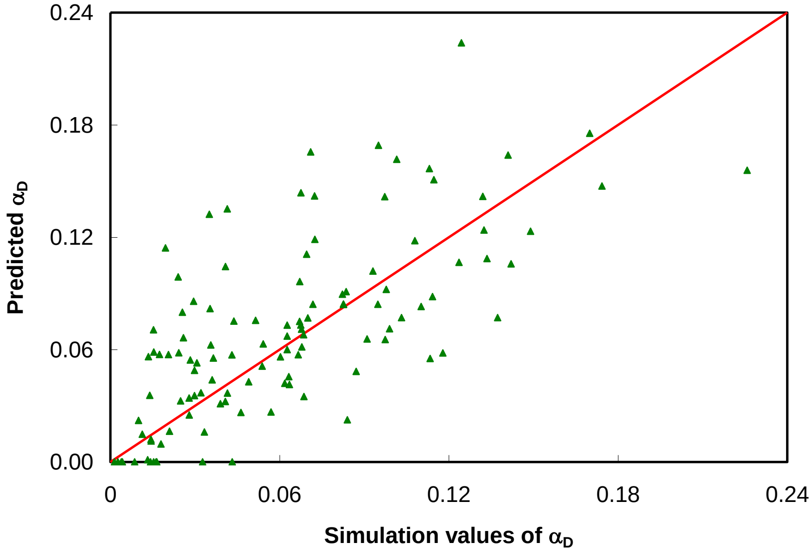

b)

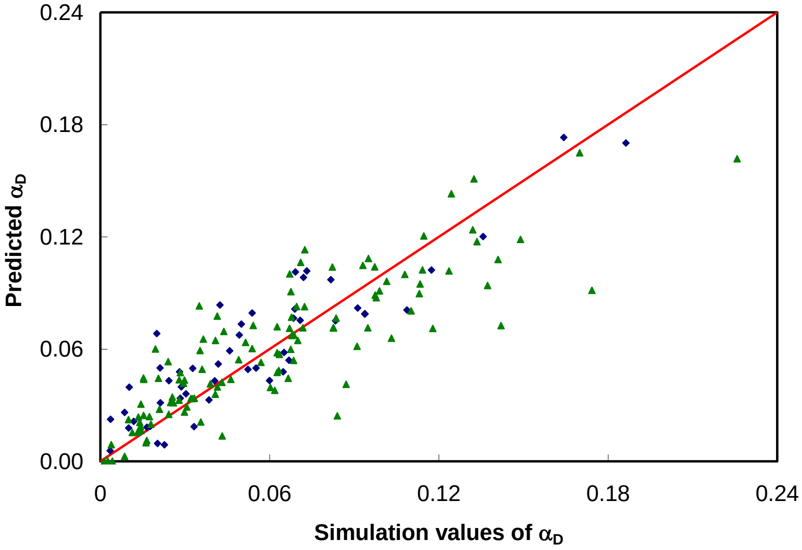

Figure 3.16: Comparison of predicted dimensionless local dispersivities at x_D =1.0 to simulated values using a) test simulations and the response function using the original coefficients given in Table 3.5, and b) those from all 750 simulations and the response function using the updated coefficients (given in parenthesis in Table 3.5) . Green (triangle) points are the test data and blue (diamond) points are original experimental design results.

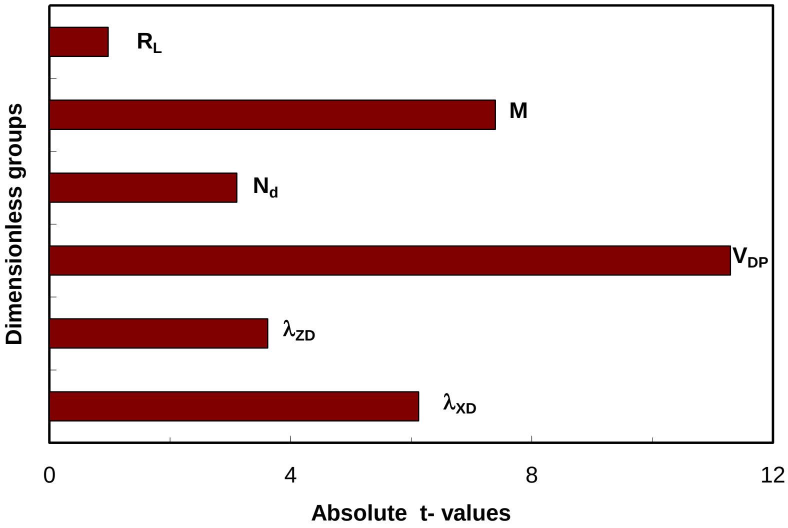

Figure 3.17: Pareto plot showing the significance of each scaling group in the estimation of dimensionless local dispersivities at x_D =1.0. The dispersion number, mobility ratio, longitudinal correlation length, and Dykstra-Parsons coefficients are the four most important groups.

Chapter 4: Upscaling Miscible Floods Considering Reservoir Mixing

In this chapter we show through simulations of both first contact miscible (FCM) and multi-contact miscible (MCM) floods that grid-block size can be significantly increased if reservoir mixing is large. Thus, heterogeneous reservoirs that have large longitudinal correlation lengths can be upscaled using larger grid-blocks than reservoirs with random permeability fields. To properly upscale miscible floods, the sum of numerical dispersion and physical dispersion associated with the reservoir heterogeneities, geometry and fluid properties must be equal at both the fine and large-scales. This chapter shows how to determine a priori the maximum grid-block size allowed in both the x- and z-directions to predict accurately the oil recovery from miscible gas floods.

4.1 OVERVIEW

A common way to convert geological models into simulation models is to upscale permeabilities based on reservoir heterogeneity, while the importance of reservoir mixing in upscaling is ignored. Dispersion is often approximated by numerical dispersion associated with the grid-block size used in numerical simulation. The origin of numerical dispersion in finite-difference schemes is related to the truncation error in the spatial and temporal derivatives of the transport equations (Price *et al.*, 1968; Lantz 1971; Peaceman, 1977). Fanchi (1983) derived expressions for multi-dimensional numerical dispersion for single-phase flow using the three-dimensional convection-dispersion equation (see Appendix C).

Large grid-block sizes are typically used in simulation to minimize computational time. This can result in significant error in recoveries owing to over mixing of gas with oil (Stalkup 1998; Haajizadeh *et al.* 1999, 2000; Solano *et al.* 2001; Johns *et al.* 2002; Moulds *et al.* 2005). Numerical dispersion should match or not exceed the level of dispersion at the field scale, but the level of mixing at the field scale is not typically known.

Geological models have been upscaled from very fine-scale to the reservoir simulation scale with little attention to reservoir mixing. There are numerous methods to upscale permeability and other petrophysical parameters (Durlofsky 1991, 1992; Durlofsky *et al.* 1997, King *et al.* 1998; Darman *et al.* 2001; Wallstrom *et al.* 2002; Chen *et al.* 2003, 2006, 2008; Wen *et al.* 2003, 2006). As permeability is upscaled, however, reservoirs are made more homogeneous, which results in smaller dispersivities. Thus, the level of mixing and permeability upscaling are coupled. Hui *et al.* (2005) developed a method for upscaling miscible processes. The method compromises effective flux boundary conditions to suppress the flux through high-permeability streaks and the extended Todd-Longstaff with upscaled relative permeabilities formulation to account for immobile oil that is not available for miscible flow. Jerauld (1998) demonstrates a procedure for scale-up of MCM gas injection. The procedure involves developing pseudo relative permeability curves including gas trapping and mixing parameter (ω) for matching the response of the miscible process. However in both studies the importance of physical and numerical dispersion is not considered.

The impact of upscaling on the spreading of solute transport in saturated porous media has been investigated by several authors (Kitanidis 1990; Dagan 1994; Rubin *et al.* 1999, 2003; Khaleed *et al.* 2002). Kitanidis (1990) developed a method to estimate effective hydraulic conductivity of a medium with locally variable conductivity. Dagan (1994) addressed the smoothing of the velocity field in upscaling and suggested a computational method to compensate for this loss. In all of these papers, however, the level of mixing at the fine scale is not matched at the large scale.

In this chapter we give a procedure to upscale miscible floods considering the appropriate level of reservoir mixing based on the response functions generated in the previous chapter. We first demonstrate the approach for a FCM displacement, and then show that the procedure also works well for a MCM displacement in the same reservoir. We also show what happens to the predicted oil recoveries if mixing is not considered in the upscaling process.

4.2 UPSCALING METHOD

The goal of permeability upscaling is to find a homogeneous effective permeability that has the same flow characteristics as the fine scale. The numerical procedure for computing the equivalent grid-block permeability (effective permeability) is described for a steady state, incompressible, single-phase flow. The flow equation is given by the continuity equation and Darcy's law:

$$\nabla \cdot (\mathbf{u}) = 0 \tag{4.1}$$

$$\boldsymbol{u} = -\frac{\boldsymbol{k}}{\mu} \cdot \nabla P \tag{4.2}$$

where $\boldsymbol{u}$ is the local fluid velocity vector, P is the local pressure, μ is the fluid viscosity and $\boldsymbol{k}$ is the local permeability tensor. The pressure equation is therefore given by substitution of Darcy's law (Eq.(4.2)) into the continuity equation (Eq.(4.1)) as given by,

$$\nabla \cdot \left(\mathbf{k}(\mathrm{x}, \mathrm{z}) \cdot \nabla P \right) = 0 \tag{4.3}$$

The grid-blocks to be upscaled are localized by assuming flow occurs in one-direction, and that transverse boundaries are no flow. The effluent flux from the upscaled solution is matched to the fine scale solution by varying the permeability (see Fig. 4.1).

As upscaling proceeds, however, the permeability variation in the reservoir is made more homogeneous, changing the Dykstra-Parsons coefficient and correlation lengths. The dispersion number is also affected by the increase in the grid-block sizes in both the longitudinal and transverse directions (Garmeh and Johns, 2009). Thus, the values of key scaling groups are altered, changing the level of mixing in the reservoir. The level of mixing as a result of upscaling is typically smaller compared to the fine scale model.

The decreased level of mixing associated with the "scaling groups" is fortuitous since the level of numerical dispersion is increased during upscaling. Thus, we can potentially achieve the same level of mixing as the original fine-scale model.

Too much upscaling, however, can result in over mixing. Our goal in upscaling therefore is to find the maximum grid-block size that we can use to match the level of mixing at the fine and coarse scales. We propose here the simple formula that the maximum grid-block size allowed in the longitudinal direction during upscaling is obtained when

$$\alpha_{L_{tot}}\Big|_{Fine} = \alpha_{L_{tot}}\Big|_{Upscaled} \tag{4.4}$$

where the total longitudinal mixing is given by the sum of the numerical dispersion and dispersion associated with the scaling groups referred to here as the reservoir dispersivity ($\alpha_{L_{res}}$). That is,

$$\alpha_{L_{tot}} = \alpha_{L_{num}} + \alpha_{L_{res}} \,. \tag{4.5}$$

A similar equation as Eq. (4.4) can be written for the transverse dispersivity. Because our goal is to find the maximum grid-block size, we do not input any physical dispersivity into Eq. (4.5). The reservoir dispersivity ($\alpha_{L_{res}}$) is determined from the evaluation of the response function for the scaling group values at the fine and coarse models. Values of $\alpha_{L_{res}}$ can change significantly during upscaling as is shown in the example below.

4.3 IMPORTANCE OF RESERVOIR MIXING IN UPSCALING MISCIBLE FLOODS

In this section, we examine the importance of reservoir mixing in upscaling miscible floods. This section first gives an example of flow upscaling for two reservoirs that have different reservoir mixing. We then show that reservoir mixing has significant influence on the size of the upscaled grid-block to accurately model miscible displacement.

We consider two reservoirs with nearly the same scaling group values including the Dykstra-Parsons coefficient, but with different permeability correlation lengths. The mean permeability and *lnk* standard deviation for both reservoirs are 1700 md and 1.0 respectively. The longitudinal and transverse correlation lengths for reservoir 1 are 125.0 ft and 5.0 ft respectively, and 1.0 ft in both directions for reservoir 2. Thus, the permeabilities for reservoir 2 are uncorrelated, while reservoir 1 has some continuous layers. The fine scale simulation models of both reservoirs contain 512 grid-blocks in the longitudinal direction by 64 grid-blocks in the transverse direction, and the grid-block sizes are initially 1 ft in the x- and z-directions. Figure 4.2 shows the stochastically generated permeability distributions and their upscaled models with 32x32 grid-blocks for each reservoir.

4.3.1 FCM Displacement

The calculated total longitudinal dispersivity is 29.9 ft from the response function for the fine grid model for reservoir 1 and 1.4 ft for reservoir 2. The scaling groups for the reservoir 1 are $\lambda_{XD} = 0.24$, $\lambda_{ZD} = 0.08$, $V_{DP} = 0.65$, $N_D = 2.91$, $M = 1.0$, and $R_L = 8.0$. The dimensionless velocity ratio used to calculate the dispersion number is estimated from the other scaling groups to be $v_{zD} / v_{xD} = 1.061$ so that $v_z / v_x = 0.133$. The larger level of mixing for the FCM displacement in reservoir 1 allow it to be accurately upscaled to larger grid-blocks than for reservoir 2. For the upscaled 32x32 model, the total longitudinal dispersivity for reservoir 1 is about 23.3 ft (8 ft of which is due to numerical dispersion and 15.3 ft from the response function), but about 8.5 ft for reservoir 2. Thus, reservoir 1 could be upscaled even further in the longitudinal direction while mixing in reservoir 2 greatly exceeds its fine grid counterpart (8.5 ft compared to 1.4 ft).

Figure 4.3 shows the solvent concentrations for both reservoirs and their upscaled models at 0.7 PVI. The concentrations show that the upscaled model for reservoir 1 more accurately reflects the displacement for its fine scale model, while the front for reservoir 2 is unphysical (large spread out). The front for the upscaled model of reservoir 2 will breakthrough earlier than its fine grid counterpart. Figure 4.4 shows that recoveries for reservoir 1 in the upscaled model is accurately predicted, but not for reservoir 2.

4.3.2 MCM Displacement

Most gas floods are multicontact miscible (MCM), where mixing causes some two-phase flow. This example demonstrates that the derived scaling groups for FCM flow can also be used with good accuracy for MCM gas floods. MCM floods can be modeled this way largely because relative permeability affects are minimal, and there is good mass transfer between phases.

We use the same reservoirs as in the previous example, but we consider the gas displacement of 12-component oil characterized by Solano *et al.* (2001). We also use an irreducible water saturation of 0.32 in the simulations so that the maximum possible gas saturation is 0.68. Tables 4.1 and 4.2 give the oil and gas compositions and the fluid and reservoir properties used. The minimum enrichment for miscibility (MME) is a blend of about 53% solvent with lean gas. We used an injection gas enrichment of 65% solvent so that the displacement is clearly MCM. A 1.4 hydrocarbon pore volume (HCPV) of enriched gas is injected continuously.

Figure 4.5 shows the gas saturation distribution at 0.4 HCPVI for the fine and upscaled models. As shown, the gas saturations are more accurately modeled for reservoir 1 for the same reasons as described before. Early breakthrough of injected gas occurs for reservoir 2 owing to its unphysical and large level of mixing. Figure 4.6 gives the oil recoveries for each reservoir. Oil recovery curves indicate that using larger grid-block sizes that induces greater mixing than reservoir mixing at the field scale decreases the accuracy of the predicted oil recovery because over mixing drive the composition routes deeper into the two-phase region and reduces the local displacement efficiency.

4.4 SIMULTANEOUS UPSCALING IN BOTH X- AND Z-DIRECTIONS

We now illustrate how to determine the appropriate grid-block sizes in both the x- and z- directions simultaneously. We consider a permeability distribution for reservoir 3 shown in Figure 4.7 with the following heterogeneity properties: mean permeability of 200 md, $V_{DP} = 0.60$, $\lambda_X = 200$ ft, $\lambda_Z = 10$ ft. The length of reservoir 3 in the longitudinal direction is 800 ft, while the length in the transverse direction is 100 ft. The fine-scale model has 512 by 64 grid-blocks, so that each grid-block is 1.56 ft in both directions.

The scaling groups for the fine grid model are $\lambda_{XD} = 0.25$, $\lambda_{ZD} = 0.10$, $V_{DP} = 0.60$, $N_D = 2.28$, $M = 1.0$, and $R_L = 6.0$. The dimensionless velocity ratio used to calculate the dispersion number is estimated from the other scaling groups to be $v_{zD} / v_{xD} = 0.649$ so that $v_z / v_x = 0.081$. The dimensionless local longitudinal dispersivity estimated form the response function using these group values is *0.045* so that the longitudinal dispersivity based on the longitudinal length is about 36 ft. The numerical dispersivity for a grid-block size of 1.56 ft is 0.78 ft ($\approx \Delta x/2$), giving a total dispersivity for the fine-grid model of 36.78 ft. Thus, an upscaled model from the fine grid one should result in a total longitudinal dispersivity of about 36.78 ft to match its fine-grid equivalent in the longitudinal direction.

To upscale the model accurately in both directions, the total longitudinal and transverse dispersivities of the upscaled model should be equal to its fine grid values. We start with transverse dispersion equation (given in Appendix C) to estimate the amount of transverse dispersion, where we do not input any longitudinal or transverse dispersivity in fine-scale model so that the grid-block sizes can be maximized in the upscaled model. We further assume negligible diffusion, small time-step sizes, and $|v| \approx v_x \approx v_{inj}$ to obtain,

$$D_{zz} \approx \left[\alpha_L \left(\frac{v_z}{v_x} \right)^2 + \alpha_T + \frac{1}{2} \Delta z \left(\frac{v_z}{v_x} \right) \right] v_{inj} = \alpha_{T_{tot}} v_{inj} . \qquad (4.6)$$

Equation (4.6) shows that upscaling in the transverse direction is coupled to upscaling in the longitudinal direction. In Eq.(4.6), α_L is equal to the total longitudinal dispersivity ($\alpha_{L_{tot}}$). The velocity ratio is again determined from its separate response function.

The procedure to predict the maximum grid-block sizes in both directions is as follows:

1) Determine the total longitudinal and transverse dispersivities in the original fine-scale model based on the scaling groups and initial geological discretization.

2) Fix the number of grid-blocks in the transverse direction and decrease the number of grid-blocks in the longitudinal direction until the total dispersivity in the longitudinal direction exceeds that of the fine-grid model. The number of grid-blocks in the transverse direction should initially be large. For each case calculate the total dispersivity in the transverse and longitudinal directions. Select the best upscaled model that matches both dispersivities at the fine scale.

3) Repeat step 2 using a smaller number of grid-blocks in the transverse direction until the optimal number of grid-blocks in both directions is found.

Table 4.3 shows the values of all scaling groups and dispersivities as the number of grid-blocks in the longitudinal direction for reservoir 3 are decreased. The number of grid-blocks in the transverse direction is fixed at 32 in this example, half of the original 64. As is shown in Figure 4.8, the x-direction correlation lengths do not change significantly because the grid-block sizes never exceeds the x-direction correlation lengths used to generate the permeabilities and it increases slightly in z-direction as grid-block size exceeds the z-direction correlation length (see Fig. 4.9). The Dykstra-Parsons coefficient changes only slightly from 0.60 to 0.56, but this induces a more significant change in the velocity ratio. The result of changes in grid-block size and velocity ratio causes the dispersion number to decrease significantly as the model is upscaled. The dimensionless longitudinal dispersivity from the response function ($\alpha_{L_{tot}}$) therefore also decreases as the number of grid-blocks in the longitudinal direction decrease. The ratio of the transverse to longitudinal dispersivity is about 0.01 for the cases studied. The sum of the numerical dispersivity and the dispersivity estimated from the response function does not show a monotonic trend, initially decreasing from the original fine-grid model, and then increasing with larger grid-blocks (see values in Table 4.3). The best matches to the fine-grid total dispersivities are the 32x32 and 16x32 grids, although one could find an optimum in between.

Figure 4.10 gives the recovery curves for each grid considered in Table 4.3. As shown, they all do reasonably well, except for the 8x32 grid system. This one does exceptionally poor because its level of mixing in both directions is very large compared to the fine-grid model. In general, one would select the model with the fewest number of grid-blocks that results in good accuracy, in this case the 16x32 grid. For that grid, the grid-block size in the longitudinal direction is 50 ft.

Table 4.4 shows the scaling group values and dispersivities where the number of grid-blocks in the longitudinal direction are fixed, but we vary the number of grid-blocks in the transverse direction. The best choices in this case are the 32x32 and 32x16 grids as more refined grids give larger total transverse dispersivities than the fine grid. The recovery curves in Figure 4.11 verify that the 32x16 grid is a good choice as it minimizes the total number of grid-blocks. The recovery curves for eight grid-blocks or less in the transverse direction do not show the characteristic S-shape for the fine grid model and should not be selected.

Maximum grid-block size for reservoir 3 is between 25-50 ft in longitudinal and 3.12-6.25 ft in transverse direction, however, our fine-scale model can only be divided by 2, 4, 8, 16; therefore the closet reservoir dimensions to the fine-scale model are 32x32 or 16x32. Figure 4.12 shows the fine-scale and upscaled models (32x32) solvent concentration profile (FCM) and gas saturation profile (MCM) after 0.4 HPVI. Gas saturation profile in the reservoir indicates that oil saturation distribution after MCM displacement (oil left behind) can be predicted by the procedure developed for FCM displacement if we do not over mix the reservoir.

Figure 4.13 and 4.14 shows the longitudinal and transverse reservoir mixing contour map of the upscaled models of the reservoir 3; however, the size of the fine-scale model has been reduced to 480x60 for better discretization in upscaling process. It can be observed that the sum of the numerical dispersivity and the dispersivity estimated from the response function does not show a monotonic trend, initially decreasing from the original fine-grid model, and then increasing with larger grid-blocks. The combined contour map for reservoir mixing from both directions determines the region that has the appropriate level of mixing (see Fig. 4.15).

4.5 SUMMARY AND CONCLUSIONS

From the response function developed for estimating reservoir dispersivity, we showed how to determine simultaneously the maximum grid-block sizes in both the longitudinal and transverse directions that should be used in compositional simulation to maintain the proper level of mixing between the fine and upscaled models. We demonstrated through examples that the total dispersivity, which includes reservoir and numerical dispersivity, must be approximately equal at the fine and coarse scales. Oil recoveries and the location of unswept oil can be accurately predicted if this balance is preserved. We also concluded that small grid-blocks must be used for reservoirs with uncorrelated permeabilities, while larger grid blocks can be used for more layered reservoirs. The predicted level of mixing for first-contact miscible floods can be extended with good accuracy to multicontact miscible (MCM) gas floods.

Component	Reservoir Oil	Lean Gas	Solvent	MI 65%
CO_2	0.015	0.0815	0.2120	0.1663
C_1	0.5069	0.8305	0.2770	0.4707
C_2	0.0587	0.062	0.2050	0.1550
C_3	0.0358	0.0225	0.2560	0.1743
C_4	0.0192	0.0035	0.0500	0.0337
C_5	0.0161			
C_6-C_7	0.0379			
C_8-C_{10}	0.0725			
C_{11}-C_{14}	0.0639			
C_{15}-C_{19}	0.0614			
C_{20}-C_{29}	0.0639			
C_{30+}	0.0487			

Table 4.1: Oil and gas compositions used in the MCM displacement example.

Reservoir pressure	4500 psi
Oil viscosity	1.17 cp
Gas viscosity	0.047 cp
Water viscosity	0.34 cp
Oil density	46.92 lb/ft^3
Gas density	16.5 lb/ft^3
Water density	62.4 lb/ft^3
K_{rog}	0.63
K_{rg}	0.52
K_{rw}	0.73
Solvent enrichment	65%
MME	53%

Table 4.2: Fluid and reservoir properties for the MCM displacement example.

No. of Grids	λ_{xD}	λ_{zD}	V_{DP}	N_D	α_{LDres}	Δx	Δz	v_Z/v_X	$\alpha_{L_{tot}}$	$\alpha_{T_{tot}}$
512x64	0.25	0.10	0.60	2.28	0.045	1.56	1.56	0.081	36.83	0.306
64x32	0.25	0.10	0.59	1.11	0.027	12.50	3.12	0.077	28.02	0.289
32x32	0.25	0.10	0.59	0.79	0.022	25.00	3.12	0.077	29.97	0.301
16x32	0.25	0.10	0.58	0.54	0.016	50.00	3.12	0.074	37.83	0.323
8x32	0.25	0.10	0.56	0.37	0.010	100.00	3.12	0.068	57.85	0.372

Table 4.3: Iterations of total dispersivities during upscaling of reservoir 3, where the grid-block size in the x-direction is varied. The values of mobility and aspect ratios are always constant at 1.0 and 6.0, respectively. The shaded region shows possible grids that match dispersivities well.

No. of Grids	λ_{xD}	λ_{zD}	V_{DP}	N_D	α_{LDres}	Δx	Δz	v_Z/v_X	$\alpha_{L_{tot}}$	$\alpha_{T_{tot}}$
512x64	0.25	0.10	0.60	2.28	0.045	1.56	1.56	0.081	36.83	0.306
32x64	0.25	0.10	0.60	0.56	0.019	25.00	1.56	0.079	27.48	0.235
32x32	0.25	0.10	0.59	0.79	0.022	25.00	3.12	0.077	29.97	0.301
32x16	0.25	0.10	0.57	1.06	0.023	25.00	6.25	0.071	31.17	0.378
32x8	0.25	0.13	0.52	1.40	0.022	25.00	12.50	0.061	30.04	0.496
32x4	0.25	0.25	0.48	2.10	0.027	25.00	25.00	0.069	34.23	1.021
32x2	0.25	0.50	0.35	3.52	0.021	25.00	50.00	0.097	29.10	2.688

Table 4.4: Iterations of total dispersivities during upscaling of reservoir 3, where the grid-block size in the z-direction is varied. The values of mobility and aspect ratios are always constant at 1.0 and 6.0, respectively. The shaded region shows possible grids that match dispersivities well.

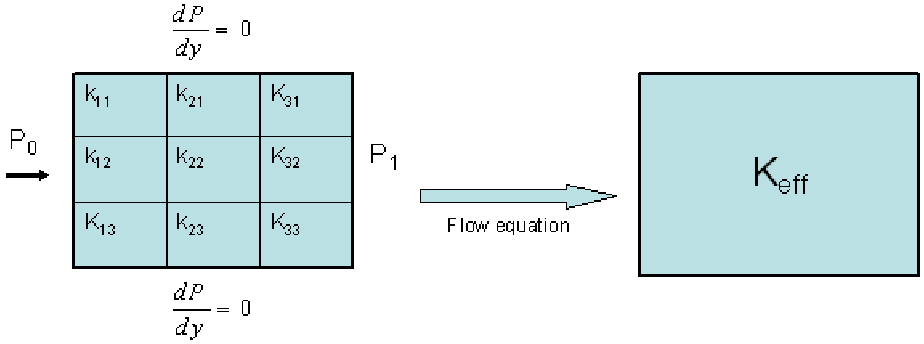

Figure 4.1: Schematic representation of local flow upscaling scheme. Upscaling represents a heterogeneous porous medium by its equivalent homogeneous one.

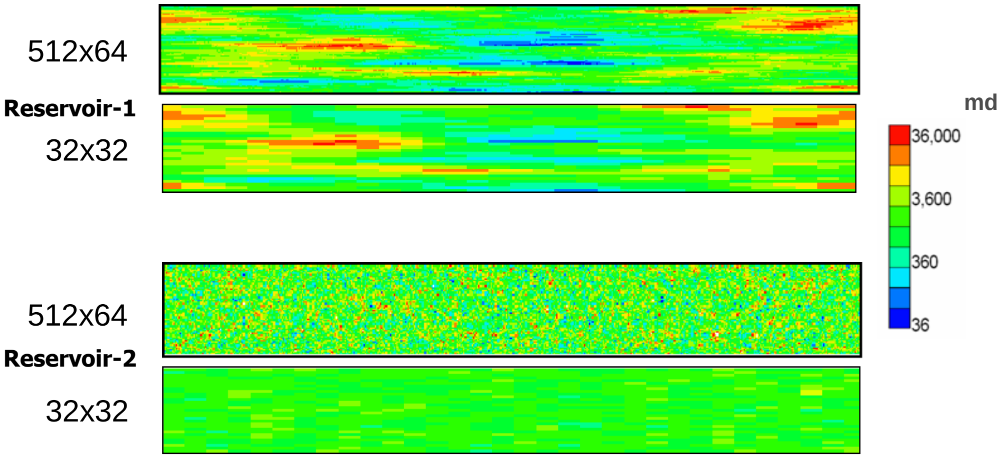

Figure 4.2: Permeability distributions for the fine- and upscaled models. Permeabilities for reservoir 2 are uncorrelated.

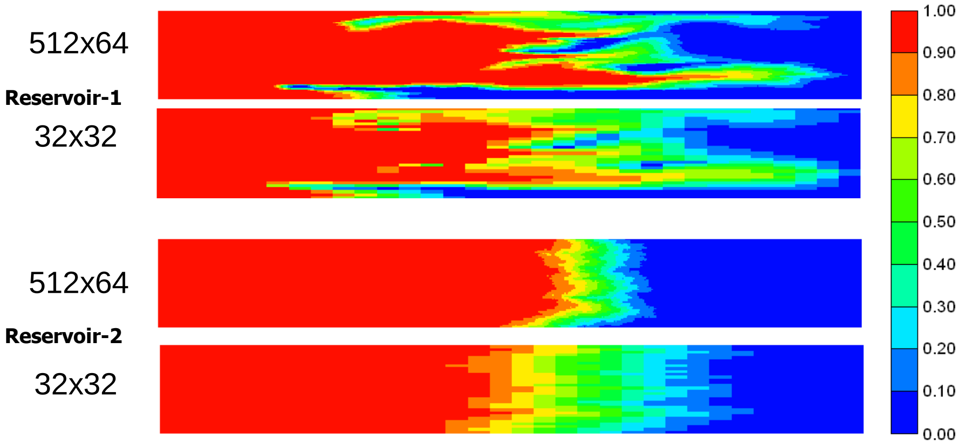

Figure 4.3: Solvent concentrations for reservoirs 1 and 2 for fine and upscaled models at 0.7 PVI. Concentration profiles show that reservoir 1 can be upscaled to 32x32, but not reservoir 2.

a)

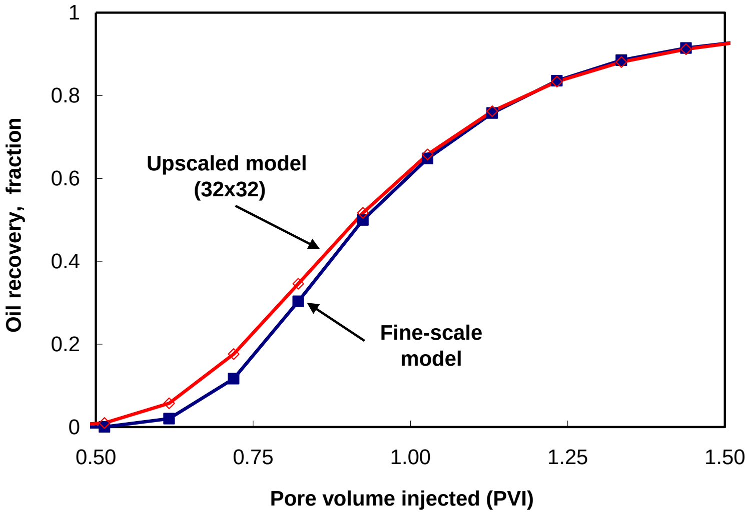

b)

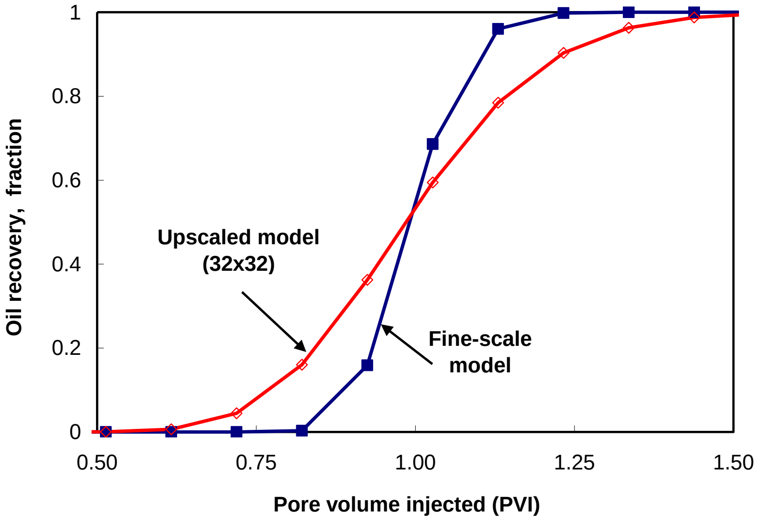

Figure 4.4: Comparison of FCM oil recoveries for fine and upscaled models for a) reservoir 1, and b) reservoir 2. Oil recoveries for reservoir 2 in the upscaled model are not accurate owing to over mixing by numerical dispersion.

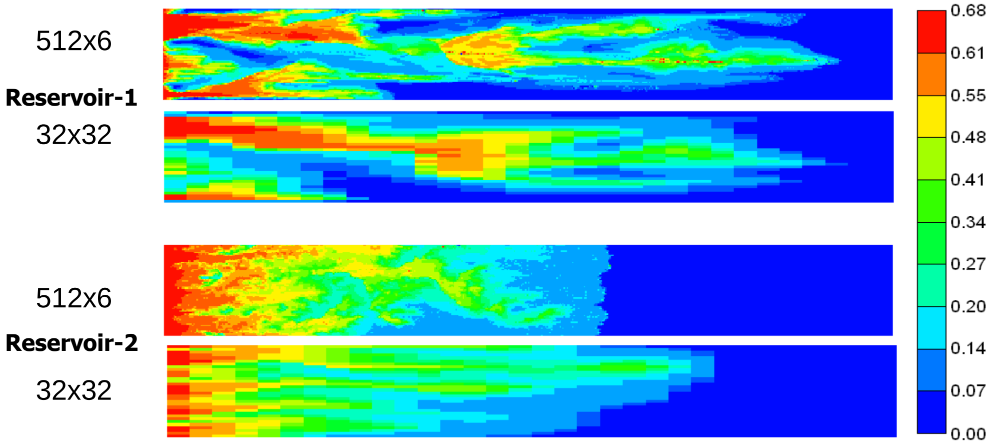

Figure 4.5: Comparison of gas saturation profiles at 0.4 HCPVI for reservoirs 1 and 2, and their upscaled models. The upscaled results for reservoir 1 are more accurate than for reservoir 2.

a)

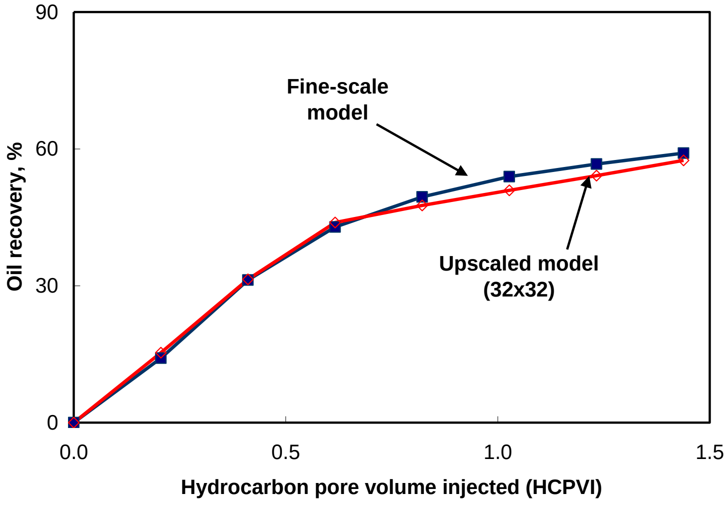

b)

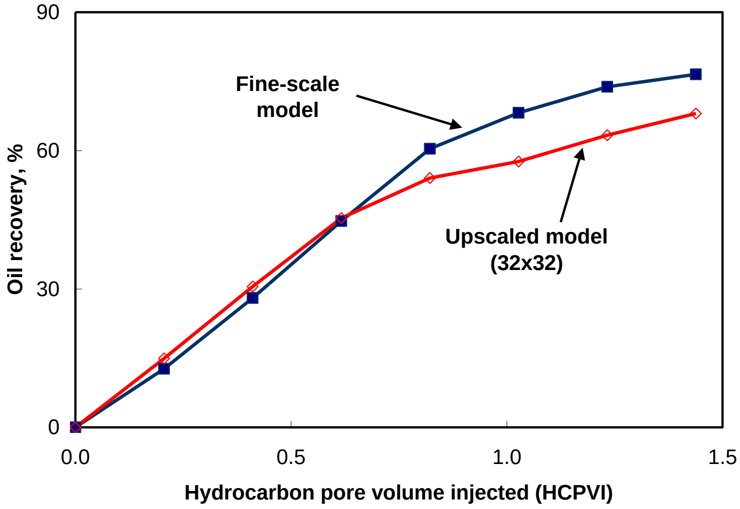

Figure 4.6: Comparison of predicted oil recoveries from the MCM displacements for the fine and upscaled models for a) reservoir 1 and b) reservoir 2. Over mixing induced by large grid-block sizes in reservoir 2 results in early breakthrough of gas.

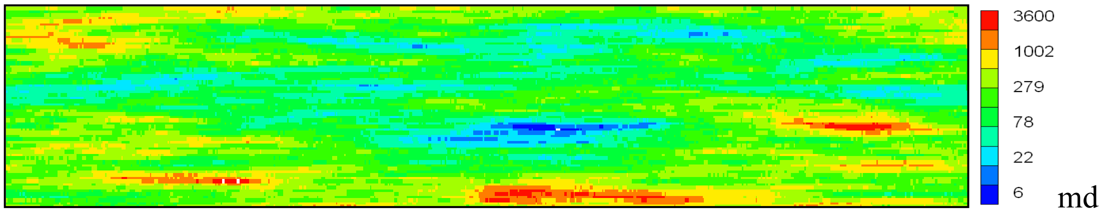

Figure 4.7: Permeability distribution for reservoir 3.

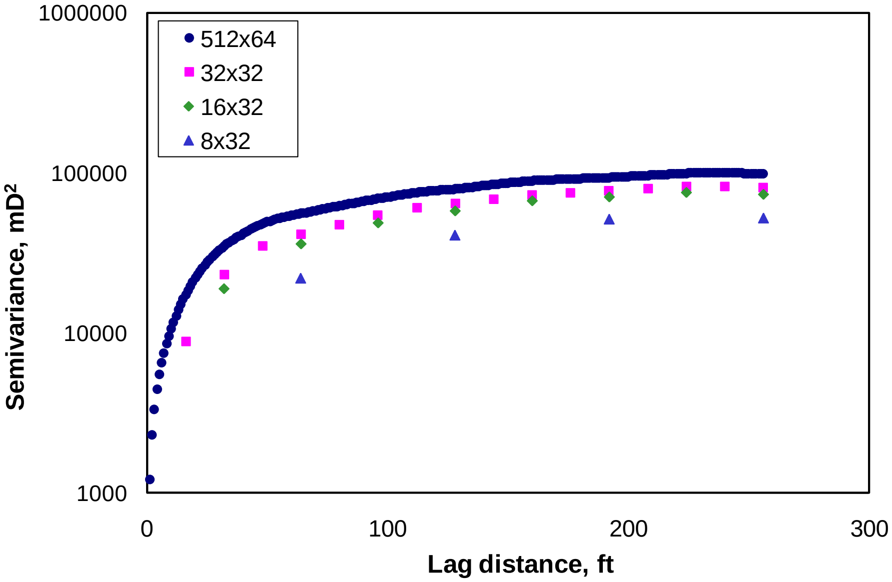

Figure 4.8: Semivariance of the permeability field in the x-direction for reservoir 3 and its various upscaled grid-block size in x-direction.

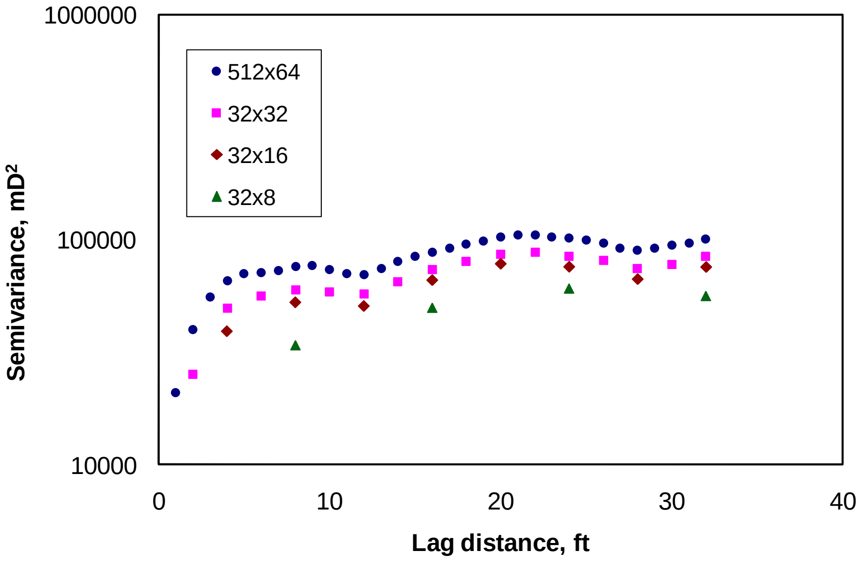

Figure 4.9: Semivariance of the permeability field in the z-direction for reservoir 3 and its various upscaled grid-block size in z-direction.

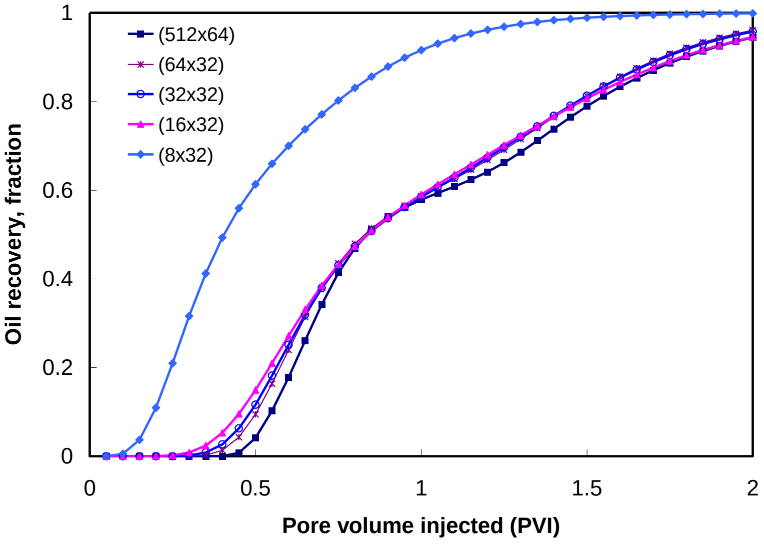

Figure 4.10: Comparison of oil recoveries for various upscaled models in the longitudinal direction to the original fine-grid model (see Table 4.3).

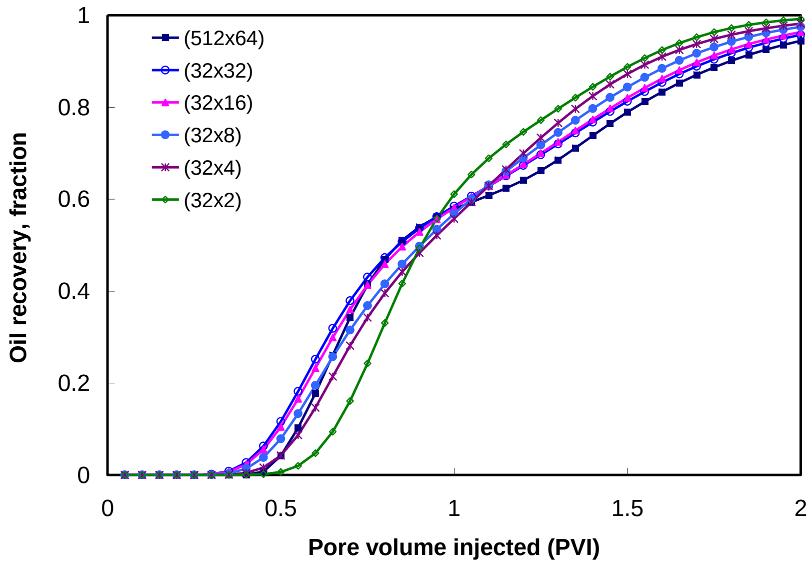

Figure 4.11: Comparison of oil recoveries for various upscaled models in the transverse direction to the original fine-grid model (see Table 4.4).

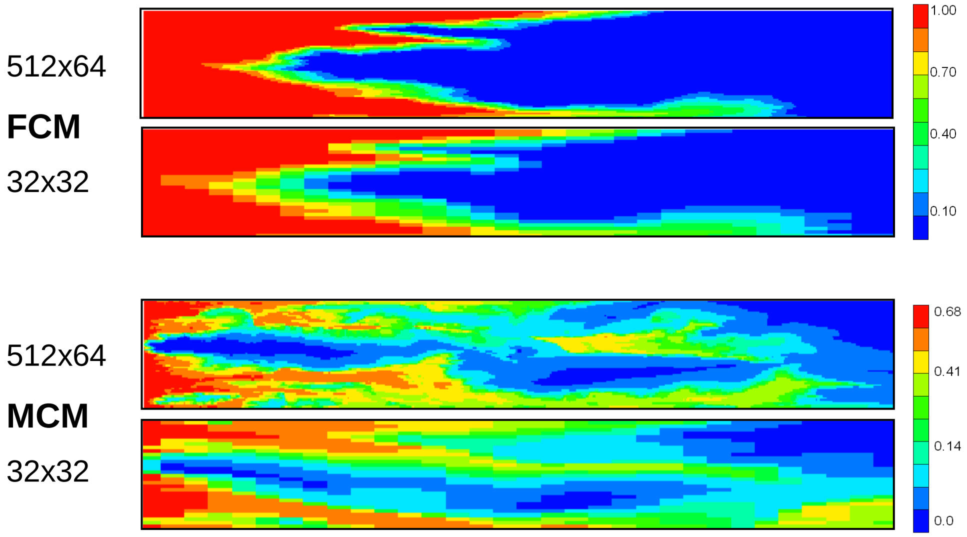

Figure 4.12: Comparison of solvent concentrations (or saturations for MCM case) at 0.4 HCPVI for reservoir 3, and their upscaled models. The upscaled grid-block sizes are 25.0 ft by 3.12 ft.

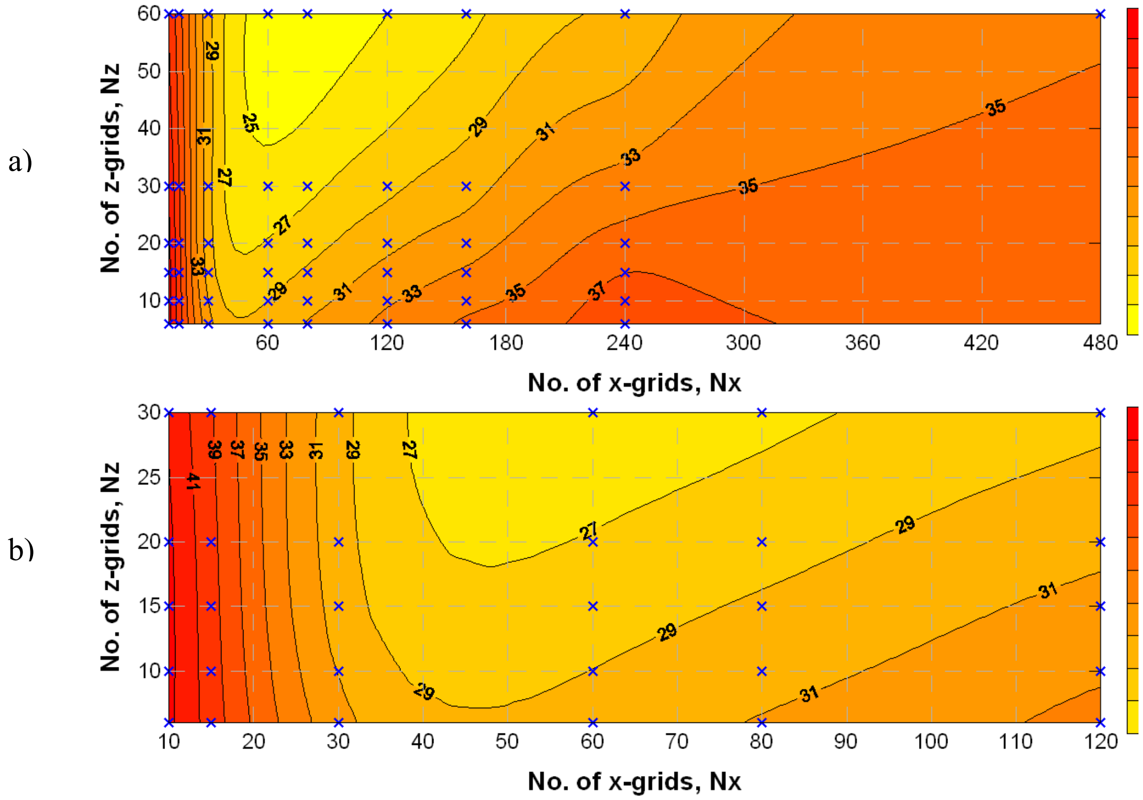

Figure 4.13: Contour map of the effective longitudinal reservoir mixing and upscaled grid block size (a), and zoom in the upscaled zone (b). Effective reservoir mixing does not increase monotonically by increased grid bock size. The fine-scale longitudinal dispersivity is 35 ft for 480 x 60 grid-blocks.

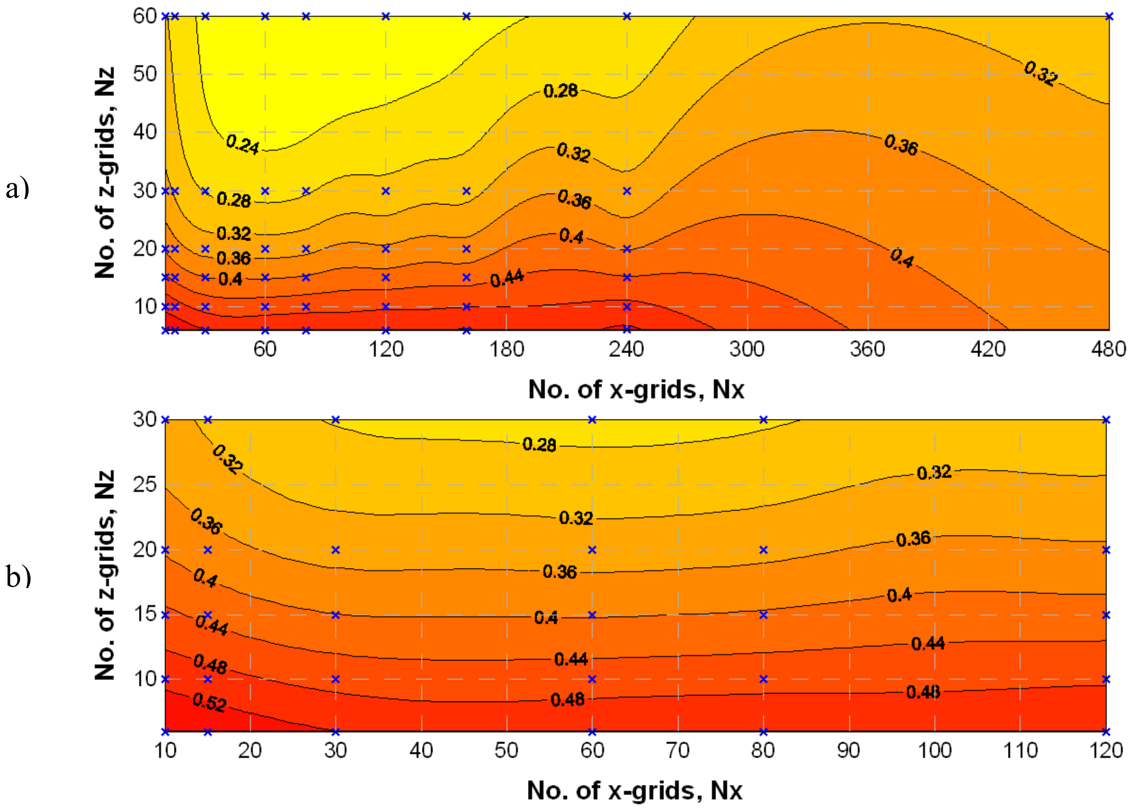

Figure 4.14: Contour map of the effective transverse reservoir mixing and upscaled grid block size (a), and zoom in the upscaled zone (b). Effective transverse reservoir mixing increase monotonically by increased grid bock size in z-direction. The fine-scale transverse dispersivity is 0.30 ft for 480 x 60 grid-blocks.

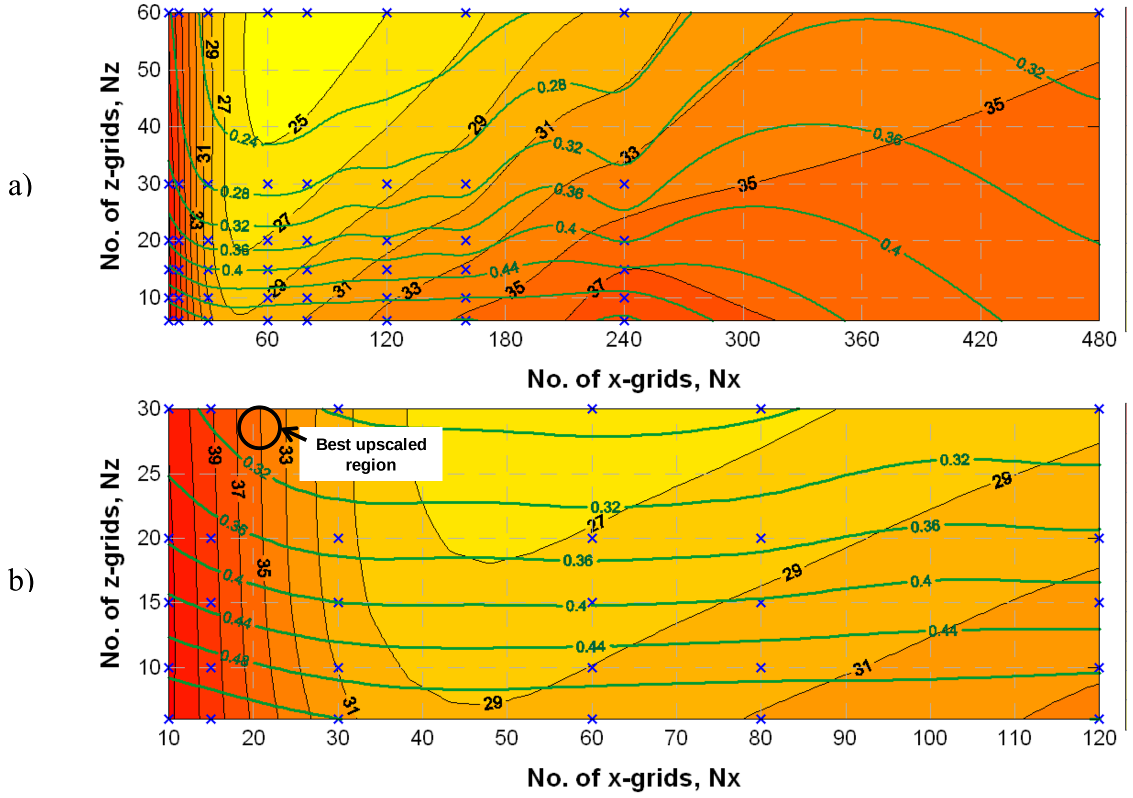

Figure 4.15: Contour map of the effective longitudinal and transverse reservoir mixing and upscaled grid block size (a), and zoom in the upscaled zone (b). The fine-scale longitudinal and transverse dispersivities are 35 ft and 0.3 ft respectively. The best upscaled region is shown in the figure.

Chapter 5: Summary, Conclusions and Recommendations

5.1 SUMMARY AND CONCLUSIONS

Oil recovery from miscible gas floods is highly dependent on the magnitude of mixing at the pattern scale. Mixing of gas and oil decreases the strength of the injected fluid, and causes early breakthrough. Mixing causes multicontact (MCM) floods to develop two-phase flow and more mixing drives the composition route deeper into the two-phase region, reducing the local displacement efficiency. The level of mixing that occurs in a reservoir, however, is widely debated and often ignored in reservoir simulation where very large grid blocks are used. Large grid blocks create artificially large mixing that can cause errors in predicted oil recovery.

The main objectives of this dissertation were to:

1. Understand the origin of scale dependent dispersivity (reservoir mixing) from pore-scale to laboratory-scale and finally field-scale.
2. Determine dispersivity as function of reservoir parameters and stochastic heterogeneity of the reservoir.
3. Determine appropriate grid-block sizes that should be used in compositional simulations to accurately predict oil recovery from miscible displacements.

For this purpose, we investigated a variety of pore-scale models to find the origin of scale dependency and to demonstrate that dispersion is scale-dependent. From our pore-scale study we found that diffusion is the primary reason for reservoir mixing or dispersion. Diffusion can be significantly enhanced if the surface area of contact between the reservoir and injected fluid are increased as fluids propagate through the reservoir. We found that both echo and transmission dispersivities are scale dependent. They may or may not reach an asymptotic limit depending on the heterogeneities encountered. The scale dependence results from an increase in the contact area between solute (gas) and resident fluid (oil) as heterogeneities are encountered, either at the pore scale or pattern scale. Convective spreading is not mixing, but can enhance mixing by allowing the impact of diffusion to be magnified.

We then derived dimensionless groups from an inspectional analysis for a first contact miscible (FCM) gas flood in a 2-D heterogeneous reservoir. Over 800 2-D numerical simulations were carried out using experimental design to obtain a response function for dispersivity as a function of the scaling groups. Dispersivity is estimated from the response function based on travelled distance and other reservoir and fluid parameters that go into the scaling groups. Reservoir mixing can be enhanced as fluids propagate through reservoir heterogeneities. The most important groups that affect mixing are the mobility ratio, dispersion number, and heterogeneity parameters, such as horizontal and vertical correlation lengths and the variation of medium’s permeability.

The degree to which dispersion increases with distance traveled depends on the dispersion number. Large dispersion numbers can yield large dispersivities away from the injection well. Mixing is increased as reservoir heterogeneity and the longitudinal correlation length increase. Mixing is decreased as the dispersion number and aspect ratio decrease. There is no scale dependence of dispersion with distance traveled when the dispersion number is zero. Mixing is increased for larger mobility ratios owing to increased channeling of injected gas through the reservoir.

Last, we showed that to properly upscale miscible floods, the sum of numerical dispersion and physical dispersion associated with the reservoir heterogeneities, geometry and fluid properties must be equal at both the fine and large-scales. We showed how to determine a priori the maximum grid-block size allowed in both the x- and z-directions to predict accurately the oil recovery from miscible gas floods. We also concluded that smaller grid-blocks must be used for reservoirs with more random permeabilities, while larger grid blocks can be used for more layered reservoirs. The predicted level of mixing for first-contact miscible floods can be extended with good accuracy to multicontact miscible (MCM) gas floods.

5.2 RECOMMENDATIONS AND FUTURE WORKS

In this section we present recommendations that can be considered to better model dispersion in permeable media and its impact on miscible displacements.

Even though comprehensive inspectional analysis was performed to find the key scaling groups that impact dispersion in miscible displacement, we ignored gravity, reaction and adsorption terms in our inspectional analysis; therefore, derived scaling groups can be extended to achieve more comprehensive results.

In our upscaling method, the upscaled permeability from incompressible and single-phase flow was linked to reservoir mixing. Single-phase and incompressible model assumptions can be extended to multi-phase flow models by updating capillary pressure and relative permeabilities. This extension can help to capture flow characteristics in partially miscible or immiscible displacements, where relative permeabilities play a significant role compared to reservoir mixing.

In the upscaling procedure, grid-block sizes, porosities and oil saturations (for MCM case) are assumed uniform spatially. Inspectional analysis and the upscaling procedure can be extended to account for spatially variable properties.

In heterogeneous reservoirs, dispersion influences miscible displacement by decreasing local displacement efficiency and increasing macroscopic sweep efficiency. Therefore, the impact of dispersion on oil recovery is complicated. Investigation of the impact of dispersion on oil recovery in heterogeneous reservoirs can be extended to find conditions where dispersion may decrease or increase oil recovery in a reservoir.

Various displacements of oil by gas give different sensitivities of oil recovery to dispersion. The impact of dispersion on different oil/gas pairs, which have different drive mechanisms, can be investigated.

The reliability of field echo tests (SWTTs) can be affected by fluid drift caused by neighboring wells or boundary conditions. Therefore, the impact of flow drift on the scale dependency of echo and local dispersivities should be investigated.

Reservoir mixing is enhanced by any mechanism that increases the surface area of contact between fluids. Reservoir mixing is enhanced by viscous and dispersive crossflow as shown by the dispersion number. This can be extended by investigating the impact of gravity and capillary crossflow on enhanced reservoir mixing.

Appendix A: Analytical Two-Dimensional CD Solution

The following two-dimensional convection-dispersion equation is used to model both transverse and longitudinal dispersion coefficients in the pore-scale displacements.

$$D_l \frac{\partial^2 C}{\partial x^2} + D_t \frac{\partial^2 C}{\partial y^2} - v\frac{\partial C}{\partial x} = \frac{\partial C}{\partial t} \quad . \tag{A.1}$$

The above equation assumes a continuum porous media and that the mean pore velocity in the vertical (y-direction) is zero, while the mean velocity in the horizontal (x-direction) is constant (see Fig. A.1). The initial and boundary conditions for the CD equation in an infinite porous media are

$$\begin{aligned} &C(0,y,t) = C_O \qquad -a \le y \le a \\ &C(0,y,t) = 0 \qquad \text{all other values of y} \\ &\lim_{y\to\pm\infty} \frac{\partial C}{\partial y} = 0 \\ &\lim_{x\to\infty} \frac{\partial C}{\partial x} = 0 \quad . \end{aligned}$$

We assumed that the upper boundary of our pore-scale model was not felt during the displacement. This is confirmed from the concentrations at that boundary.

The analytical solution to the above model is given (Cleary and Ungs 1978) as

$$C(x,y,t)=\frac{C_O\,x}{4(\pi D_L)^{1/2}}\exp\left(\frac{vx}{2D_L}\right)\int_0^t \exp\left[-\frac{v^2}{4D_L}\tau-\frac{x^2}{4D_L\tau}\right]\tau^{-3/2} \\ \left[erf\left(\frac{a-y}{2(D_T\tau)^{1/2}}\right)+erf\left(\frac{a+y}{2(D_T\tau)^{1/2}}\right)\right]d\tau \quad . \tag{A.2}$$

where C_O is the injection concentration, D_L and D_T are the longitudinal and transverse dispersion coefficients, v is the injection velocity, t is the final time and a is the half of the vertical injection thickness (Fig. A.1).

We used only half of the medium in the y-direction of our porous media because of symmetry.

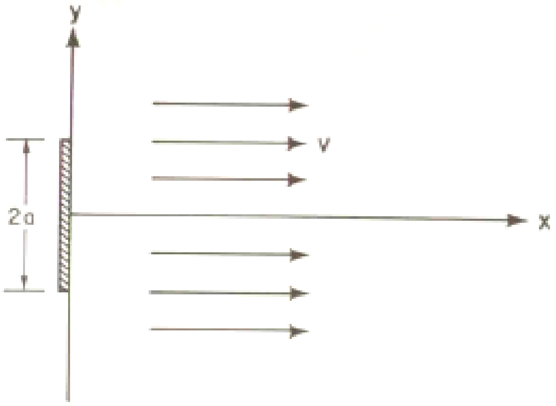

Figure A.1: Injection of solute over a distance $2a$ in two-dimensional porous media with a constant velocity v (from Javandel *et al.*, 1984). This boundary condition is used with the 2-D CD equation.

Appendix B: Scaling Groups by Inspectional Analysis

In this appendix, the dimensionless scaling groups for first-contact miscible (FCM) displacement are derived through use of inspectional analysis (Shook *et al.* 1992, Gharbi *et al.* 1998). We consider FCM displacement of incompressible fluids in a 2-D porous medium with no chemical reaction and adsorption. Governing equations for this process are conservation equations, Darcy's equation, continuity equation, a simple viscosity mixing rule equation, dispersion equation and two simple auxiliary equations.

$$\frac{\partial}{\partial t}\phi\sum_{j=1}^{n_p}\sum_{i=1}^{n_c}x_{ij}\rho_j S_j+\nabla\cdot\sum_{j=1}^{n_p}\sum_{i=1}^{n_c}x_{ij}\rho_j\vec{u}_j-\nabla\cdot\phi\sum_{j=1}^{n_p}\sum_{i=1}^{n_c}\vec{\vec{D}}_{ij}\cdot\nabla\rho_j x_{ij}=0 \qquad \text{(B.1)}$$

$$i=1,\ldots,n_c,\; j=1,\ldots,n_p$$

$$\nabla\cdot\vec{u}_j=0 \qquad \text{(B.2)}$$

$$\vec{u}_j=-\frac{kk_{rj}}{\mu_j}\left(\nabla P_j+\rho_j\vec{g}\right) \qquad j=1,\ldots,n_p \qquad \text{(B.3)}$$

$$\mu_j=-\left[\sum_{i=1}^{n_c}(\rho_j x_{ij})\mu_i^{-1/4}\right]^{-4} \qquad j=1,\ldots,n_p \qquad i=1,\ldots,n_c \qquad \text{(B.4)}$$

$$\vec{\vec{D}}_{ij}=\frac{D_{ij}^{o}}{\phi F}+\frac{\alpha_{ij}\vec{u}_j}{\phi} \qquad i=1,\ldots,n_c \qquad j=1,\ldots,n_p \qquad \text{(B.5)}$$

$$\sum_{i=1}^{n_c} x_{ij} = 1 \qquad i = 1,...,n_c \qquad j = 1,...,n_p \tag{B.6}$$

$$\sum_{i=1}^{n_p} S_j = 1 \qquad j = 1,...,n_p \tag{B.7}$$

Additional assumptions made are uniform and constant porosity, anisotropic porous medium and no gravity. The top and bottom boundaries of the reservoir are no flow. The injection well is constant rate, while the producer is constant pressure. We used a simple mixing rule to calculate viscosity of the multicomponent single-phase mixtures. We also assumed that $x_{ij}\rho_j \equiv c_{ij}$.

Introducing the above assumption, equations are reduced to the following forms:

$$\frac{\partial}{\partial t}\phi\sum_{i=1}^{n_c} c_i + \nabla\cdot\sum_{i=1}^{n_c} c_i\vec{u} - \nabla\cdot\phi\sum_{i=1}^{n_c}\vec{\vec{D}}_i\cdot\nabla c_i = 0 \qquad i = 1,...,n_c \tag{B.8}$$

$$\nabla\cdot\vec{u} = 0 \tag{B.9}$$

$$\vec{u} = -\frac{k}{\mu_m}\left(\nabla P\right) \tag{B.10}$$

$$\mu_m = \left[\mu_o^{-1/4} + \beta(\mu_s^{-1/4} - \mu_o^{-1/4})\right]^{-4} \tag{B.11}$$

$$\beta = \frac{c_1 - c_1^I}{c_1^J - c_1^I}, \quad c_1 = \text{injection component} \tag{B.12}$$

$$\vec{\vec{D}}_i = \frac{D_i^o}{\phi F} + \frac{\alpha_i\vec{u}}{\phi} \tag{B.13}$$

$$\sum_{i=1}^{n_c} c_i = 1 \qquad i = 1,...,n_c \tag{B.14}$$

Introducing Arbitrary Scaling Factors:

Two arbitrary scaling factors are introduced for each variable assuming a linear relationship. These scaling factors are substituted into the equations to obtain the dimensionless form of the equations. In all of the following relationship the scaling factors with “2*” are multiplicative term and scaling factors with “1*” are additive and variables with subscript “D” are dimensionless variables.

$$c_i = c_i^{2*} c_{iD} + c_i^{1*}$$

$$x = x^{2*} x_D + x^{1*}$$

$$z = z^{2*} z_D + z^{1*}$$

$$P = P^{2*} P_D + P^{1*}$$

$$t = t^{2*} t_D + t^{1*}$$

$$u_x = u_x^{2*} u_{xD} + u_x^{1*}$$

$$u_z = u_z^{2*} u_{zD} + u_z^{1*} .$$

Substituting Dimensionless Variables with Scaling Factors into Governing Equations and Boundary Conditions:

This section presents all equations after substituting each dimensionless variable by its scaling factors. Each equation has been split into a few terms to easily handle each equation.

Expanding accumulation term of the conservation equation gives:

$$\frac{\partial}{\partial t}(\phi c_i) = \phi \frac{\partial (c_i)}{\partial t} = \phi \frac{\partial (c_i^{2*} c_{iD} + c_i^{1*})}{\partial (t^{2*} t_D + t^{1*})} \qquad i = 1,\ldots,n_c \tag{B.15}$$

$$\frac{\partial}{\partial t}(\phi c_i) \equiv \left[\frac{\phi c_i^{2*}}{t^{2*}}\right]\frac{\partial}{\partial t_D}(c_{iD}) \qquad i=1,\ldots,n_c \tag{B.16}$$

For convection term in the x-direction we have:

$$\begin{aligned}
\frac{\partial}{\partial x}(u_x c_i) &= \left(u_x \frac{\partial c_i}{\partial x}\right) = \left((u_x^{2*}u_{xD}+u_x^{1*})\frac{\partial(c_i^{2*}c_{iD}+c_i^{1*})}{\partial(x^{2*}x_D+x^{1*})}\right)\\
&= \left((u_x^{2*}u_{xD}+u_x^{1*})\frac{c_i^{2*}}{x^{2*}}\frac{\partial(c_{iD})}{\partial(x_D)}\right) \qquad i=1,\ldots,n_c\\
&= \left((\frac{u_x^{2*}c_i^{2*}}{x^{2*}})u_{xD}\frac{\partial(c_{iD})}{\partial(x_D)}+(\frac{c_i^{2*}u_x^{1*}}{x^{2*}})\frac{\partial(c_{iD})}{\partial(x_D)}\right)
\end{aligned} \tag{B.17}$$

Since we do not want to change the original form of the equations and also scaling factors are arbitrary so we set u_x^{1*} equal to zero; hence above equation is reduced to:

$$\frac{\partial}{\partial x}(uc_i) \equiv \left[\frac{u_x^{2*}c_i^{2*}}{x^{2*}}\right]\frac{\partial}{\partial x_D}(u_{xD}c_{iD}) \qquad i=1,\ldots,n_c \tag{B.18}$$

Similarly we can have the same type of derivation in z-direction for convection term.

$$\frac{\partial}{\partial z}(uc_i) \equiv \left[\frac{u_z^{2*}c_i^{2*}}{z^{2*}}\right]\frac{\partial}{\partial z_D}(u_{zD}c_{iD}) \qquad i=1,\ldots,n_c \tag{B.19}$$

Expanding dispersion term in the x-direction gives:

$$\begin{aligned}
\frac{\partial}{\partial x}(\phi D_{ixx}\frac{\partial c_i}{\partial x}) &= \left(\phi D_{ixx}\frac{\partial}{\partial x}\frac{\partial c_i}{\partial x}\right) = \left((\phi D_{ixx})\frac{\partial}{\partial(x^{2*}x_D+x^{1*})}\frac{\partial(c_i^{2*}c_{iD}+c_i^{1*})}{\partial(x^{2*}x_D+x^{1*})}\right)\\
&= \left((\phi D_{ixx})\frac{\partial}{x^{2*}\partial(x_D)}\frac{c_i^{2*}}{x^{2*}}\frac{\partial(c_{iD})}{\partial(x_D)}\right) \qquad i=1,\ldots,n_c\\
&= \left((\frac{\phi D_{ixx}c_i^{2*}}{(x^{2*})^2})\frac{\partial^2 c_{iD}}{\partial x_D{}^2}\right) \equiv \left[\frac{\phi D_{ixx}c_i^{2*}}{(x^{2*})^2}\right]\frac{\partial^2 c_{iD}}{\partial x_D{}^2}
\end{aligned} \tag{B.20}$$

Similarly we can have the same type of derivation in the z-direction for dispersion term.

$$\frac{\partial}{\partial z}(\phi D_{\mathrm{izz}}\frac{\partial c_i}{\partial z})=\left[\frac{\phi D_{izz}c_i^{2*}}{(z^{2*})^2}\right]\frac{\partial^2 c_{iD}}{\partial {z_D}^2} \qquad i=1,\ldots,n_c \tag{B.21}$$

Next we substitute the scaling factors into the continuity equation.

$$\frac{\partial u_x}{\partial x}+\frac{\partial u_z}{\partial z}=\left[\frac{u_x^{2*}}{x^{2*}}\right]\frac{\partial u_{xD}}{\partial x_D}+\left[\frac{u_z^{2*}}{z^{2*}}\right]\frac{\partial u_{zD}}{\partial z_D}=\frac{\partial u_{xD}}{\partial x_D}+\left[\frac{x^{2*}}{u_x^{2*}}\frac{u_z^{2*}}{z^{2*}}\right]\frac{\partial u_{zD}}{\partial z_D} \tag{B.22}$$

Substitution of the scaling factors into the Darcy's equation in the x-direction is given by

$$\begin{aligned}&\vec{u}_x=-\frac{k_x}{\mu_m}\left(\frac{\partial P}{\partial x}\right)= \qquad i=1,\ldots,n_c\\&(u_x^{2*}u_{xD}+u_x^{1*})=-\frac{k_x}{\left[\mu_o^{-1/4}+\beta(\mu_s^{-1/4}-\mu_o^{-1/4})\right]^{-4}}\left(\frac{P^{2*}}{x^{2*}}\right)\frac{\partial P_D}{\partial x_D}\end{aligned} \tag{B.23}$$

$$u_{xD}=-\frac{1}{\left(\left[\frac{u_x^{2*}x^{2*}\left[\beta\right]^{-4}\mu_s}{k_xP^{2*}}\right]^{-1/4}-\left[\frac{u_x^{2*}x^{2*}\left[\beta\right]^{-4}\mu_o}{k_xP^{2*}}\right]^{-1/4}+\left[\frac{u_x^{2*}x^{2*}}{k_xP^{2*}}\right]^{-1/4}{\mu_o}^{-1/4}\right)^{-4}}\cdot\frac{\partial P_D}{\partial x_D} \tag{B.24}$$

Similarly for the z-direction we have:

$$u_{zD}=-\frac{1}{\left(\left[\frac{u_z^{2*}z^{2*}\left[\beta\right]^{-4}\mu_s}{k_zP^{2*}}\right]^{-1/4}-\left[\frac{u_z^{2*}z^{2*}\left[\beta\right]^{-4}\mu_o}{k_zP^{2*}}\right]^{-1/4}+\left[\frac{u_z^{2*}z^{2*}}{k_zP^{2*}}\right]^{-1/4}{\mu_o}^{-1/4}\right)^{-4}}\cdot\frac{\partial P_D}{\partial z_D} \tag{B.25}$$

Initial and Boundary Conditions:

We next introduce initial and boundary conditions and obtain its dimensionless form by substitution of each scaling factor.

$$\begin{array}{lllll}
c_i^{2*} c_{iD} + c_i^{1*} = c_i^I & at & t^{2*} t_D + t^{1*} = t_0 & \forall x_D, z_D & i = 1, \ldots, n_c \\
P^{2*} P_D + P^{1*} = P_0 & at & t^{2*} t_D + t^{1*} = 0 & \forall x_D, z_D & \\
c_1^{2*} c_D + c_1^{1*} = c_1^J & at & x^{2*} x_D + x^{1*} = x_0 & \forall t_D, z_D & \\
u_x^{2*} u_{xD} + u_x^{1*} = u_{inj} & at & x^{2*} x_D + x^{1*} = x_0 & \forall t_D, z_D & \\
P^{2*} P_D + P^{1*} = P_{wf} & at & x^{2*} x_D + x^{1*} = L & \forall t_D, z_D & \\
u_z^{2*} u_{zD} + u_z^{1*} = 0 & at & z^{2*} z_D + z^{1*} = z_0 & \forall t_D, z_D & \\
u_z^{2*} u_{zD} + u_z^{1*} = 0 & at & z^{2*} z_D + z^{1*} = H & \forall t_D, z_D &
\end{array}$$

In dimensionless form, initial and boundary equations are set to one or zero; therefore, the dimensionless form of the variables is given by,

$$\begin{array}{llll}
c_{iD} = \left[\dfrac{c_i^I - c_i^{1*}}{c_i^{2*}} \right] & at & t_D = \left[\dfrac{t_0 - t^{1*}}{t^{2*}} \right] & \forall x_D, z_D \\
P_D = \left[\dfrac{P_0 - P^{1*}}{P^{2*}} \right] & at & t_D = \left[\dfrac{t_0 - t^{1*}}{t^{2*}} \right] & \forall x_D, z_D \\
c_{1D} = \left[\dfrac{c_1^J - c_1^{1*}}{c_1^{2*}} \right] & at & x_D = \left[\dfrac{x_0 - x^{1*}}{x^{2*}} \right] & \forall t_D, z_D \\
u_{xD} = \left[\dfrac{u_{inj}}{u_x^{2*}} \right] & at & x_D = \left[\dfrac{x_0 - x^{1*}}{x^{2*}} \right] & \forall t_D, z_D \\
P_D = \left[\dfrac{P_{wf} - P^{1*}}{P^{2*}} \right] & at & x_D = \left[\dfrac{L - x^{1*}}{x^{2*}} \right] & \forall t_D, z_D \\
u_{zD} = 0 & at & z_D = \left[\dfrac{z_0 - z^{1*}}{z^{2*}} \right] & \forall t_D, z_D \\
u_{zD} = 0 & at & z_D = \left[\dfrac{H - z^{1*}}{z^{2*}} \right] & \forall t_D, z_D
\end{array}$$

Then we set B.C's and I.C's equal to zero or one, where it is appropriate

$$\begin{array}{llll}
c_{iD} = 0 & at & t_D = 0 \quad \forall x_D, z_D & i = 1,\ldots,n_c \\
P_D = 0 & at & t_D = 0 \quad \forall x_D, z_D & \\
c_{1D} = 1 & at & x_D = 0 \quad \forall t_D, z_D & \\
u_{xD} = 1 & at & x_D = 0 \quad \forall t_D, z_D & \\
P_D = 1 & at & x_D = 1 \quad \forall t_D, z_D & \\
u_{zD} = 0 & at & z_D = 0 \quad \forall t_D, z_D & \\
u_{zD} = 0 & at & z_D = 0 \quad \forall t_D, z_D &
\end{array}$$

Using the given initial and boundary conditions, scaling factors are

$$c_i^{1*} = c_i^I$$

$$c_1^{2*} = (c_1^J - c_1^I)$$

$$u_x^{2*} = u_{inj}$$

$$P^{1*} = P_0$$

$$P^{2*} = (P_{wf} - P_0)$$

$$t^{1*} = t_0$$

$$x^{1*} = x_0$$

$$x^{2*} = (L - x_0)$$

$$z^{1*} = z_0$$

$$z^{2*} = (H - y_0)$$

$$x^{1*} = z^{1*} = 0\,.$$

Dimensionless Form of the Equations:

After substitution of the scaling factors, the initial and boundary equation to the initial equation the dimensionless form of the conservation equation are given by,

$$\frac{\partial}{\partial t_D}(c_{iD})+\overset{\boxed{1}}{\left[\frac{u_x^{2*}t^{2*}}{\phi x^{2*}}\right]}\frac{\partial}{\partial x_D}(u_{xD}c_{iD})+\overset{\boxed{2}}{\left[\frac{u_z^{2*}t^{2*}}{\phi z^{2*}}\right]}\frac{\partial}{\partial z_D}(u_{zD}c_{iD})=$$

$$\underset{\boxed{3}}{\left[\frac{D_{ixx}t^{2*}}{(x^{2*})^2}\right]}\frac{\partial^2}{\partial {x_D}^2}+\underset{\boxed{4}}{\left[\frac{D_{izz}t^{2*}}{(z^{2*})^2}\right]}\frac{\partial^2 c_{iD}}{\partial {z_D}^2}$$

and the dimensionless form for continuity equation is:

$$\frac{\partial u_x}{\partial x}+\frac{\partial u_z}{\partial z}=\frac{\partial u_{xD}}{\partial x_D}+\underset{\boxed{5}}{\left[\frac{x^{2*}u_z^{2*}}{u_x^{2*}z^{2*}}\right]}\frac{\partial u_{zD}}{\partial z_D}$$

The dimensionless form of Darcy's equation is presented as:

$$u_{xD}=-\frac{1}{\left(\underset{\boxed{6}}{\left[\frac{u_x^{2*}x^{2*}\left[\beta\right]^{-4}\mu_s}{k_xP^{2*}}\right]^{-1/4}}-\underset{\boxed{7}}{\left[\frac{u_x^{2*}x^{2*}\left[\beta\right]^{-4}\mu_o}{k_xP^{2*}}\right]^{-1/4}}+\underset{\boxed{8}}{\left[\frac{u_x^{2*}x^{2*}}{k_xP^{2*}}\right]^{-1/4}}\mu_o^{-1/4}\right)^{-4}}\frac{\partial P_D}{\partial x_D}$$

$$u_{zD}=-\frac{1}{\left(\underset{\boxed{9}}{\left[\frac{u_z^{2*}y^{2*}\left[\beta\right]^{-4}\mu_s}{k_zP^{2*}}\right]^{-1/4}}-\underset{\boxed{10}}{\left[\frac{u_z^{2*}z^{2*}\left[\beta\right]^{-4}\mu_o}{k_zP^{2*}}\right]^{-1/4}}+\underset{\boxed{11}}{\left[\frac{u_z^{2*}z^{2*}}{k_zP^{2*}}\right]^{-1/4}}\mu_o^{-1/4}\right)^{-4}}\frac{\partial P_D}{\partial z_D}$$

We then set the first and second groups in the conservation equation to be 1; therefore, group 3 in the conservation equation is

$$\frac{\phi D_{xx}}{u_{inj}L}=\frac{1}{N_{Pex}} \tag{B.26}$$

and group 4 in the conservation equation is given by,

$$\frac{\phi D_{zz}}{Hu_{inj}}\frac{L}{H}=\frac{1}{N_{Pez}} \tag{B.27}$$

Group 5 is equal to 1.0 from the first and second groups. Darcy's equation is simplified to the following equation.

$$u_{xD}=-\frac{1}{\left(1+(\left[\frac{1}{\beta^{-4}}\right]-1)\left[\frac{\mu_o}{\mu_s}\right]^{-1/4}\right)^{-4}}\frac{\partial P_D}{\partial x_D}$$

$$u_{zD}=-\frac{1}{\left(1+(\left[\frac{1}{\beta^{-4}}\right]-1)\left[\frac{\mu_o}{\mu_s}\right]^{-1/4}\right)^{-4}}\frac{\partial P_D}{\partial z_D}$$

The first group in Darcy's equation is set to one and the second group is the mobility ratio.

$$M=\left[\frac{\mu_o}{\mu_s}\right] \tag{B.28}$$

Knowing that $u_x^{2*}=u_{inj}$, Darcy's equation in the z-direction is

$$u_{zD}=\left[\frac{k_z}{k_x}\frac{L^2}{H^2}\right]\frac{1}{\mu_{mD}}\frac{\partial P_D}{\partial z_D} \tag{B.29}$$

Therefore, the last group is defined as:

$$\left[\frac{k_z}{k_x}\frac{L^2}{H^2}\right]=(R_L)^2. \tag{B.30}$$

Final Dimensionless Variables and Scaling Groups

Considering the scaling factors, the final form of the dimensionless variables is given by,

$$c_{iD} = \frac{c_i - c_i^I}{c_i^J - c_i^I} \tag{B.31}$$

$$x_D = \frac{x - x_0}{L} \tag{B.32}$$

$$z_D = \frac{z - z_0}{H} \tag{B.33}$$

$$P_D = \frac{P - P_0}{P_{wf} - P_0} \tag{B.34}$$

$$u_{xD} = \frac{u_x}{u_{inj}} \tag{B.35}$$

$$u_{zD} = \frac{u_z}{u_{inj}} \frac{L}{H} \tag{B.36}$$

$$t_D = \frac{u_{inj} t}{\phi L} \tag{B.37}$$

and final form of the scaling groups is presented as:

$$G_1 = \left[\frac{u_{inj} L}{\phi D_{xx}} \right]. \tag{B.38}$$

$$G_2 = \left[\frac{u_{inj}}{\phi D_{zz}} \frac{H^2}{L} \right] \tag{B.39}$$

$$G_3 = \left[\frac{L^2}{H^2} \frac{k_z}{k_x} \right] \tag{B.40}$$

$$G_4 = \left[\frac{\mu_o}{\mu_s} \right]. \tag{B.41}$$

Minimizing the Scaling Groups:

The matrix rank method is used to minimize the number of dimensionless group (Shook *et al.,* 1992). In this method the logarithm of both sides of the dimensionless groups is taken to convert the equation as a linear combination of parameters.

The resulting matrix, which is a linear system of four equations with ten unknowns, is as follow:

$$\begin{bmatrix} Ln\,G_1 \\ Ln\,G_2 \\ Ln\,G_3 \\ Ln\,G_4 \end{bmatrix} = \begin{bmatrix} 1 & 0 & 0 & 0 & 0 & 0 & 1 & -1 & -1 & 0 \\ -1 & 2 & 0 & 0 & 0 & 0 & 1 & -1 & 0 & -1 \\ 2 & -2 & -1 & 1 & 0 & 0 & 0 & 0 & 0 & 0 \\ 0 & 0 & 0 & 0 & -1 & 1 & 0 & 0 & 0 & 0 \end{bmatrix} \begin{bmatrix} ln\,L \\ ln\,H \\ ln\,k_x \\ ln\,k_z \\ ln\,\mu_s \\ ln\,\mu_o \\ ln\,u_{inj} \\ ln\,\phi \\ ln\,D_{xx} \\ ln\,D_{zz} \end{bmatrix}$$

Next, the rank of the resulting coefficient matrix is calculated and the number of independent scaling groups is then equal to the rank of the coefficient matrix. The reduced coefficient matrix is:

$$\begin{bmatrix} 1 & 0 & 0 & 0 & 0 & 0 & 1 & -1 & -1 & 0 \\ -1 & 1 & 0 & 0 & 0 & 0 & 0 & 0 & -0.5 & 0.5 \\ 0 & 0 & 1 & -1 & 0 & 0 & 0 & 0 & -1 & 1 \\ 0 & 0 & 0 & 0 & -1 & 1 & 0 & 0 & 0 & 0 \end{bmatrix}$$

After exponentiation, the scaling groups are given as:

$$G_1 = \left[\frac{u_{inj} L}{\phi D_{xx}} \right]$$

$$G_2 = \left[\frac{L}{H} \sqrt{\frac{D_{zz}}{D_{xx}}} \right]$$

$$G_3 = \left[\frac{k_x D_{zz}}{k_z D_{xx}} \right]$$

$$G_4 = \left[\frac{\mu_o}{\mu_s} \right].$$

Considering the physical meaning and the traditional scaling groups, the final groups for first contact miscible displacements are:

$$G_1^f = N_{pe} = \left[\frac{u_{inj} L}{\phi D_{xx}} \right] \qquad \text{= Longitudinal Peclet number} \qquad \text{(B.42)}$$

$$G_2^f = N_D = \left[\frac{L}{H} \sqrt{\frac{D_{zz}}{D_{xx}}} \right] \qquad = \text{Dispersion number} \qquad \text{(B.43)}$$

$$G_3^f = R_L = \left[\frac{L}{H} \sqrt{\frac{k_z}{k_x}} \right] \qquad = \text{Effective aspect ratio} \qquad \text{(B.44)}$$

$$G_4^f = M = \left[\frac{\mu_o}{\mu_s} \right] \qquad = \text{Mobility ratio} \qquad \text{(B.45)}$$

Appendix C: Numerical Dispersion and Dispersion Tensor

Mathematically, the numerical dispersion term in the convection-dispersion equation can be obtained from the truncation error generated from the numerical finite difference formulation of the convection-dispersion equation (Peaceman and Rachford, 1962; Price *et al.*, 1968; Lantz, 1971; Peaceman 1977).

The one-dimensional form of the convection equation is:

$$\phi \frac{\partial C}{\partial t} + u \frac{\partial C}{\partial x} = 0 . \tag{C.1}$$

where C is the tracer concentration in the single-phase fluid, ϕ is the formation porosity, and u is the Darcy velocity, which is assumed to be constant with respect to distance. The differential form of equation (C.1) is obtained by approximating the special and temporal derivatives. The discretization of the spatial derivative of equation (C.1) yields

$$\frac{\partial C}{\partial x} \approx -\frac{C_{i+1/2} - C_{i-1/2}}{\Delta x} . \tag{C.2}$$

In the above equation, concentrations are only available at the center of grid-blocks. In order to evaluate concentrations at the grid-block face, a single parameter ω is introduced by Peaceman (1977). The general equations are:

$$C_{i+1/2} = [\omega]C_i + [1-\omega]C_{i+1} \tag{C.3}$$

$$C_{i-1/2} = [\omega]C_{i-1} + [1-\omega]C_i \tag{C.4}$$

where parameter ω specifies the weighting schemes as:

Upstream weighting: $\omega = 1$
Midpoint weighting: $\omega = 1/2$
Downstream weighting: $\omega = 0$.

Discretization in time can also be characterized similar to the spatial discretization for implicit, explicit and centered-in-time. If θ is chosen as the time weighting factor, then

Implicit (t^{n+1}): $\theta = 1$
Centered-in-time ($t^{n+1/2}$): $\theta = 1/2$
Explicit (t^{n}): $\theta = 0$.

Equation (C.1) can then be written in the following differential form.

$$\phi \frac{C_i^{n+1} - C_i^n}{\Delta t} = -\frac{u}{\Delta x}\left[\theta\left(C_{i+1/2}^{n+1} - C_{i-1/2}^{n+1}\right) + (1-\theta)\left(C_{i+1/2}^{n} - C_{i-1/2}^{n}\right)\right]. \tag{C.5}$$

Each elements of the concentration at the center of the grid-block can then be converted through use of equations (C.3) and (C.4).

As an example, for an upstream weighting with distance and explicit in time, i.e. $\omega = 1$ and $\theta = 0$, equation (C.5) is given by:

$$\phi \frac{C_i^{n+1} - C_i^n}{\Delta t} = -\frac{u}{\Delta x}\left[\left(C_i^n - C_{i-1}^n\right)\right] \tag{C.6}$$

Taylor's series expansion is performed about C_i^n for both spatial and temporal differences to investigate the truncation error in equation(C.6).

$$C_{i-1}^n = C_i^n - \frac{\Delta x}{1!}\frac{\partial C}{\partial x} + \frac{(\Delta x)^2}{2!}\frac{\partial^2 C}{\partial^2 x} \pm HOT(\text{Higher Order Terms})\,. \tag{C.7}$$

Thus we have

$$\frac{C_i^n - C_{i-1}^n}{\Delta x} = \frac{\partial C}{\partial x} - \frac{\Delta x}{2}\frac{\partial^2 C}{\partial x^2} \pm HOT \tag{C.8}$$

and for temporal expansion

$$C_i^{n+1} = C_i^n + \frac{\Delta t}{1!}\frac{\partial C}{\partial t} + \frac{(\Delta t)^2}{2!}\frac{\partial^2 C}{\partial^2 t} \pm HOT\ . \tag{C.9}$$

Therefore the differential form is

$$\frac{C_i^{n+1} - C_i^n}{\Delta t} = \frac{\partial C}{\partial t} + \frac{\Delta t}{2}\frac{\partial^2 C}{\partial t^2} \pm HOT\,. \tag{C.10}$$

The second order term $\partial^2 C / \partial t^2$ in equation (C.10) can be expressed in terms of a derivative with respect to space by differentiating equation (C.1)

$$\frac{\partial^2 C}{\partial t^2} = -\frac{u}{\phi}\frac{\partial}{\partial t}\left(\frac{\partial C}{\partial x}\right) = -\frac{u}{\phi}\frac{\partial}{\partial x}\left(\frac{\partial C}{\partial t}\right) \tag{C.11}$$

$$\frac{\partial^2 C}{\partial t^2} = -\frac{u}{\phi}\frac{\partial}{\partial x}\left(-\frac{u}{\phi}\frac{\partial C}{\partial x}\right) = \frac{u^2}{\phi^2}\frac{\partial^2 C}{\partial x^2}\,. \tag{C.12}$$

We multiply equation(C.8) by u and equation(C.10) by ϕ and then add them up. And we neglect all higher order terms

$$u\left(\frac{C_i^n - C_{i-1}^n}{\Delta x}\right) + \phi\left(\frac{C_i^{n+1} - C_i^n}{\Delta t}\right) = u\frac{\partial C}{\partial x} + \phi\frac{\partial C}{\partial t} - \frac{u\Delta x}{2}\frac{\partial^2 C}{\partial x^2} + \frac{\phi\Delta t}{2}\frac{\partial^2 C}{\partial t^2} \tag{C.13}$$

Next we use equation (C.12) and neglect all higher order terms

$$u\left(\frac{C_i^n - C_{i-1}^n}{\Delta x}\right) + \phi\left(\frac{C_i^{n+1} - C_i^n}{\Delta t}\right) = u\frac{\partial C}{\partial x} + \phi\frac{\partial C}{\partial t} - \frac{u\Delta x}{2\phi}\left(1 - \frac{u\Delta t}{\phi\Delta x}\right)\phi\frac{\partial^2 C}{\partial x^2} \qquad \text{(C.14)}$$

It can be observed that the difference approximation of equation (C.1) has the truncation error form given by:

$$\varepsilon = -\frac{u\Delta x}{2\phi}\left(1 - \frac{u\Delta t}{\phi\Delta x}\right)\phi\frac{\partial^2 C}{\partial x^2} \qquad \text{(C.15)}$$

where $\left(\frac{u\Delta t}{\phi\Delta x}\right)$ is the Courant number (N_{Co}). Thus the above equation is reduced to

$$\varepsilon = -\frac{u\Delta x}{2\phi}\left(1 - N_{Co}\right)\phi\frac{\partial^2 C}{\partial x^2}. \qquad \text{(C.16)}$$

The coefficient in front of $\phi\frac{\partial^2 C}{\partial x^2}$ is the numerical dispersion.

$$D_{num} = \frac{u\Delta x}{2\phi}\left(1 - N_{Co}\right) \qquad \text{(C.17)}$$

Therefore equation (C.14) takes the form:

$$u\left(\frac{C_i^n - C_{i-1}^n}{\Delta x}\right) + \phi\left(\frac{C_i^{n+1} - C_i^n}{\Delta t}\right) = u\frac{\partial C}{\partial x} + \phi\frac{\partial C}{\partial t} - \phi D_{num}\frac{\partial^2 C}{\partial x^2} \qquad \text{(C.18)}$$

Thus by solving equation(C.6), we solve the convection-dispersion equation.

$$\phi\frac{\partial C}{\partial t} = -u\frac{\partial C}{\partial x} - \phi D_{num}\frac{\partial^2 C}{\partial x^2}. \qquad \text{(C.19)}$$

For small Courant number, $\frac{u\Delta t}{\phi} << \Delta x$, numerical dispersion takes the form:

$$D_{num} = \left(\frac{u}{\phi}\right)\frac{\Delta x}{2} \tag{C.20}$$

Thus, in a linear 1-D system, the dispersivity is equal to half of the grid-block size, when Courant number is small.

The derived numerical dispersion in equation (C.17) is for the specific case of one-point upstream weighting in distance and explicit in time differencing (Lantz, 1971). Peaceman (1977) presents a generalized form for numerical dispersion, D_{num}, for different combination of spatial and temporal differencing given by,

$$D_{num} = \frac{u\Delta x}{\phi}\left[\left(W - \frac{1}{2}\right) + N_{Co}\left(\theta - \frac{1}{2}\right)\right] \tag{C.21}$$

The numerical dispersion term does not appear in mid-point distance weighting and centered-in-time (Crank-Nicolson) differencing scheme, which makes the numerical dispersion associated with this scheme leads to zero. However, this condition does not ensure that Crank-Nicolson scheme is numerical dispersion free. This method of discretization often leads to artificial oscillations.

Fanchi (1983) derived the numerical dispersion tensor for a variety of finite-difference schemes for single-phase flow in multidimensional reservoirs (Table C.1).

The 3-D form of the convection dispersion equation is:

$$\frac{\partial C}{\partial t} = \sum_{i=1}^{3}\left(\sum_{j=1}^{3} D_{ij}\frac{\partial^2 C}{\partial x_i x_j} - v_i\frac{\partial C}{\partial x_i}\right) \tag{C.22}$$

where D_{ij} is the dispersion tensor, v_i is the interstitial velocity in the i direction, x_i and x_j are the corresponding spatial directions.

As an example, the 2-D convection equation is:

$$\frac{\partial C}{\partial t} = -v_x \frac{\partial C}{\partial x} - v_y \frac{\partial C}{\partial y} \tag{C.23}$$

For upstream weighting with distance and implicit in time, i.e. $\omega = 1$ and $\theta = 1$, the discretization for of equation (C.23) is given by:

$$\frac{C_{ij}^{n} - C_{ij}^{n-1}}{\Delta t} = -v_x \left[\left(\frac{C_{ij}^{n} - C_{i-1j}^{n}}{\Delta x} \right) \right] - v_y \left[\left(\frac{C_{ij}^{n} - C_{ij-1}^{n}}{\Delta y} \right) \right] \tag{C.24}$$

Taylor's series expansion is performed about C_{ij}^{n} for both spatial and temporal differences to investigate the truncation error in equation(C.24). Therefore the differential forms for both spatial and temporal are

$$\frac{C_{ij}^{n} - C_{ij}^{n-1}}{\Delta t} = \frac{\partial C}{\partial t} - \frac{\Delta t}{2} \frac{\partial^2 C}{\partial t^2} \pm HOT \tag{C.25}$$

$$\frac{C_{ij}^{n} - C_{i-1j}^{n}}{\Delta x} = \frac{\partial C}{\partial x} - \frac{\Delta x}{2} \frac{\partial^2 C}{\partial x^2} \pm HOT \tag{C.26}$$

$$\frac{C_{ij}^{n} - C_{ij-1}^{n}}{\Delta y} = \frac{\partial C}{\partial y} - \frac{\Delta y}{2} \frac{\partial^2 C}{\partial y^2} \pm HOT \tag{C.27}$$

Equation (C.24) is then replaced by its Taylor's series expansion

$$\begin{aligned} &\frac{C_{ij}^{n} - C_{ij}^{n-1}}{\Delta t} + v_x \left[\left(\frac{C_{ij}^{n} - C_{i-1j}^{n}}{\Delta x} \right) \right] + v_y \left[\left(\frac{C_{ij}^{n} - C_{ij-1}^{n}}{\Delta y} \right) \right] = \left(\frac{\partial C}{\partial t} - \frac{\Delta t}{2} \frac{\partial^2 C}{\partial t^2} \right) \\ &+ v_x \left(\frac{\partial C}{\partial x} - \frac{\Delta x}{2} \frac{\partial^2 C}{\partial x^2} \right) + v_y \left(\frac{\partial C}{\partial y} - \frac{\Delta y}{2} \frac{\partial^2 C}{\partial y^2} \right) \end{aligned} \tag{C.28}$$

The second order term $\partial^2 C/\partial t^2$ in equation (C.25) can be expressed in terms of a derivative with respect to space by differentiating equation (C.23)

$$\begin{aligned}\frac{\partial^2 C}{\partial t^2} &= -\frac{\partial}{\partial t}\left(v_x\frac{\partial C}{\partial x}+v_y\frac{\partial C}{\partial y}\right) = -\left(v_x\frac{\partial}{\partial x}\frac{\partial C}{\partial t}+v_y\frac{\partial}{\partial y}\frac{\partial C}{\partial t}\right)\\ &= -\left(v_x\frac{\partial}{\partial x}\left(-v_x\frac{\partial C}{\partial x}-v_y\frac{\partial C}{\partial y}\right)+v_y\frac{\partial}{\partial y}\left(-v_x\frac{\partial C}{\partial x}-v_y\frac{\partial C}{\partial y}\right)\right)\\ &= v_x^2\frac{\partial^2 C}{\partial x^2}+v_xv_y\frac{\partial^2 C}{\partial x\partial y}+v_y^2\frac{\partial^2 C}{\partial y^2}+v_yv_x\frac{\partial^2 C}{\partial y\partial x}\end{aligned} \tag{C.29}$$

The term $\partial^2 C/\partial t^2$ in equation (C.28) is replaced by equation (C.29)

$$\begin{aligned}&\frac{C_{ij}^{n}-C_{ij}^{n-1}}{\Delta t}+v_x\left[\left(\frac{C_{ij}^{n}-C_{i-1j}^{n}}{\Delta x}\right)\right]+v_y\left[\left(\frac{C_{ij}^{n}-C_{ij-1}^{n}}{\Delta y}\right)\right]=\frac{\partial C}{\partial t}+v_x\left(\frac{\partial C}{\partial x}\right)+v_y\left(\frac{\partial C}{\partial y}\right)\\ &-\frac{\Delta t}{2}\left(v_x^2\frac{\partial^2 C}{\partial x^2}+v_xv_y\frac{\partial^2 C}{\partial x\partial y}+v_y^2\frac{\partial^2 C}{\partial y^2}+v_yv_x\frac{\partial^2 C}{\partial y\partial x}\right)-\frac{\Delta x}{2}\left(\frac{\partial^2 C}{\partial x^2}\right)-\frac{\Delta y}{2}\left(\frac{\partial^2 C}{\partial y^2}\right)=\\ &\frac{\partial C}{\partial t}+v_x\left(\frac{\partial C}{\partial x}\right)+v_y\left(\frac{\partial C}{\partial y}\right)-\\ &\frac{1}{2}(v_x\left(\Delta x+v_x\Delta t\right)\left(\frac{\partial^2 C}{\partial x^2}\right)+v_xv_y\Delta t\left(\frac{\partial^2 C}{\partial x\partial y}\right)+v_y\left(\Delta y+v_y\Delta t\right)\left(\frac{\partial^2 C}{\partial y^2}\right)+\\ &v_yv_x\Delta t\left(\frac{\partial^2 C}{\partial y\partial x}\right))\end{aligned} \tag{C.30}$$

It can be observed that the difference approximation of equation (C.23) has the truncation error form given by:

$$\begin{aligned}\varepsilon = &\frac{1}{2}(v_x\left(\Delta x+v_x\Delta t\right)\left(\frac{\partial^2 C}{\partial x^2}\right)+v_xv_y\Delta t\left(\frac{\partial^2 C}{\partial x\partial y}\right)+v_y\left(\Delta y+v_y\Delta t\right)\left(\frac{\partial^2 C}{\partial y^2}\right)+\\ &v_yv_x\Delta t\left(\frac{\partial^2 C}{\partial y\partial x}\right))\end{aligned} \tag{C.31}$$

The coefficient in front of $\frac{\partial^2 C}{\partial x^2}$, $\frac{\partial^2 C}{\partial y^2}$, $\frac{\partial^2 C}{\partial x \partial y}$, $\frac{\partial^2 C}{\partial y \partial x}$ are the numerical dispersions in different directions.

In three-dimensions where the finite difference scheme uses backward spatial differences, and is implicit in time, numerical dispersion tensor is given by

$$\vec{\vec{D}}_{num} = \frac{1}{2} \begin{bmatrix} v_x \left(\Delta x + v_x \Delta t \right) & v_x v_y \Delta t & v_x v_z \Delta t \\ v_y v_x \Delta t & v_y \left(\Delta y + v_y \Delta t \right) & v_y v_z \Delta t \\ v_z v_x & v_z v_y \Delta t & v_z \left(\Delta z + v_z \Delta t \right) \end{bmatrix} \tag{C.32}$$

The hydrodynamic dispersion tensor in three-dimensions is given by,

$$\vec{\vec{D}}_i = \begin{bmatrix} D_{xx} & D_{xy} & D_{xz} \\ D_{yx} & D_{yy} & D_{yz} \\ D_{zx} & D_{zy} & D_{zz} \end{bmatrix}, \tag{C.33}$$

where each element of the tensor (including numerical dispersion from Eq. (C.32) is given by,

$$D_{xx} = \frac{D_o}{\tau} + \alpha_L \frac{v_x^2}{|v|} + \alpha_T \frac{v_y^2}{|v|} + \alpha_T \frac{v_z^2}{|v|} + \frac{1}{2} v_x \left(\Delta x + v_x \Delta t \right), \tag{C.34}$$

$$D_{yy} = \frac{D_o}{\tau} + \alpha_T \frac{v_x^2}{|v|} + \alpha_L \frac{v_y^2}{|v|} + \alpha_T \frac{v_z^2}{|v|} + \frac{1}{2} v_y \left(\Delta y + v_y \Delta t \right), \tag{C.35}$$

$$D_{zz} = \frac{D_o}{\tau} + \alpha_T \frac{v_x^2}{|v|} + \alpha_T \frac{v_y^2}{|v|} + \alpha_L \frac{v_z^2}{|v|} + \frac{1}{2} v_z \left(\Delta z + v_z \Delta t \right), \tag{C.36}$$

$$D_{xy} = D_{yx} = (\alpha_L - \alpha_T)\frac{v_x v_y}{|v|} + \frac{1}{2} v_x v_y \Delta t \tag{C.37}$$

$$D_{xz} = D_{zx} = (\alpha_L - \alpha_T)\frac{v_x v_z}{|v|} + \frac{1}{2} v_x v_z \Delta t \tag{C.38}$$

$$D_{yz} = D_{zy} = (\alpha_L - \alpha_T)\frac{v_y v_z}{|v|} + \frac{1}{2} v_y v_z \Delta t \tag{C.39}$$

Special Case:

For 1-D flow and 2-D transport, $v_Z = 0$ and Eqs. (C.34) , (C.36) and (C.38) become,

$$D_{xx} = \frac{D_o}{\tau} + \alpha_L v_x + \frac{1}{2} v_x \left(\Delta x + v_x \Delta t\right) = D_L \tag{C.40}$$

$$D_{zz} = \frac{D_o}{\tau} + \alpha_T v_x = D_T \tag{C.41}$$

$$D_{xz} = D_{zx} = 0 \tag{C.42}$$

Often the time-step size Δt is made sufficiently small so that its contribution to numerical dispersion is negligible. We always use a Courant number ($v_{inj}\Delta t / \Delta x$) less than 0.05. We also neglect the diffusion terms in Eqs. (C.34) to (C.39) because it is much smaller than the other terms for most injection velocities (Lake, 1989). This does not negate the importance of diffusion, however, in mixing of gas with oil.

Difference technique		Numerical Dispersion Tensor, $\mathbf{D}_{num}$
Space	Time	ijth Element
Backward-difference	Explicit	$\begin{cases} \frac{v_i}{2}\left(\Delta x_i - v_i \Delta t\right), & i = j \\ -\frac{1}{2} v_i v_j \Delta t, & i \neq j \end{cases}$
Centered-difference	Explicit	$-\frac{1}{2} v_i v_j \Delta t, \quad all\ i, j$
Backward-difference	Implicit	$\begin{cases} \frac{v_i}{2}\left(\Delta x_i + v_i \Delta t\right), & i = j \\ \frac{1}{2} v_i v_j \Delta t, & i \neq j \end{cases}$
Centered-difference	Implicit	$\frac{1}{2} v_i v_j \Delta t, \quad all\ i, j$

Table C.1: Multi-dimensional numerical dispersion, Fanchi (1983)

Appendix D: Coefficients for Response Functions

In this appendix the response functions coefficients and input values for the experimental design are given. Dimensional input values for blind test and validation tests also are given in this appendix.

	X_D=0.25	X_D =0.5	X_D =0.75	X_D =1.0
β0	0.0488	0.0885	0.1640	0.2002
β1	0.0062	0.0087	0.0146	0.0173
β2	-0.0036	-0.0036	-0.0112	-0.0115
β3	0.0186	0.0284	0.0403	0.0426
β4	0.0069	0.0154	0.0174	0.0214
β5	0.0080	0.0190	0.0171	0.0174
β6	0.0015	-0.0019	0.0056	0.0029
β12	-0.0005	-0.0012	-0.0048	-0.0031
β13	0.0089	0.0081	0.0170	0.0189
β14	-0.0003	-0.0015	-0.0021	0.0008
β15	0.0012	0.0003	-0.0024	-0.0049
β16	-0.0002	-0.0018	0.0040	0.0016
β23	-0.0029	-0.0020	-0.0047	-0.0077
β24	0.0011	0.0028	0.0044	0.0047
β25	0.0000	0.0022	-0.0023	-0.0037
β26	0.0011	0.0037	0.0015	-0.0001
β34	0.0050	0.0125	0.0135	0.0097
β35	0.0015	0.0024	0.0015	0.0017
β36	-0.0009	-0.0017	-0.0023	-0.0033
β45	0.0030	0.0081	0.0086	0.0101
β46	-0.0023	-0.0009	-0.0030	-0.0066
β56	0.0009	-0.0052	-0.0010	-0.0024
β11	-0.0079	-0.0228	-0.0498	-0.0407
β22	-0.0053	-0.0073	-0.0084	-0.0211
β33	0.0025	0.0042	0.0026	0.0010
β44	-0.0134	-0.0156	-0.0355	-0.0506
β55	-0.0126	-0.0173	-0.0468	-0.0597
β66	-0.0021	-0.0038	-0.0110	-0.0180

Table D.1: Response surface coefficients for dimensionless local dispersivity estimation (see Eq. (3.15)). The subscript number is based on the order in Table 3.4.

	X_D=0.25	**X_D =0.5**	**X_D =0.75**	**X_D =1.0**
β_{0}	0.0358	0.0668	0.0921	0.1383
β_{1}	0.0071	0.0094	0.0141	0.0204
β_{2}	-0.0046	-0.0083	-0.0128	-0.0149
β_{3}	0.0172	0.0217	0.0304	0.0337
β_{4}	0.0041	0.0076	0.0065	0.0056
β_{5}	0.0095	0.0129	0.0108	0.0117
β_{6}	-0.0014	-0.0066	-0.0033	0.0004
β_{12}	0.0007	-0.0001	-0.0014	-0.0014
β_{13}	0.0061	0.0046	0.0096	0.0156
β_{14}	0.0016	0.0016	0.0037	0.0021
β_{15}	0.0023	-0.0002	-0.0010	-0.0011
β_{16}	-0.0023	-0.0034	-0.0022	-0.0015
β_{23}	-0.0050	-0.0063	-0.0077	-0.0117
β_{24}	0.0020	-0.0006	-0.0006	0.0025
β_{25}	-0.0014	0.0000	-0.0007	-0.0027
β_{26}	0.0009	0.0019	0.0007	-0.0010
β_{34}	0.0022	0.0061	0.0056	0.0011
β_{35}	0.0047	0.0010	-0.0019	-0.0043
β_{36}	-0.0007	-0.0014	-0.0007	0.0019
β_{45}	0.0000	0.0011	-0.0009	-0.0023
β_{46}	0.0008	-0.0004	-0.0012	-0.0010
β_{56}	-0.0008	-0.0065	-0.0032	-0.0001
β_{11}	-0.0003	-0.0074	-0.0030	-0.0117
β_{22}	-0.0048	-0.0038	-0.0029	-0.0129
β_{33}	0.0053	0.0049	0.0051	0.0048
β_{44}	-0.0101	-0.0143	-0.0257	-0.0346
β_{55}	-0.0058	-0.0141	-0.0246	-0.0360
β_{66}	-0.0016	-0.0038	-0.0069	-0.0117

Table D.2: Updated response coefficients that include all 750 simulations. The subscript number is based on the order in Table 3.4.

Scaling groups	λ_{xD}	λ_{zD}	V_{DP}	N_D	M	R_L	N_{Pe}
1	0.10	0.02	0.60	1.00	5.00	6.00	512.00
2	0.10	0.02	0.60	10.00	5.00	6.00	512.00
3	0.10	0.50	0.60	1.00	5.00	6.00	512.00
4	0.10	0.50	0.60	10.00	5.00	6.00	512.00
5	2.00	0.02	0.60	1.00	5.00	6.00	512.00
6	2.00	0.02	0.60	10.00	5.00	6.00	512.00
7	2.00	0.50	0.60	1.00	5.00	6.00	512.00
8	2.00	0.50	0.60	10.00	5.00	6.00	512.00
9	0.25	0.02	0.40	3.30	1.00	6.00	512.00
10	0.25	0.02	0.40	3.30	25.00	6.00	512.00
11	0.25	0.02	0.80	3.30	1.00	6.00	512.00
12	0.25	0.02	0.80	3.30	25.00	6.00	512.00
13	0.25	0.50	0.40	3.30	1.00	6.00	512.00
14	0.25	0.50	0.40	3.30	25.00	6.00	512.00
15	0.25	0.50	0.80	3.30	1.00	6.00	512.00
16	0.25	0.50	0.80	3.30	25.00	6.00	512.00
17	0.25	0.10	0.40	1.00	5.00	0.10	512.00
18	0.25	0.10	0.40	1.00	5.00	10.00	512.00
19	0.25	0.10	0.40	10.00	5.00	0.10	512.00
20	0.25	0.10	0.40	10.00	5.00	10.00	512.00
21	0.25	0.10	0.80	1.00	5.00	0.10	512.00
22	0.25	0.10	0.80	1.00	5.00	10.00	512.00
23	0.25	0.10	0.80	10.00	5.00	0.10	512.00
24	0.25	0.10	0.80	10.00	5.00	10.00	512.00
25	0.10	0.10	0.60	1.00	1.00	6.00	512.00
26	0.10	0.10	0.60	1.00	25.00	6.00	512.00
27	0.10	0.10	0.60	10.00	1.00	6.00	512.00
28	0.10	0.10	0.60	10.00	25.00	6.00	512.00
29	2.00	0.10	0.60	1.00	1.00	6.00	512.00
30	2.00	0.10	0.60	1.00	25.00	6.00	512.00
31	2.00	0.10	0.60	10.00	1.00	6.00	512.00
32	2.00	0.10	0.60	10.00	25.00	6.00	512.00
33	0.25	0.02	0.60	3.30	1.00	0.10	512.00
34	0.25	0.02	0.60	3.30	1.00	10.00	512.00
35	0.25	0.02	0.60	3.30	25.00	0.10	512.00
36	0.25	0.02	0.60	3.30	25.00	10.00	512.00
37	0.25	0.50	0.60	3.30	1.00	0.10	512.00
38	0.25	0.50	0.60	3.30	1.00	10.00	512.00
39	0.25	0.50	0.60	3.30	25.00	0.10	512.00
40	0.25	0.50	0.60	3.30	25.00	10.00	512.00
41	0.10	0.10	0.40	3.30	5.00	0.10	512.00
42	0.10	0.10	0.40	3.30	5.00	10.00	512.00
43	0.10	0.10	0.80	3.30	5.00	0.10	512.00
44	0.10	0.10	0.80	3.30	5.00	10.00	512.00
45	2.00	0.10	0.40	3.30	5.00	0.10	512.00
46	2.00	0.10	0.40	3.30	5.00	10.00	512.00
47	2.00	0.10	0.80	3.30	5.00	0.10	512.00
48	2.00	0.10	0.80	3.30	5.00	10.00	512.00
49	0.25	0.10	0.60	3.30	5.00	6.00	512.00
50	0.25	0.10	0.60	3.30	5.00	6.00	512.00

51	0.25	0.10	0.60	3.30	5.00	6.00	512.00
52	0.25	0.10	0.60	3.30	5.00	6.00	512.00
53	0.25	0.10	0.60	3.30	5.00	6.00	512.00
54	0.25	0.10	0.60	3.30	5.00	6.00	512.00

Table D.3: Group values used in experimental design for dispersivity estimation. Each experiment is repeated 5 times with different realizations of reservoir heterogeneity.

Scaling groups	λ_{xD}	λ_{zD}	V_{DP}	N_D	M	R_L	N_{Pe}
1	0.25	0.10	0.60	0.09	5.00	0.10	100.00
2	0.25	0.10	0.60	1.32	5.00	10.00	100.00
3	0.25	0.10	0.60	9.95	5.00	0.10	100.00
4	0.25	0.10	0.60	10.03	5.00	10.00	100.00
5	0.25	0.10	0.60	0.28	5.00	0.10	1000.00
6	0.25	0.10	0.60	2.83	5.00	10.00	1000.00
7	0.25	0.10	0.60	9.95	5.00	0.10	1000.00
8	0.25	0.10	0.60	10.34	5.00	10.00	1000.00
9	0.10	0.10	0.60	2.03	1.00	0.10	500.00
10	0.10	0.10	0.60	1.90	25.00	0.10	500.00
11	0.10	0.10	0.60	3.12	1.00	10.00	500.00
12	0.10	0.10	0.60	3.36	25.00	10.00	500.00
13	2.00	0.10	0.60	2.01	1.00	0.10	500.00
14	2.00	0.10	0.60	2.06	25.00	0.10	500.00
15	2.00	0.10	0.60	2.14	1.00	10.00	500.00
16	2.00	0.10	0.60	2.40	25.00	10.00	500.00
17	0.25	0.02	0.60	1.52	1.00	6.00	500.00
18	0.25	0.02	0.60	1.95	25.00	6.00	500.00
19	0.25	0.02	0.60	10.08	1.00	6.00	500.00
20	0.25	0.02	0.60	10.09	25.00	6.00	500.00
21	0.25	0.50	0.60	1.55	1.00	6.00	500.00
22	0.25	0.50	0.60	1.83	25.00	6.00	500.00
23	0.25	0.50	0.60	10.08	1.00	6.00	500.00
24	0.25	0.50	0.60	10.09	25.00	6.00	500.00
25	0.10	0.02	0.60	2.37	5.00	6.00	100.00
26	0.10	0.02	0.60	3.41	5.00	6.00	1000.00
27	0.10	0.50	0.60	2.36	5.00	6.00	100.00
28	0.10	0.50	0.60	3.39	5.00	6.00	1000.00
29	2.00	0.02	0.60	2.05	5.00	6.00	100.00
30	2.00	0.02	0.60	2.35	5.00	6.00	1000.00
31	2.00	0.50	0.60	2.09	5.00	6.00	100.00
32	2.00	0.50	0.60	2.56	5.00	6.00	1000.00
33	0.25	0.10	0.40	2.09	1.00	6.00	100.00
34	0.25	0.10	0.40	2.07	25.00	6.00	100.00
35	0.25	0.10	0.40	2.58	1.00	6.00	1000.00
36	0.25	0.10	0.40	2.49	25.00	6.00	1000.00
37	0.25	0.10	0.80	2.72	1.00	6.00	100.00

38	0.25	0.10	0.80	3.20	25.00	6.00	100.00
39	0.25	0.10	0.80	4.03	1.00	6.00	1000.00
40	0.25	0.10	0.80	4.64	25.00	6.00	1000.00
41	0.10	0.10	0.40	1.67	5.00	6.00	500.00
42	0.10	0.10	0.40	10.09	5.00	6.00	500.00
43	0.10	0.10	0.80	2.52	5.00	6.00	500.00
44	0.10	0.10	0.80	9.99	5.00	6.00	500.00
45	2.00	0.10	0.40	1.40	5.00	6.00	500.00
46	2.00	0.10	0.40	10.07	5.00	6.00	500.00
47	2.00	0.10	0.80	1.80	5.00	6.00	500.00
48	2.00	0.10	0.80	10.09	5.00	6.00	500.00
49	0.25	0.02	0.40	2.04	5.00	0.10	500.00
50	0.25	0.02	0.40	2.20	5.00	10.00	500.00
51	0.25	0.02	0.80	1.93	5.00	0.10	500.00
52	0.25	0.02	0.80	4.10	5.00	10.00	500.00
53	0.25	0.50	0.40	1.76	5.00	0.10	500.00
54	0.25	0.50	0.40	2.49	5.00	10.00	500.00
55	0.25	0.50	0.80	2.03	5.00	0.10	500.00
56	0.25	0.50	0.80	3.77	5.00	10.00	500.00
57	0.25	0.10	0.60	2.64	5.00	6.00	500.00
58	0.25	0.10	0.60	2.64	5.00	6.00	500.00
59	0.25	0.10	0.60	2.64	5.00	6.00	500.00
60	0.25	0.10	0.60	2.64	5.00	6.00	500.00
61	0.25	0.10	0.60	2.64	5.00	6.00	500.00
62	0.25	0.10	0.60	2.64	5.00	6.00	500.00
63	0.25	0.10	0.60	2.55	1.00	6.00	500.00
64	0.25	0.10	0.60	2.82	25.00	6.00	500.00
65	0.25	0.10	0.60	1.73	5.00	6.00	500.00
66	0.25	0.10	0.60	10.09	5.00	6.00	500.00
67	0.25	0.10	0.60	2.01	5.00	0.10	500.00
68	0.25	0.10	0.60	2.92	5.00	10.00	500.00
69	0.25	0.10	0.60	3.08	5.00	6.00	1000.00
70	0.25	0.10	0.60	2.23	5.00	6.00	100.00
71	0.10	0.10	0.60	2.91	5.00	6.00	500.00
72	2.00	0.10	0.60	2.24	5.00	6.00	500.00
73	0.25	0.02	0.60	2.61	5.00	6.00	500.00
74	0.25	0.50	0.60	2.61	5.00	6.00	500.00
75	0.25	0.10	0.40	2.36	5.00	6.00	500.00
76	0.25	0.10	0.80	3.50	5.00	6.00	500.00
77	0.10	0.02	0.40	0.47	1.00	0.10	100.00
78	2.00	0.50	0.80	10.41	25.00	10.00	1000.00
79	2.00	0.50	0.40	0.88	1.00	0.10	100.00
80	2.00	0.50	0.80	1.03	1.00	10.00	100.00
81	0.10	0.02	0.40	1.46	5.00	0.10	1000.00
82	2.00	0.02	0.80	2.79	1.00	10.00	1000.00
83	2.00	0.50	0.60	2.00	1.00	0.10	100.00
84	0.25	0.02	0.40	10.01	1.00	10.00	100.00
85	0.10	0.02	0.60	0.30	5.00	0.10	100.00
86	0.10	0.50	0.80	10.06	1.00	10.00	100.00
87	0.31	0.09	0.71	4.79	8.27	3.44	616.45
88	1.20	0.41	0.65	1.87	14.17	5.06	612.55
89	0.85	0.21	0.50	6.28	6.56	3.74	465.36
90	1.29	0.14	0.52	6.70	8.90	2.73	742.38
91	0.48	0.22	0.76	7.51	4.44	0.35	608.84
92	1.01	0.20	0.61	2.75	17.15	4.69	542.60

93	1.13	0.25	0.69	6.22	14.80	2.93	447.04
94	0.80	0.42	0.57	4.13	11.08	6.25	497.56
95	0.42	0.26	0.58	5.35	13.47	7.35	661.46
96	0.87	0.37	0.54	4.06	16.56	4.54	467.76

Table D.4: Group values used as test for experimental design. Each experiment is repeated 5 times with different realizations of reservoir heterogeneity.

Scaling groups	λ_{xD}	λ_{zD}	V_{DP}	M	R_L
1	0.10	0.02	0.60	5.00	6.00
2	0.10	0.50	0.60	5.00	6.00
3	2.00	0.02	0.60	5.00	6.00
4	2.00	0.50	0.60	5.00	6.00
5	0.25	0.10	0.40	1.00	6.00
6	0.25	0.10	0.40	25.00	6.00
7	0.25	0.10	0.80	1.00	6.00
8	0.25	0.10	0.80	25.00	6.00
9	0.25	0.02	0.60	5.00	0.10
10	0.25	0.02	0.60	5.00	10.00
11	0.25	0.50	0.60	5.00	0.10
12	0.25	0.50	0.60	5.00	10.00
13	0.10	0.10	0.40	5.00	6.00
14	0.10	0.10	0.80	5.00	6.00
15	2.00	0.10	0.40	5.00	6.00
16	2.00	0.10	0.80	5.00	6.00
17	0.25	0.10	0.60	1.00	0.10
18	0.25	0.10	0.60	1.00	10.00
19	0.25	0.10	0.60	25.00	0.10
20	0.25	0.10	0.60	25.00	10.00
21	0.25	0.02	0.40	5.00	6.00
22	0.25	0.02	0.80	5.00	6.00
23	0.25	0.50	0.40	5.00	6.00
24	0.25	0.50	0.80	5.00	6.00
25	0.10	0.10	0.60	1.00	6.00
26	0.10	0.10	0.60	25.00	6.00
27	2.00	0.10	0.60	1.00	6.00
28	2.00	0.10	0.60	25.00	6.00
29	0.25	0.10	0.40	5.00	0.10
30	0.25	0.10	0.40	5.00	10.00
31	0.25	0.10	0.80	5.00	0.10
32	0.25	0.10	0.80	5.00	10.00
33	0.10	0.10	0.60	5.00	0.10
34	0.10	0.10	0.60	5.00	10.00
35	2.00	0.10	0.60	5.00	0.10
36	2.00	0.10	0.60	5.00	10.00
37	0.25	0.02	0.60	1.00	6.00
38	0.25	0.02	0.60	25.00	6.00
39	0.25	0.50	0.60	1.00	6.00
40	0.25	0.50	0.60	25.00	6.00
41	0.25	0.10	0.60	5.00	6.00
42	0.25	0.10	0.60	5.00	6.00

43	0.25	0.10	0.60	5.00	6.00
44	0.25	0.10	0.60	5.00	6.00
45	0.25	0.10	0.60	5.00	6.00
46	0.25	0.10	0.60	5.00	6.00
47	0.68	0.26	0.56	11.06	7.17
48	0.73	0.15	0.52	4.87	0.19
49	0.87	0.45	0.49	6.93	4.23
50	1.50	0.48	0.69	16.94	6.17
51	0.81	0.20	0.56	3.26	1.45
52	1.60	0.33	0.58	1.41	2.76
53	0.71	0.40	0.52	21.26	8.81
54	0.86	0.33	0.41	9.40	0.77
55	0.13	0.48	0.76	2.50	2.45
56	1.59	0.37	0.55	10.30	9.23
57	0.31	0.09	0.71	8.27	3.44
58	1.20	0.41	0.65	14.17	5.06
59	0.85	0.21	0.50	6.56	3.74
60	1.29	0.14	0.52	22.30	2.73
61	0.48	0.22	0.76	4.44	0.35
62	1.01	0.20	0.61	17.15	4.69
63	1.13	0.25	0.69	3.50	2.93
64	0.80	0.42	0.57	11.08	1.63
65	0.42	0.26	0.58	13.47	7.35
66	0.87	0.37	0.54	1.70	4.54

Table D.5: Group values used in experimental design for velocity anisotropy estimation. Each experiment is repeated 5 times with different realizations of reservoir heterogeneity. The last 20 rows are the group values that are used for validation test.

Appendix E: User Guide for FFTSim Program

The FFT (Fast Fourier Transform) simulator is a stochastic permeability field generator written by Dr. James Jennings (Jennings *et al.*, 2000). It is based on a spectral method, which represents a synthetic field with a Fourier series. Inputs to the FFTSim are the parameters of the permeability correlation model and the grid at which the output is desired. Outputs are a set of normally distributed numbers, which are conditioned to the correlation structure.

Input Parameters:

Table E.1 lists all the input parameters that are used in FFTSim program with a brief description of each parameter.

Correlation length in this code is modeled by the stable semivariogram model as

$$\gamma(h,r) = S\left[1-\exp\left(-\left(\frac{h}{r}\right)^{p}\right)\right] \tag{E.1}$$

where p is the asymptotic power law exponent and exponents of one and two produce the exponential and Gaussian semivariogram model, S is the sill and r is the range. The range parameter is the autocorrelation length used as an input to the model and is taken to be the lag at which 67% of the sill is reached.

Parameter	Description
Run type	Run type other than 1 produces no simulation, but rather a much bigger output file for plotting the covariance function, the power spectrum, and the amplitude spectrum.
Random number seed	The random number generator is built in and is machine portable. That means the same random number seed produces the same realization even when compiled on different computers.
Variogram window	Use zero. Non-zero values are for an expert user to try to damp covariance models with a Gaussian window in cases where the covariance would not otherwise decay enough within the grid.
X array size power, px	This is the power to base 2 for the number of gridblocks in the x-direction.
Y array size power, py	This is the power to base 2 for the number of gridblocks in the y-direction.
Z array size power, pz	This is the power to base 2 for the number of gridblocks in the z-direction.
X mesh spacing, dx	Size of x-directional gridblock
Y mesh spacing, dy	Size of y-directional gridblock
Z mesh spacing, dz	Size of z-directional gridblock
Number of variogram structures	A covariance model can be built from a sum of any number of structures.
Variogram type	1 = stable 2 = J-bessel 3 = K-bessel
Variogram sill	Total variance
Alpha	1 = exponential variogram 2 = Gaussian variogram
X scale	Correlation length (range) in x-direction
Y scale	Correlation length (range) in y-direction
Z scale	Correlation length (range) in z-direction

Table E.1: Description of input parameters for FFTSim program.

The input to the FFTSim program is a text file as given in Figure E.1. The comment lines list the input parameters name, which are described in Table E.1. The comment lines are not to be included in the input file.

```
1 1 0                  // run type, seed, window
5 2 3 1 1 1            // px, py, pz, dx, dy, dz
1                      // number of variogram structures
1 1 1 10.0  1.0  1.0   // variogram type, sill, alpha, x scale, y scale, z scale
```

Figure E.1: Sample input file for FFTSim program.

In this research we used run type 1 to generate the stochastic permeability field. The random number seed can be varied to generate multiple realizations. Same random number seed generate identical outputs. We used stable exponential variogram type with total variance of 1.0 and mean of zero. The number of grid-blocks in each direction is in terms of power to the base two. For example, the sample input file (Fig. E.1) would generate 5^2 x 2^2 x 3^2 i.e. 32 x 4 x 8 grid-blocks field.

Implementation of the Code:

The windows executable file fft_sim.exe can be used on a PC to generate the output using the following command:

```
Folder_name/fft_sim.exe<input_file_name>output_file_name
```

where the "*input_file_name*" is the text file that contain the parameters similar to the Figure E.1 without given comments, and "*output_ file_name*" is the output file that contain the generated random numbers. Figure E.2 shows the random numbers generated by using the given input file in Figure E.1. Generated random numbers are then processed to generate permeability field.

Data Processing:

The values are written to the output file in x, y, z, order, where x varies fastest and z varies last. The output has a mean of zero and the variance that is specified in the input as the sill. To convert output numbers to log-normal permeability distribution with a specified mean and variance, the following formula is used.

$$k(i,j,k) = Exp\left[\mu_{\ln k} + \sigma_{\ln k} \cdot N(i,j,k)\right] \ . \tag{E.2}$$

where, *k(i,j,k)* is the log-normally distributed permeability, $\mu_{\ln k}$ is the mean of the log of permeability, $\sigma_{\ln k}$ is the standard deviation of the log of permeability, *N(i,j,k)* is the output from FFTSim program.

```
nx = 32, ny = 4, nz = 8, dx = 1.000000, dy = 1.000000, dz = 1.000000, seed = 1, nvar = 1
1
simulation
 1.09987e+000
 5.06121e-001
-3.20826e-001
 2.61262e-001
 5.74937e-001
 1.29005e-001
 4.37051e-001
 1.46319e-001
 7.09333e-001
 8.23950e-001
 8.28377e-001
 1.13332e+000
 9.09254e-002
-3.18491e-001
 1.54355e-001
 2.53693e-001
 1.22459e-001
-5.08537e-002
 9.04405e-002
 2.45193e-001
 2.34692e-001
 4.86910e-001
.....
......
```

Figure E.2: Sample output file for FFTSim program generated by using the input file given in Figure E.1.

Post Processing Code:

Post-processing is required to convert the generated random numbers of FFTSim program to the permeability field. Figure E.3 presents a sample post processing code written in C++ that converts the output file from FFTSim into the permeability field. The comment lines (first 3 lines) of the FFTSim output are not to be included in the post-processing.

Figure E.4 shows the generated permeability data by using the random numbers given in Figure E.2 and code given in Figure E.3. The mean permeability of ***ln*** *k* is 5.3 and standard deviation of ***ln*** *k* is 0.92.

```
# include<fstream.h>
# include<math.h>
const int NX=32, NY=4, NZ=8;                    // no of grids
int SX=32, SY=4, SZ=8;                  //no of grids to be considered
double DX=1,DY=1,DZ=1;                          //length
double input[NX][NY][NZ],perm[NX][NY][NZ];
double lmean=5.3;                               //mean of ln k
double lsdev=0.92;                              // standard dev of ln perm (  Vdp=1-exp(-STDV(LnK))  )

int main()
{
        ifstream infile("output_file_name.txt",ios::in);
        ofstream outchar("perm-out.txt",ios::out);

        for( int a=0;a<NZ;a++) {
                for( int b=0;b<NY;b++) {
                        for( int c=0;c<NX;c++) {
                                infile>>input[c][b][a];
                                perm[c][b][a]=exp(lmean+lsdev*input[c][b][a]);
                                }
                        }
                }

        for(  a=0;a<SZ;a++) {
                for( int b=0;b<SY;b++) {
                        for( int c=0;c<SX;c++) {
                                outchar<<perm[c][b][a]<<"\n";
                                }
                        }
                }
        return(0);
}
```

Figure E.3: Sample post processing code written in C++ that converts the output file from FFTSim into the permeability field.

```
319.14
149.133
254.77
339.999
225.582
299.492
229.204
384.747
427.534
429.279
568.303
217.816
149.454
230.905
253.002
224.228
191.18
217.719
251.031
248.618
313.549
262.375
139.16
339.692
356.766
560.689
754.199
449.209
522.484
362.632
766.905
774.912
647.685
878.479
509.037
490.711
361.04
565.263
398.823
133.034
159.189
49.831
39.5961
.....
......
```

Figure E.4: Generated permeability data by using the random numbers given in Figure E.2 and code given in Figure E.3.

Appendix F: Single-Phase Permeability Upscaling Code

The following program, written in C++, is used to upscale permeability in a 2-D single-phase flow model. Input to the code is a text file that contains the fine-scale permeability field and the output is a text file that contains the upscaled permeability field. In the input data section the number of fine-scale grid-blocks, grid-block sizes and number of coarse-scale grid-block sizes are required.

```
//**************************************************************************************
//************************  Permeability Upscaling  ******************************************
//************************  Single-Phase, 2-D, No Gravity *************************************

#include<math.h>
#include<fstream.h>
#include<iostream.h>
#include<conio.h>
#include<stdlib.h>
#include <iomanip.h>
#include <stdio.h>
#include <time.h>
#include <malloc.h>

//************* Input Data ***************************************************************
const int nx=480;                        // no. of fine scale grid in x direction
const int ny=60;                         // no. of fine scale grid in y direction
const int Ix=15;                         // desired No of grid in x-direction (coarse grid)
const int Jy=6;                          // desired no. of grid in y-direction (coarse grid)
double Dx=0.25;                          //size of grid block in X direction
double Dy=0.25;                          //size of grid block in Y direction
double Dz=1;                             //size of grid block in Z direction

int Nx=int (nx/Ix);                       //X-direction upscaled grid size
int Ny=int (ny/Jy);                      //Z-direction upscaled grid size

const double P1=0.0;                     // dimensionless outlet pressure of coarse grid
const double P0=1.0* (1e5*Nx*Dx);    //  dimensionless (P_inlet=P0*L*E5) inlet pressure of coarse grid
const double Mio=1e-3;                   // viscosity  (pa.s)
double comp,sum,duration;

//************************** Variables Arrays ********************************************

double **a,**f,**l,**u,**Pt,*b,*P;
double **Txplus,**Tyminus,**Txminus,**Typlus;
double **kx,**ky,**Vx,**Vy,**V,**K_ef;

int I,J,II,JJ,i,j,k,n,n2,n3,t,mult,nx1,ny1,nx2,nx3,ny2,ny3;
```

```
//**************************** Subroutines and Functions ***********************************

void solver(double **a,double **u,double **l, double *b,int n,int N);              // solver subroutine
int min(int r,int s);

int max(int r,int s);
void Input();                                                                       // read input file
void Transmissibility();                                                            //calculate transmissibility
void flow_matrix();                                                                 // build flow matrix
void Flux();                                                                        // velocity values
void K_eff();                                                                       // effective perm


//**************** Printed out files *****************************************************
ofstream Kefff("Perm-upscale.txt",ios::out);                    // effective permeability output file
//**********************************************************************************

void main()
{

        n=Nx*Ny;
        n2=nx*ny;
        n3=Ix*Jy;
        nx1=Nx;
        ny1=Ny;
        nx2=nx;
         ny2=ny;
        nx3=Ix;
         ny3=Jy;


  //******************* Matrix Declaration ***********************************************
clock_t start, finish;
start = clock();

        b=new double [n+1];
        P=new double [n+1];
        a=new double *[n+1];
        f=new double *[n+1];
        l=new double *[n+1];
        u=new double *[n+1];
        Pt=new double *[nx1+2];
        Txplus=new double *[nx1+2];
        Txminus=new double *[nx1+2];
        Typlus=new double *[nx1+2];
        Tyminus=new double *[nx1+2];
        Vx=new double *[nx1+2];
        Vy=new double *[nx1+2];
        V=new double *[nx1+2];
        kx=new double *[nx2+2];
        ky=new double *[nx2+2];
        K_ef=new double *[nx3+2];

        for(i=0;i<=n;i++){
        a[i]=new double [n+1];
        f[i]=new double [n+1];
        l[i]=new double [n+1];
        u[i]=new double [n+1];
```

```
            }

            for(i=0;i<=nx+1;i++){
            Pt[i]=new double [ny1+2];
            Txplus[i]=new double [ny1+2];
            Txminus[i]=new double [ny1+2];
            Typlus[i]=new double [ny1+2];
            Tyminus[i]=new double [ny1+2];
            Vx[i]=new double [ny1+2];
            Vy[i]=new double [ny1+2];
            V[i]=new double [ny1+2];


                                    }

            for(i=0;i<=nx2+1;i++){
                        kx[i]=new double [ny2+2];
                        ky[i]=new double [ny2+2];
                        }

            for(i=0;i<=nx3+1;i++){
                        K_ef[i]=new double [ny3+2];
                        }
//*************************main ******************************************************

            t=1;
            for ( J=1;J<=Jy;J++){
                  for ( I=1;I<=Ix;I++){


                                    Input();
                                    Transmissibility();
                                    flow_matrix();
                                    Flux();
                                    K_eff();

                                    //          comp=  (t/(Ix*Jy));
                                                cout<<"Completed = "<<t<<endl;;
                                                t=t+1;

                        }
                                    }


  finish = clock();
  duration = (double)(finish - start) / CLOCKS_PER_SEC;
  printf( "CPU time= %2.1f seconds\n", duration );


}

//******************** end of main ******************************************************
void Input()
{

  ifstream Permx("Perm-fine.txt",ios::in);            // read input permeability file
```

```
                      for (j=1;j<=ny;j++)
       {
            for (i=1;i<=nx;i++)
            {
                  Permx>>kx[i][j];
                       kx[i][j]=9.869e-16*kx[i][j] ;
                                                  ky[i][j]=kx[i][j] ;

            }
       }

  //******************* Initializing matrices ************************************************

for(i=1;i<=n;i++)
                                {

                                b[i]=0;
                                P[i]=0;

                                }
 }

//************************* calculate transmisciblity****************************************

void Transmissibility()
{
            int ii;
            int jj;


             II=((I-1)*Nx);
             JJ=((J-1)*Ny);

            for (j=1;j<=Ny;j++)  {
                       for(i=1;i<=Nx;i++)  {
                                Txplus[i][j]=0;
                                Typlus[i][j]=0;
                                Txminus[i][j]=0;
                                Tyminus[i][j]=0;
                                           }
                                  }


            for (j=1;j<=Ny;j++)     {
                        for(i=1;i<=Nx;i++)    {

                                ii=II+i;
                                jj=JJ+j;
                                kx[II][jj]=1e36;
                                kx[II+Nx+1][jj]=1e36;
                                ky[ii][JJ]=1e36;
                                ky[ii][JJ+Ny+1]=1e36;
                                    }
                                          }


            for (j=1;j<=Ny;j++)   {
             for(i=1;i<=Nx;i++)   {
```

```
            ii=II+i;
             jj=JJ+j;
    Txplus[i][j]= ( 2 / ((1 /  (Dz*Dy*kx[ii][jj]/(Dx*Mio) )) + (1 / (Dz*Dy*kx[ii+1][jj]/(Dx*Mio)  ))  )   );
    Txminus[i][j]=( 2 / ((1 /  (Dz*Dy*kx[ii][jj]/(Dx*Mio) )) + (1 / (Dz*Dy*kx[ii-1][jj]/(Dx*Mio)  ))  )   );
    Typlus[i][j]= ( 2 / ((1 /  (Dz*Dx*ky[ii][jj]/(Dy*Mio) )) + (1 / (Dz*Dx*ky[ii][jj+1]/(Dy*Mio)  ))  )   );
    Tyminus[i][j]=( 2 / ((1 /  (Dz*Dx*ky[ii][jj]/(Dy*Mio) )) + (1 / (Dz*Dx*ky[ii][jj-1]/(Dy*Mio)  ))  )   );

            }
                }

}

//*************************** build flow matrix*********************************************
void flow_matrix()
{
    //********* a[ ][ ]***************** adjacency matrix

for(j=1;j<=n;j++)
        for(i=1;i<=n;i++)
            a[i][j]=0.0;

    j=1;
    for(i=1;i<=Nx;i++){
        k=Nx*(j-1)+i;
        a[k][k]=-(Txplus[i][j]+Txminus[i][j]+Typlus[i][j]);
            }

    for(j=2;j<Ny;j++)
        for(i=1;i<=Nx;i++){
            k=Nx*(j-1)+i;
            a[k][k]=-(Txplus[i][j]+Txminus[i][j]+Typlus[i][j]+Tyminus[i][j]);
                }
    j=Ny;
    for(i=1;i<=Nx;i++){
        k=Nx*(j-1)+i;
        a[k][k]=-(Txplus[i][j]+Txminus[i][j]+Tyminus[i][j]);
            }


    for(j=1;j<=Ny;j++)
        for(i=1;i<Nx;i++){
            k=Nx*(j-1)+i;
            a[k][k+1]=Txplus[i][j];
                }

for(j=1;j<=Ny;j++)
        for(i=2;i<=Nx;i++){
            k=Nx*(j-1)+i;
            a[k][k-1]=Txminus[i][j];
            }

    for(j=1;j<=Ny-1;j++)
        for(i=1;i<=Nx;i++){
            k=Nx*(j-1)+i;
            a[k][k+Nx]= Typlus[i][j];
                }

    for(j=2;j<=Ny;j++)
```

```
                for(i=1;i<=Nx;i++){
                        k=Nx*(j-1)+i;
                        a[k][k-Nx]=Tyminus[i][j];
                                }

//*********b[ ]********** Forcing function matrix ******************************************

        for(j=1;j<=Ny;j++)
                for(i=1;i<=Nx;i++){
                        k=Nx*(j-1)+i;
                        b[k]=(0.0);
                                }
        i=1;
        for(j=1;j<=Ny;j++)  {
                k=Nx*(j-1)+1;
                b[k]= -Txminus[i][j]*(P0);
                         }

        i=Nx;
        for(j=1;j<=Ny;j++)  {
                k=Nx*(j-1)+Nx;
                b[k]= -Txplus[i][j]*P1;
                        }
//********** call solver subroutine ************ ******************************************

        solver(a,u,l,b,n,Nx);
                for(j=1;j<=Ny;j++)
                        for(i=1;i<=Nx;i++)  {
                                k=Nx*(j-1)+i;
                                P[k]=b[k];
                                        }
 }
//********************** calculate fulx **********************************************

void Flux()
{

//********  Calculating Flux at each Gridblock *************
        for (j=1;j<=Ny;j++){
                for (i=1;i<=Nx;i++) {
                        k=Nx*(j-1)+i;
                        Pt[i][j]=P[k];
                                }
                        }

        for (j=1;j<=Ny;j++) {
                Pt[Nx+1][j]=P1;
                Pt[0][j]=P0;
                        }

        for (i=1;i<=Nx;i++) {
                Pt[i][Ny+1]=Pt[i][Ny];
                Pt[i][0]=Pt[i][1];
                        }

        for (j=1;j<=Ny;j++) {
                for (i=1;i<=Nx;i++) {
```

```
			Vx[i][j]=- (0.5)*(  Txplus[i][j]*(Pt[i+1][j]-Pt[i][j]) + Txminus[i][j]*(Pt[i][j]-Pt[i-1][j])
)/(Dz*Dy);							}
				}

		for (j=1;j<=Ny;j++) {
			for (i=1;i<=Nx;i++) {
			Vy[i][j]=- (0.5)*(  Typlus[i][j]*(Pt[i][j+1]-Pt[i][j]) + Tyminus[i][j]*(Pt[i][j]-Pt[i][j-1])
)/(Dz*Dx);
					}
				}
}

//************************ effective permeability ******************************************

void K_eff()
{

		double Keff=0;
		double Vt=0;
		double Vave=0;

		for (i=1;i<=Ny;i++) {
			Vt=Vt+(Vx[Nx][i])   ;
				}

		Vave=Vt/Ny;
		Keff=((1/9.869e-16)*(Vave*Mio*(Nx*Dx))/(P0-P1));
		Kefff<<Keff<<" \n";
}


//********************** subroutin Matrix solver *****************************************
void solver(double **a,double **u,double **l, double *b,int n,int N)
{
		int i,j,k,mi,mx;
		double zig,sig;
		 int p=N+1; int q=N+1;


//******* LU  decomposition ********************
		for(k=1;k<=n-1;k++){
			mi=min(k+p,n);
			for(i=k+1;i<=mi;i++)
				a[i][k]=a[i][k]/a[k][k];
				for(i=k+1;i<=mi;i++){
					mi=min(k+q,n);
					for(j=k+1;j<=mi;j++)
						a[i][j]=a[i][j]-a[i][k]*a[k][j];
						}
				}
for(i=1;i<=n;i++)
			for(j=1;j<=n;j++){
				l[i][j]=0.0;
				u[i][j]=0.0;
					}

		//******* matrix L[ ][ ] *********
```

```
for(i=1;i<=n;i++){
                for(j=1;j<i;j++)
                        l[i][j]=a[i][j];
                        }

        //******* matrix U[ ][ ]  *********
        for(i=1;i<=n;i++){
                for(j=i;j<=n;j++)
                        u[i][j]=a[i][j];
                        }

        //********* overwriting b[ ] for L[ ][ ] matrix  ************
for(i=1;i<=n;i++){
                mx=max(1,i-p);
                zig=0.0;
                for(j=mx;j<=i-1;j++)
                        zig=zig+l[i][j]*b[j];
                        b[i]=b[i]-zig;
                        }

        //****** solution matrix x[ ] for UX=Y ****************
for(i=n;i>=1;i--){
                mi=min(i+q,n);
                sig=0.0;
                for(j=i+1;j<=mi;j++)
                        sig=sig+u[i][j]*b[j];
                        b[i]=(b[i]-sig)/u[i][i];
                        }

}
//****************** min and max functions *************************************************

int min(int r,int s){
        int mini=0;
        mini=r;
        if(s<r) mini=s;
        return mini ;
}
 int max(int r,int s){
        int mxi=0;
        mxi=r;
        if(s>r) mxi=s;
        return mxi;
}
```

Appendix G: Post-Processing Dispersivity Estimation Code

The following program, written in Excel macro (VB), is used to read the solvent concentration history for all grid-blocks of a simulation model and then estimate local dispersivity for each grid-block.

Local dispersivities are estimated through use of constant velocity as the injection velocity in this research; however local dispersivities can be updated using local velocity of each grid-block. This can be done by including the local velocities from an input file to the code. Further detail can be found in the comments of the code.

```
Option Base 1

Sub Sheet_loop_mixzone()
Dim WrkSheet As Worksheet

For Each WrkSheet In Worksheets
  TheName = WrkSheet.Name

  If Left(TheName, 1) = "R" Then
    WrkSheet.Activate
    Call Main_Extractor_mixzone
    Sheet2_Col = Sheet2_Col + 1
    Col = 4
    Do
      If Cells(55, Col) = "" Then Exit Do
      Sheet2.Cells(6 + Col, Sheet2_Col + 2) = Cells(55, Col)
      Col = Col + 1
    Loop
  End If
Next

End Sub

Sub Main_Extractor_mixzone()

Dim C(520, 65, 42), V(520, 65, 1), Xd(200), Yd(200), CD(200), td(200), slope(200), alfa(200), Lx(200),
disx(200)
Dim alfa_ave, J16, J84 As Double
Dim xd16, xd84, CD_max, CD_min, n_max, n_min As Double
Dim j, t, nx, ny, nt, Dx, NLx, PVI, Num As Long
Dim ss, jvar As Long
Dim filename As String
```

```
Cells(1, 1) = "Nx"
Cells(2, 1) = "Ny"
Cells(3, 1) = "Nt"
Cells(4, 1) = "No of LX point"
Cells(4, 3) = "point"
Cells(5, 1) = "DX"
Cells(6, 1) = "PVI"
Cells(6, 3) = "Days"

nx = Cells(1, 2)    'Reservoir x-dimensions
ny = Cells(2, 2)    'Reservoir y-dimensions
nt = Cells(3, 2)    'No. of reported time steps
NLx = Cells(4, 2)   'No. of traveled distances to report dispersivities
Dx = Cells(5, 2)    'Grid-block size in x-direction
PVI = Cells(6, 2)   'Equivalent days of 1 PVI
filename_c = Cells(8, 2)    'Solvent concentration history file name
filename_v = Cells(9, 2)    'Local velocities file name

'*************Reading C(x,y,t)********************************
ThePath = "C:\Documents and Settings\Reza\....\"
TheFile = ThePath + filename_c
Dim AllData()
Open TheFile For Input As #1
Do While Not (EOF(1))
   LnNo = LnNo + 1
   Line Input #1, theline
   theline = Split(theline)
     For i = 0 To UBound(theline)
      If theline(0) = "'Global" Or theline(1) = "'day'" Then

      Else
            If theline(i) <> "" Then
               Nc = Nc + 1
               ReDim Preserve AllData(Nc)
               AllData(Nc) = theline(i)
            End If
     End If
   Next i

Loop
Close #1

'*************Reading V(x,y,tn)********************************
File = ThePath + filename_v
Dim velocity()
Open File For Input As #2
Do While Not (EOF(2))
   Line Input #2, Line
   Line = Split(Line)
   For i = 0 To UBound(Line)
      If Line(0) = "'Total" Or Line(1) = "'day'" Then
     Else
        If Line(i) <> "" Then
           Nv = Nv + 1
           ReDim Preserve velocity(Nv)
           velocity(Nv) = Line(i)
         End If
      End If
```

```
   Next i
Loop
Close #2

'****************************************************
'*** Read C(x,y,t) from 1D data file

For t = 1 To nt
   For j = 1 To ny
      For i = 1 To nx

          k = ((t - 1) * (nx * ny)) + (nx * (j - 1)) + i
          C(i, j, t) = AllData(k)
      Next i
   Next j
Next t

'****************************************************
'*** Read V(x,y,tn) from 1D data file
   For j = 1 To ny
      For i = 1 To nx
          k = (nx * (j - 1)) + i
          V(i, j, 1) = velocity(k)
      Next i
   Next j

'************************************************
'*** Read the x-Grid location fot transmission dispersivity
For i = 1 To NLx
   disx(i) = Cells(53, 3 + i)
   Lx(i) = Dx * disx(i)
   Cells(54, 3 + i) = Lx(i)
   Next i
'**************************************************
For ss = 1 To NLx
'*** Write C(x,y,t) and V(x,y,t) on spreadsheet cells
For t = 1 To nt
   For j = 1 To ny

          Cells(10 + t, 4 + j) = C(disx(ss), j, t)
   Next j
Next t

alfa_ave = 0
Num = 0
For jvar = 1 To ny
'**************************************************
'*** Dimenssionless time and CD
For i = 1 To nt
   Xd(i) = 0
   Yd(i) = 0
   '*** The following definition is used if velocity is assumed constant
   td(i) = (Cells(10 + i, 3) / PVI) * ((nx * Dx) / Lx(ss))

   '*** The following definition is used if local velocities are included
   'td(i) = V(disx(ss), jvar, 1) * cells(10 + i, 3) / Lx(ss) / 3.28 / 0.25
   Cells(10 + i, 4) = td(i)
   CD(i) = Cells(10 + i, 4 + jvar)  'C(disx(ss),j,i)
```

```
Next i

'*****************************************************

   CD_max = CD(nt)
   n_max = nt
For i = nt - 1 To 1 Step -1
   If CD(i) > CD_max Then
     CD_max = CD(i)
     n_max = i
   End If
Next i
'****************************
   CD_min = CD(1)
   n_min = 1
For i = 2 To nt
   If CD(i) < CD_min Then
     CD_min = CD(i)
     n_min = i
   End If
Next i
'******************************
'*** If CD(1)> 0.7 or CD_max<0.3 then do not estimate dispersivity for that grid-block
If CD(1) > 0.7 Or CD_max < 0.3 Then
      GoTo skip
End If
'******************************
'*** Lower Bound
For i = n_max To 1 Step -1
   If CD(i) < 0.16 Then
          J16 = ((1 - td(i)) / (td(i)) ^ 0.5)
          xd16 = -WorksheetFunction.NormSInv(CD(i)) / (2 ^ 0.5)
          GoTo UpperBound
   ElseIf i = 1 Then
          J16 = ((1 - td(i)) / (td(i)) ^ 0.5)
          xd16 = -WorksheetFunction.NormSInv(CD(i)) / (2 ^ 0.5)
           GoTo UpperBound
  End If
Next i

'******************************
UpperBound:
For i = 1 To n_max
   If CD(i) > 0.84 Then
         If CD(i) = 1 Then
          J84 = ((1 - td(i)) / (td(i)) ^ 0.5)
          xd84 = -3.09
          GoTo Disp_Estimate
         Else
            J84 = ((1 - td(i)) / (td(i)) ^ 0.5)
            xd84 = -WorksheetFunction.NormSInv(CD(i)) / (2 ^ 0.5)
            GoTo Disp_Estimate
         End If
  ElseIf i = n_max Then
         J84 = ((1 - td(i)) / (td(i)) ^ 0.5)
         xd84 = -WorksheetFunction.NormSInv(CD(i)) / (2 ^ 0.5)
         GoTo Disp_Estimate
   End If
```

```
Next i
'******************************
Disp_Estimate:

   coef_xd = 2 * (xd16 - xd84)
   alfa(jvar) = Lx(ss) * ((J84 - J16) / coef_xd) ^ 2

'****************************************************
'*** Write dispersivities value on spreadsheet cells

Cells(55 + jvar, 3 + ss) = alfa(jvar)
Cells(55 + jvar, 3) = jvar
alfa_ave = alfa_ave + alfa(jvar)
Num = Num + 1

'******************************
skip:
Next jvar
Cells(55, 3 + ss) = alfa_ave / Num
Next ss

End Sub
```

Appendix H: Sample GEM Input Files

The following input files are sample input files for FCM and MCM floods. FCM sample input file is a two components tracer flood and both components are non-hydrocarbon component.

```
*****************************************************************************************
**                                                                                     **
** FILE:   Box-Design.DAT                                                              **
**                                                                                     **
** MODEL:  512x64x1 GRIDS                                                              **
**                                Field UNIT                                           **
*****************************************************************************************
**                                                                                     **
** This is a cartesian 512x64x1 grids model                                            **
** single phase tracer test with dispersivity                                          **
**                                                                                     **
*****************************************************************************************
** CONTACT:   CMG,   (403)531-1300;   282-6495 (fax);support@cmgl.ca                   **
**                                                                                     **
*****************************************************************************************

RESULTS SIMULATOR IMEX

*****************************************************************************************
** I/O Control Section                                                                  **
*****************************************************************************************

**FILENAMES         *INDEX-IN              'file name'


*INUNIT *Field             **  units are used for both input and output.

*WPRN *WELL 0                    **TIME
*WPRN *GRID 0                    **TIME                    **write well result everey  time step


DIM *MDIMPL 100              **FRACTION OF GRID BLOCK IN FULLY IMPICIT MANER
DIM *MDICLU 200000           **MAXIMUM NUMBER OF NON-ZERO VALUES ENTERED FOR L & U IN AIMSOL


*OUTPRN *WELL   *Brief                    **ALL
*OUTPRN *RES    *None                     **ALL
*OUTPRN *GRID   *None                     ** *PRES *SO


*WSRF   *GRID   *Time
*WSRF   *WELL   *Time

**RESTART                   **write restart file WITH TIME STEP

*OUTSRF *WELL    *ZWEL 'SOL' 'PROx'
*OUTSRF *GRID  *SO *PRES *Z 'SOL'
```

```
           *VELOCRC  *VISO

*OUTSRF *RES   *ALL

*SUMMARY

*****************************************************************************************
** Reservoir Description Section
*****************************************************************************************
GRID CART  512  64  1
KDIR DOWN

DI CON 1.0

DJ CON 1.0

DK CON 10.00

DEPTH TOP 1 1 1 0.0

POR *CON       0.25

*PERMI                    *CON 100              **md
**INCLUDE permx.txt

*PERMJ *EQUALSI * 1.0
*PERMK *EQUALSI * 1.0


CPOR  MATRIX   0.E-10
PRPOR MATRIX   14.7

*****************************************************************************************
** FLUID PROPERTIES
*****************************************************************************************
*MODEL *PR
*NC   2  2

*COMPNAME     'OIL'    'SOL'

  *SG         1.0      1.0
  *TB         212.0    212.0       **deeg F
  *PCRIT      220.0    220.0       **atm
  *TCRIT      650.0    650.0       **k
  *VCRIT      0.055    0.055       **m3/kmole
  *MW         18.01    18.01

  *VISCOSITY  1.0       1.0
  **PCHOR     41.00    41.00
  *AC         0.04     0.04

  *HCFLAG    0        0      **USER COMPONENT IS NOT A HYDROCARBON COMP.

  *OMEGA    0.45   0.45
  *OMEGB    0.077  0.077

*PHASEID *OIL      ** ALL SINGLE PHASE GRID BLOCK IDENTIFY BY OIL

*TRES   60.0      **deg F

*PSAT   -1        **Psi

**WATER PROPERTY
*CW      0.0E-6   ** /kpa-1
```

```
*DENW    62.4      ** Lbm/ft3
*VISW    1.00      ** cp
*REFPW   14.7      ** Psi


*ROCKFLUID
******************************************************************************************
** Rock-Fluid Property Section
******************************************************************************************

**SIGMA         *CAPILLARY AND REL. PERM DEPENDENT ON INTERFACIAL TENSIN

*RPT 1   **NTENA


*SWT      **SNORM    KRW    NKRWO  NPCWOD
               0.00      0.00     1.00   0.0
        1.00      1.00     0.000  0.0


*SGT  **SL   KRG     KROG   PCGOD
             0.00          0.00          1.00          0.0
             1.00          1.00          0.00    0.0

*RTYPE  *CON 1

*DISPERARRAY-LNG     *CON     0.0          **ft
*DISPERARRAY-TRN     *CON     0.0
**DISPERARRAY-ISO    *CON     0.0

*INITIAL
******************************************************************************************
** Initial Conditions Section
******************************************************************************************
**USER_INPUT

*VERTICAL *off
  *PRES    *CON 4500.0    ** initial reservoir pressure
*SW      *CON  0.00
*ZGLOBAL *CON
1.0            0.00

******************************************************************************************
** Numerical Control Section
******************************************************************************************
*NUMERICAL

*NORM *PRESS 1000.0
*NORM *SATUR  0.2500
*NORM *GMOLAR 0.2500

**PRECC 0.0005      ** Convergence tolerance for linear solver default=0.0005
                             ** CONVERGE    ****PRESS, HC, WATER, MAXRES

*CONVERGE  *MAXRES  *NORMAL          *** LOOSER, LOOSE, NORMAL, TIGHT, TIGHTER
**CONVERGE  *PRESS   0.25
**CONVERGE  *WATER   0.01
**CONVERGE  *HC      0.01

*NEWTONCYC 30   ***Default value is 10
*SDEGREE 3
*SORDER *NATURAL
**PIVOT  *OFF      ***Control the diagonal submatrix pivot stabilization, default is OFF

**SOLVER **PARASOL    **/AIMSOL
```

```
*****************************************************************************************
** Well and Recurrent Data Section
*****************************************************************************************
*RUN

*DATE 2000 1 1
*DTWELL 1.0E-5
*DTMAX 1.0E-1
*DTMIN 1E-5
*AIMSET *CON  3                    ** 0=explicit  1=implicit   2=explicity always  3=impicit always

*****************************************************************************************

*WELL 1 'INJX'

   *INJECTOR  1
   *INCOMP  *SOLVENT     0.0  1.0
   **OPERATE  *MAX  *BHP 5012.00 *CONT
   *OPERATE  *MAX  *STG  200.0  *CONT
   *GEOMETRY *J 0.1 0.35 1.0 0.0
   *PERF *GEO 1
   ** if     jf     kf     wi
     1:1     1:64    1:1   1.0  *OPEN


*WELL 2  'PROx'
   *PRODUCER   2            ** Define the type of well 1.
   **OPERATE   *MAX  *STL  20.0  *CONT
   *OPERATE  *MIN  *BHP 4500.0 *CONT
   *GEOMETRY *J 0.15 0.35 1.0 0.0
   *PERF *GEO 2
   ** if     jf     kf     wi
    512:512  1:64    1:1    1.0     *OPEN


******************************************************************************************

*TIME      40
*TIME      80
*TIME      120
*TIME      160
*TIME      200
*TIME      240
*TIME      280
*TIME      320
*TIME      360
*TIME      400
*TIME      440
*TIME      480
*TIME      520
*TIME      560
*TIME      600
*TIME      640
*TIME      680
*TIME      720
*TIME      760
*TIME      800

*STOP
```

Figure G.1: Sample GEM input file for FCM tracer test.

```
***************************************************************************************** **
** MODEL: multiphase WAG injection                                                                                **
**       single POROSITY                                                                                         **
**       FIELD  UNITS                                                                                             **
**------------------------------------------------------------------
** three phase oil-gas-water
**------------------------------------------------------------------
** CONTACT CMG at (403)531-1300 or support@cmgl.ca
**------------------------------------------------------------------
************************************************************************
** I/O Control Section
************************************************************************

**FILENAMES         *INDEX-IN              'file-name'

*RESULTS *SIMULATOR *GEM

*INUNIT *FIELD

*WPRN *WELL *TIME
*WPRN *GRID *TIME                **write well result everey  time changes

*WRST *TIME
**RESTART  21                  **write restart file WITH TIME STEP

DIM *MDIMPL 100               **FRACTION OF GRID BLOCK IN FULLY IMPICIT MANER
DIM *MDICLU 200000            **MAXIMUM NUMBER OF NON-ZERO VALUES ENTERED FOR L & U IN AIMSOL

*OUTPRN *WELL   *ALL           **WHAT INFORMATION IS WRITTEN TO OUTPUTPRINT FILE
*OUTPRN *RES    *ALL
**OUTPRN *TABLES *NONE
*OUTPRN *GRID  *PRES *SO *SG *SW

*WSRF *WELL *TIME            **how frequency written to simulation result
*WSRF *GRID *TIME
*DIARY *CHANGES


*OUTSRF *WELL
            *PAVG
                          *ZWEL  'CO2'          'PRO1'
                          *ZWEL  'C2'           'PRO1'
                          *TOIP
                          *TGIP
                          *TWIP
                          *RECO
                          *RECI
                          *RECG


*OUTSRF *GRID  *PRES *SO *SG *SW *VISO *VISG  *VELOCRC *Z 'CO2'  *Z 'C2'
                 *DENO *DENG *DENW *SATP *SIG
                 *STRMLN

 *OUTSRF *RES   *ALL
*SUMMARY

**************************************************************************
** Reservoir Description Section
*********************************68***************************************

*GRID *CART 512 64 1

*KDIR *DOWN
```

```
*DI *CON 1.0
*DJ *CON 1.0
*DK *CON 10.00


*DEPTH 1 1 1 100.000       ** Depth to center of first block, in bottom layer.
*POR  *CON 0.25
*CPOR  3.60E-6          **ROCK COMPRESIBILITY
*PRPOR 4500.0           **REFRENCE PRESSURE
*DCPOR 0.0             **PRESSURE DEPNDENCY

*PERMI                 *CON 100             **md
**INCLUDE perm-B-random.txt

*PERMJ *EQUALSI * 1.0
*PERMK *EQUALSI * 1.0

****************************************************************************
** FLUID PROPERTIES
****************************************************************************

*MODEL    *PR
*NC      12 12
*COMPNAME 'CO2' 'C1' 'C2' 'C3' 'C4' 'C5' 'C6-C7' 'C8-C10' 'C11-C14' 'C15-C19' 'C20-C29' 'C30+'
*BIN
0.000
0.115      0.000
0.125      0.002      0.000
0.125      0.006      0.001      0.000
0.125      0.010      0.004      0.001      0.000
0.125      0.015      0.007      0.002      0.001      0.000
0.125      0.021      0.010      0.005      0.002      0.000      0.000
0.125      0.028      0.016      0.008      0.004      0.002      0.000      0.000
0.125      0.042      0.027      0.176      0.012      0.007      0.000      0.000      0.000
0.125      0.056      0.039      0.027      0.020      0.014      0.000      0.000      0.000      0.000
0.143      0.078      0.056      0.040      0.030      0.022      0.018      0.001      0.003      -0.046     0.000

*HCFLAG   0        0          0          0          0          0          0          0          0          0          0
          0
*PCRIT    72.95    45.46      48.18      41.95      37.49      33.26      31.23      27.78      20.78      16.92      15.47
          11.48
*VCRIT    0.09     0.10       0.15       0.20       0.25       0.31       0.38       0.46       0.68       0.98       1.36
          2.44
*TCRIT    304.2    190.6      305.4      369.8      425.2      469.7      542.2      604.4      679.4      751.9      810.2
          927.9
*AC      0.23      0.01       0.10       0.15       0.20       0.25       0.27       0.33       0.49       0.64       0.79
          1.05
*MW      44.0      16.0       30.1       44.1       58.1       72.2       94.2       116.0      169.5      232.6      328.0
          628.0
*VISVC     0.09    0.10       0.15       0.20       0.25       0.31       0.38       0.46       0.68       0.98       1.36
          2.44

*PHASEID  *DEN

**WATER PROPERTY
*CW      3.6E-06
*DENW     62.40        ** lb/ft3
*VISW    0.340         ** cp
*REFPW    4500.0       ** psi
*TRES   182.0     **deg F

**FLASH-METHOD                          **default

*******************************************************************************
```

```
**  ROCK/FLUID PROPERTIES
****************************************************************************************************

*ROCKFLUID

**SIGMA         *CAPILLARY AND REL. PERM DEPENDENT ON INTERFACIAL TENSION

*RPT 1   **


*SWT
**SNORM   KRW   KROW   PCWOD
0.320     0.000     0.630     0.000
0.343     0.001     0.548     0.000
0.389     0.003     0.407     0.000
0.412     0.006     0.348     0.000
0.458     0.014     0.247     0.000
0.493     0.024     0.186     0.000
0.539     0.048     0.122     0.000
0.562     0.066     0.097     0.000
0.608     0.115     0.057     0.000
0.631     0.148     0.043     0.000
0.654     0.187     0.031     0.000
0.677     0.231     0.021     0.000
0.701     0.281     0.014     0.000
0.724     0.335     0.009     0.000
0.747     0.394     0.005     0.000
0.770     0.456     0.003     0.000
0.793     0.519     0.001     0.000
0.816     0.583     0.000     0.000
0.839     0.646     0.000     0.000
0.862     0.708     0.000     0.000
0.874     0.737     0.000     0.000


*SGT
**SG     KRG     KROG    PCGOD
0.000     0.000     0.630     0.000
0.055     0.000     0.347     0.000
0.107     0.004     0.189     0.000
0.158     0.012     0.097     0.000
0.210     0.029     0.047     0.000
0.262     0.053     0.021     0.000
0.313     0.088     0.008     0.000
0.365     0.131     0.003     0.000
0.391     0.157     0.002     0.000
0.417     0.184     0.001     0.000
0.442     0.214     0.000     0.000
0.468     0.246     0.000     0.000
0.494     0.280     0.000     0.000
0.520     0.316     0.000     0.000
0.546     0.354     0.000     0.000
0.572     0.393     0.000     0.000
0.597     0.434     0.000     0.000
0.623     0.476     0.000     0.000
0.649     0.519     0.000     0.000

*HYSKRG  0.15


*RTYPE  *CON 1

**DISPERARRAY-LNG    *CON    0.000          **ft
**DISPERARRAY-TRN    *CON    0.000
**DISPERARRAY-ISO    *CON    0.000
```

```
*******************************************************************************
**  INITIAL CONDITIONS
**********210******************************************************************

*INITIAL

*VERTICAL *off
*PRES    *CON 4500.0    ** initial reservoir pressure
*SW      *CON  0.320

*ZGLOBAL *CON
0.015       0.5069      0.0587      0.0358      0.0192      0.0161      0.0379      0.0725      0.0639      0.0614      0.0639
            0.0487

**DWOC 500.   ** WOC
**DATUMDEPTH  100.0  *INITIAL
**SEPARATOR  1000.0  60.0
**BO
**BG
**RS

*******************************************************************************
**  NUMERICAL CONTROL
*******239*********************************************************************

 *NUMERICAL   ** Simulator uses default timestep size control based
          ** on number of Newtonian iterations


*DTMAX 0.02
*DTMIN 1E-8
*ITERMAX 50

*NORM *PRESS 10000.0
*NORM *SATUR  0.2500
*NORM *GMOLAR 0.2500

*PRECC 0.005      ** Convergence tolerance for linear solver default=0.0005
                           ** CONVERGE    ****PRESS, HC, WATER, MAXRES

*CONVERGE  *MAXRES  *NORMAL         *** LOOSER, LOOSE, NORMAL, TIGHT, TIGHTER
**CONVERGE  *PRESS   2.5
**CONVERGE  *WATER   0.02
**CONVERGE  *HC      0.02

*NEWTONCYC 30   ***Default value is 10

*SDEGREE 3
*SORDER *NATURAL
**PIVOT  *OFF      ***Control the diagonal submatrix pivot stabilization, default is OFF
**SOLVER **PARASOL    **/AIMSOL

*******************************************************************************
**  WELL DATA
******263**********************************************************************


*RUN

*DATE  2000 1  1
*DTWELL 1E-5         ** the first time step
*AIMSET *CON 3         **ASIGN EXPLICIT OR IMPLICIT 0=EXP  1=IMP

 *WELL 1  'PRO1'
```

```
  *PRODUCER 1               ** Define the type of well 1.
                  **OPERATE   *MAX  *STO  5000.0  *CONT    **STB/D
   *OPERATE  *MIN  *BHP 4500.0 *CONT
   *GEOMETRY *J 0.5 0.35 1.0 0.0
   *PERF *GEO 1
  ** if     jf     kf    wi
    512:512  1:64     1:1    1.0     *OPEN


*WELL 2 'INJ-Water'

  *INJECTOR 2
   *INCOMP  *WATER
   *OPERATE  *MAX      *STW 100.0        *CONT       **STB/D       ****BHP 5012.0
   *GEOMETRY *J 0.5 0.35 1.0 0.0         ** (rad  geofac  wfrac skin)
   *PERF *GEO 2
  ** if     jf     kf    wi
    1:1     1:64    1:1   1.0  *OPEN

*WELL 3 'INJ-Gas'

  *INJECTOR 3                                  ** 65% Enrichment
   *INCOMP  *SOLVENT    0.1663            0.4707      0.155        0.1743      0.0337      0            0            0            0
             0              0             0
   *OPERATE  *MAX  *STG 160000.0     *CONT      **SCF/D   **BHP 5012.0
   *GEOMETRY *J 0.5 0.35 1.0 0.0         ** (rad  geofac  wfrac skin)
   *PERF *GEO 3
  ** if     jf     kf    wi
     1:1     1:64    1:1   1.0  *OPEN


*SHUTIN 2
*OPEN 3

*TIME      20
*TIME      40
*TIME      60
*TIME      80
*TIME      100
*TIME      120
*TIME      140
*TIME      160
*TIME      180
*TIME      200
*TIME      220
*TIME      240
*TIME      260
*TIME      280
*TIME      300

 *STOP
```

Figure G.: Sample GEM input file for MCM flood.

References

Aris, R. 1959. Dispersion of a Solute by Diffusion, Convection, and Exchange Between Phases. *Proc. Roy. Soc.* London **A**252: 38-50.

Aronofsky, J.W. and Heller, J.P. 1957. Diffusion Model to Explain Mixing of Flowing Miscible Fluids in Porous Media. *Trans.,* AIME, 210: 345–349.

Arya, A., Hewett, T.A., Larson, R.G. and Lake, L.W. 1988. Dispersion and Reservoir Heterogeneity. *SPERE* **3** (1): 139–148. SPE-14364-PA.

Auriault, J.L., and Adler, P.M. 1995. Taylor Dispersion in Porous Media: Analysis by Multiple Scale Expansions. *Advances in Water Resources* **18** (4): 217-226.

Baker, L.E. 1977. Effects of Dispersion and Dead-End Pore Volume in Miscible Flooding. *SPEJ* **17**(3): 219-227. SPE-5632-PA.

Barker, J.W. and Fayers, F.J. 1994. Transport Coefficients for Compositional Simulation with Coarse Grids in Heterogeneous Media. *SPE Advanced Technology Series* ***2***: 103-112.

Bear, J. 1961. Some Experiments in Dispersion. *Jour. Geophysics.* Res. **66**: 2455-2467.

Bear, J. 1969. *Flow through Porous Media.* Academic Press, New York.

Bear, J. 1972. *Dynamics of Fluids in Porous Media*. New York City: American Elsevier Publishing Co.

Bear, J. 1979. *Hydrodynamics of Groundwater*. New York City: McGraw-Hill Co.

Bear, J. and Bachmat, Y. 1990. *Introduction to Modeling of Transport Phenomena in Porous Media*. Boston: Kluwer Academic Publishers.

Benson, D.A., Wheatcraft, S.W. and Meerschaert, M.M. 2000. Application of a Fractional Advection-Dispersion Equation. *Water Resources Research* **36** (6): 1403-1412.

Berentsen, C.W.J., Van Kruijsdijk, C.P.J.W. and Verlaan, M.L. 2007. Upscaling, Relaxation and Reversibility of Dispersive Flow in Stratified Porous Media. *Transport in Porous Media* **68** (2): 187-218.

Berentsen, C.W.J., Verlaan, M.L. and van Kruijsdijk, C.P.J.W. 2005. Upscaling and Reversibility of Taylor Dispersion in Heterogeneous Porous Media. *Physical Review E, Statistical, Nonlinear and Soft Matter Physics* **71** (4): 046308

Berkowitz, B. and Scher, H. 1995. On Characterization of Anomalous Dispersion in Porous and Fracture Media. *Water Resources Research* **31** (6): 1461–1466.

Berkowitz, B., Klafter, J., Metzler, R. and Scher, J. 2002. Physical Pictures of Transport in Heterogeneous Media: Advection-Dispersion, Random-Walk, and Fractional Derivative Formulations. *Water Resources Research* **38** (10): 1191-1203.

Berkowitz, B., Scher, H. and Silliman, S. E. 2000. Anomalous Transport in Laboratory-Scale, Heterogeneous Porous Media. *Water Resources Research* **36** (1): 149-158.

Bijeljic, B. and Blunt, M.J. 2006. Pore-Scale Modeling and Continuous Time Random Walk Analysis of Dispersion in Porous Media. *Water Resources Research* **42** (1): 1-5.

Bijeljic, B. and Blunt, M.J. 2007. Pore-Scale Modeling of Transverse Dispersion in Porous Media. *Water Resources Research* **43** (11): 2–8.

Bijeljic, B., Muggeridge, A.H. and Blunt, M.J. 2004. Pore-scale Modeling of Longitudinal Dispersion. *Water Resources Research* **40** (11): W03503.

Boving, T.B. and Grathwohl, P. 2001. Tracer Diffusion Coefficients in Sedimentary Rocks: Correlation to Porosity and Hydraulic Conductivity. *Journal of Contaminant Hydrology* **53** (1): 85-100.

Chang, H.I., Lo, T.S. and Ring, W.W. 1993. The Effects of Injectant-Enrichment Level on Oil recovery in Horizontal, Gravity-Tongue Dominated Enriched Gas Drives. Paper SPE 26084 presented at the western regional meeting, Anchorage, Alaska.

Chen, Y. and Durlofsky, L.J. 2006. Adaptive Local-Global Upscaling for General Flow Scenarios in Heterogeneous Formations. *Transport in Porous Media* **62** (2): 157-185.

Chen, Y. and Durlofsky, L.J. 2008. Ensemble-level upscaling for efficient estimation of fine-scale production statistics. *SPEJ* **13** (4): 400-411.

Chen, Y., Durlofsky, L.J., Gerritsen, M. and Wen, X.H. 2003. A Coupled Local-Global Upscaling Approach for Simulating Flow in Highly Heterogeneous Formations. *Advances in Water Resources* **26** (10): 1041-1060.

Cirpka, O.A. and Kitanidis, P.K. 2000. Characterization of Mixing and Dilution in Heterogeneous Aquifers by Means of Local Temporal Moments. *Water Resources Research* **36** (5): 1221–1236.

Cleary, R.W. and Ungs, M.J. 1978. Groundwater Pollutions and Hydrology, Mathematical Models and Computer Programs. Report 78-WR-15, Water Resource Program, Princeton University, Princeton, New Jersey.

Coats, K.H., Whitson and Thomas, L.K. 2009. Modeling Conformance as Dispersion. *SPEREE* **12** (1): 33-47. SPE 90390-PA.

COMSOL 3.2 Chemical Engineering Module: User's Guide. 2006. Burlington, Massachusetts: COMSOL.

Cortis, A., Gallo, C., Scher, H. and Berkowitz, B. 2004. Numerical simulation of non-Fickian transport in geological formations with multiple-scale heterogeneities. *Water Resources Research* **40 (3)**: W04209.

da Silva F. and Belery, P. 1989. Molecular Diffusion in Naturally Fractured Reservoirs: A Decisive Recovery Mechanism. Paper SPE 19672 presented at the Annual Technical Conference and Exhibition, San Antonio, TX.

Dagan, G. 1994. Upscaling of Dispersion Coefficients in Transport through Heterogeneous Porous Formations. In: A. Peters *et al.*, Editors, *Computational Methods in Water Resources X*, Kluwer Academic Publisher, Netherlands. 431-439.

Dagan, G. 1984. Solute Transport in Heterogeneous Porous Formations. *Journal of Fluid Mechanics* **145**: 151-177.

Darman, N.H., Durlofsky, L.J., Sorbie, K.S., Pickup, G.E. 2001. Upscaling immiscible gas displacements: Quantitative use of fine-grid flow data in grid-coarsening schemes. *SPE J* **6** (1): 47-56.

Dentz, M. and Carrera, J. 2007. Mixing and Spreading in Stratified Flow. *Physics of Fluids* **19** (1): 017107

Dentz, M., Cortis, A., Scher, H., and Berkowitz, B. 2004. Time behavior of solute transport in heterogeneous media: Transition from anomalous to normal transport. *Advances in Water Resources* 27 (2): 155–173.

Deutsch, C.V. 2002. *Geostatistical Reservoir Modeling*. New York: Oxford University Press.

Domenico, P.A. and Robbins, G. A. 1984. A Dispersion Scale Effect in Model Calibrations and Field Tracer Experiments. *Journal of Hydrology* **70**: 123-132.

Durlofsky, L.J. 1991. Numerical calculation of Equivalent Grid Block Permeability Tensors for Heterogeneous Porous Media. *Water Resources Research* **27** (5):699-708.

Durlofsky, L.J. 1992. Representation of Grid Block Permeability in Coarse Scale Models of Randomly Heterogeneous Porous Media. *Water Resources Research* **28** (7):1791-1800.

Durlofsky, L.J., Jones, R.C., and Milliken, W.J. 1997. A Non-uniform Coarsening Approach for the Scale-up of Displacement Processes in Heterogeneous Porous Media. *Advance in Water Resources* **20** (5-6):335-347.

Dykstra, H. and Parsons, R.L. 1950. *The Prediction of Oil Recovery by Waterflooding in secondary Recovery of Oil in the United States*. Second edition, 160–174. Washington, DC: API.

Fanchi, J.R. 1983. Multidimentional Numerical Dispersion. *SPEJ* **23**(1):143-151. SPE-9018-PA.

Fayers, F.J. and Lee, S.T. 1994. Crossflow Mechanisms in Oil Displacement by Gas Drive in Heterogeneous Reservoirs. *In Situ* **18** (4): 1-13.

Fick, A.E. 1855. Uber Diffusion. *Pogg. Ann.* **94**:59.

Fiori, A. 2001. On the Influence of Local-Dispersion in Solute Transport Through Formation with Evolving Scale of Heterogeneity. *Water Resources Research* **37** (2): 235-242.

Freeze, R. and Cherry, J. 1979. *Groundwater*. Prentice Hall, Englewood Cliffs, New Jersey.

Gaganisa, P., Skourasa, E.D., Theodoropouloub, M.A., Tsakirogloua, C.D., and Burganos, V.N. 2005. On the evaluation of dispersion next term coefficients from visualization experiments in artificial porous media. *Journal of Hydrology* **307** (1–4): 79–91.

Garmeh, G. and Johns, R.T. 2009. Upscaling of Miscible Floods in Heterogeneous Reservoirs Considering Reservoir Mixing. Paper SPE 124000 presented at the SPE Annual Technical Conference and Exhibition, New Orleans, LA.

Garmeh, G., Johns, R.T. and Lake, L.W. 2009. Pore-scale Simulation of Dispersion in Porous Media. *SPEJ* **14**(4). SPE-110228-PA.

Gelhar, L.W. 1993. *Stochastic Subsurface Hydrology*. New Jersey: Prentice Hall, Englewood Cliffs.

Gelhar, L.W. and Axness, C.L. 1983. Three Dimensional Stochastic Analysis of Macro-Dispersion in Aquifers. *Water Resources Research* **19** (1): 161–180.

Gelhar, L.W., Welty, C. and Rehfeldt, L.R. 1992. A Critical Review of Data on Field-Scale Dispersion in Aquifers. *Water Resource Research* **28** (7):1955-1974.

Gharbi, R., Peters, E.J. and Elkamel A. 1998. Scaling Miscible Fluid Displacements in Porous Media. *Energy & Fuels* **12**:801-811.

Ghomian, Y. 2008. Reservoir Simulation Studies for Coupled Co_2 Sequestration and Enhanced Oil Recovery. PhD dissertation, University of Texas, Austin, Texas.

Grane, F.E. and Gardner, G.H.F. 1961. Measurements of Transverse Dispersion in Granular Media. *J. Chem. Eng. Data* **6** (2): 283–287.

Greenkorn, A.R. 1983. *Flow Phenomena in Porous Media*. New York City: Marcel Decker, Inc.

Haajizadeh, M., Fayers, F.J. and Cockin, A.P. 2000. Effects of Phase Behavior, Dispersion and Girding on Sweep Patterns for Nearly Miscible Gas Displacement. Paper SPE 62995 presented at the SPE Annual Technical Conference and Exhibition, Dallas, TX.

Haajizadeh, M., Fayers, F.J., Cockin, A.P. and Bond, D.J. 1999. On the Importance of Dispersion and Heterogeneity in the Compositional Simulation of Miscible Gas Processes. Paper SPE 57256 presented at the SPE Asia Pacific Improved Oil Recovery Conference, Kuala Lumpur, Malaysia.

Heller, J. P. 1972. Observations of Mixing and Diffusion in Porous Media. Paper presented at the International Symposium on Fundamentals of Transport Phenomena in Porous Media, Guelph University, Ontario.

Hui, M.H., Zhou, D., Wen, X.H. and Durlofsky, L.J. 2005. Development and Application of a New Technique for Upscaling Miscible Processes. *SPEREE* **8** (3): 189-195.

Hulin, J.P. and Plona, T.J. 1989. Echo Tracer Dispersion in Porous Media. *Physics of Fluids* **1** (8): 1341-1347.

Javandel, I., Doughty, C., and Tsang, C.F. 1984. *Groundwater Transport: Handbook of Mathematical Models*, No. 10. Washington, DC: Water Resources Monograph, American Geophysical Union.

Jennings, J.W., Ruppel, S.C. and Ward, W.B. 2000. Geostatistical Analysis of Permeability Data and Modeling of Fluid-Flow Effects in Carbonate Outcrops. *SPEREE* **3** (4): 292-303. SPE-65370-PA.

Jensen, J.L., Lake, L.W., Corbett, P.W.M. and Goggin, D.J. 2000. *Statistics for Petroleum Engineers and Geoscientists*. New Jersey: Prentice Hall PTR.

Jerauld, G.R. 1998. A Case Study in Scale-up for Multicontact Miscible Hydrocarbon Gas Injection. *SPEREE* **1**(6):575-582. SPE-53006-PA.

Jessen, K., Stenby, E.H. and Orr, F.M. 2002. Interplay of Phase Behavior and Numerical Dispersion in Finite Difference Compositional Simulation. Paper SPE 75134 presented at the SPE/DOE Symposium on Improved Oil Recovery, Tulsa, OK.

Jha, R.K. 2008. Investigation of Local Mixing and Its Influence on Core Scale Mixing (Dispersion). PhD dissertation, University of Texas, Austin, Texas.

Jha, R.K., Bryant, S.L., Lake, L.W. and John, A.K. 2006. Investigation of Pore-Scale (Local) Mixing. Paper SPE 99782 presented at the SPE Improved Oil Recovery Symposium, Tulsa, OK.

Jha, R.K., John, A., Bryant, S.L. and Lake, L.W. 2006. Flow Reversal and Mixing. Paper SPE 103054 presented at the SPE Annual Technical Conference and Exhibition, San Antonio, TX.

John, A.K. 2008. Dispersion in Large Scale Permeable Media. PhD dissertation, University of Texas, Austin, Texas.

John, A.K., Lake, L.W., Bryant, S.L., and Jennings, J.W. 2008. Investigation of Field Scale Dispersion. Paper SPE-113429 presented at the SPE/DOE Improved Oil Recovery Symposium, Tulsa, OK.

Johns, R.T., Fayers, F.J., and Orr, F.M. 1994. Effect of Gas Enrichment and Dispersion on Nearly Miscible Displacements in Condensing/Vaporizing Drives. *SPE Advanced Technology Series* **2** (2): 26–34. SPE-24938-PA.

Johns, R.T., Pashupati, S., and Subramanian, S.K. 2000. Effect of Gas Enrichment Above the MME on Oil Recovery in Enriched-Gas Floods. *SPEJ* **5** (3): 331–338. SPE-65704-PA.

Johns, R.T., Sah, P., and Solano, R. 2002. Effect of Dispersion on Local Displacement Efficiency for Multicomponent Enriched-Gas Floods Above the Minimum Miscibility Enrichment. *SPEREE* **5** (1): 4–10. SPE-75806-PA.

Jose, S.C., Rahman, M.A. and Cirpka, O.A. 2004. Large-Scale Sandbox Experiment on Longitudinal Effective Dispersion in Heterogeneous Porous Media. *Water Resources Research* **40** (12)**:** W12415.

Khaleed, R., JimYeh, T.C. and Lu, Z. 2002. Upscaled Flow and Transport Properties for Heterogeneous Unsaturated Media. *Water Resource Research* **38** (5): 1-12.

King, M.J., MacDonald, D.G., Todd, S.P., Leung. 1998. Application of Novel Upscaling Approaches to the Magnus and Andrew Reservoirs. Paper SPE 50643 presented at the SPE European petroleum Conference, Netherland.

Kitanidis, P. K. 1992. Analysis of Macrodispersion through Volume-Averaging: Moment Equations. *Stochastic Hydrology and Hydraulics* **6**:5-25.

Kitanidis, P.K. 1990. Effective Hydraulic Conductivity for Gradually Varying Flow. *Water Resource Research* **26** (6):1197-1208.

Kitanidis, P.K. 1994. The Concept of the Dilution Index. *Water Resources Research* **30** (7): 2011-2026.

Klinkenberg, L.J. 1951. Analog Between Diffusion and Electrical Conductivity in Porous Rocks. *Bull. GSA* **62,** 559.

Koch, D.L. and Brady, J.F. 1987. A Non-Local Description of Advection Diffusion with Application to Dispersion in Porous Media. *Journal of Fluid Mechanics* **180**: 387-403.

Koch, D.L. and Brady, J.F. 1987. Nonlocal Dispersion in Porous Media: Nonmechanical Effects. *Chemical Engineering Science* **42** (6): 1377-1392.

Lake, L.W. 1989. *Enhanced Oil Recovery*. Englewood Cliffs, New Jersey: Prentice Hall.

Lake, L.W. and Hirasaki, G.J. 1981. Taylor's Dispersion in Stratified Porous Media. *SPEJ* **21** (4): 459–468. SPE-8436-PA.

Lantz, R.B. 1971. Qualitative Evaluation of Numerical Diffusion (Truncation Error). *SPEJ* **11** (3):315-320; *Trans.,* AIME, **251**. SPE-2811-PA.

Leroy, C., Hulin, J.P. and Lenormand, R. 1992. Tracer Dispersion in Stratified Porous Media: Influence of Transverse Dispersion and Gravity. *Journal of Contaminant Hydrology* **11** (1-2): 51-68.

Mahadevan, J., Lake, L.W. and Johns, R.T. 2003. Estimation of True Dispersivity in Field-Scale Permeable Media. *SPEJ* **8** (3): 272–279. SPE-86303-PA.

Majoros, S. and Deans, H.A. 1980. Single-Well Chemical Tracer Tests Since 1968. Topical Report, U.S. Department of Energy, OK.

Moulds, T.P., McGuire, P.L., Jerauld, G.R., Lee, S.T. and Solano, R. 2005. Pt. McIntyre: A Case Study of Gas Enrichment Above MME. *SPEREE* **8** (3): 182-188. SPE-84185-PA.

Myers, R.H., and Montgomery, C.D. 1995. *Response Surface Methodology: Process and Product Optimization Using Designed Experiments*. New York: John Wiley and Sons.

Pande, K.K. and Orr, F.M. 1989. Interaction of Phase Behavior, Reservoir Heterogeneity and Crossflow in Co_2 Floods. Paper SPE 19668 presented at the SPE Annual Technical and Conference and Exhibition, San Antonio, TX.

Peaceman, D.W. 1977. *Fundamentals of Numerical Reservoir Simulation*. Elsevier Scientific Publishing Company: New York.

Peaceman, D.W., and Rachford, H.H. Jr. 1962. Numerical Calculation of Multidimensional Miscible Displacement. *SPEJ* **2**(4):327-339.

Peaudecerf, P. and Sauty J.P. 1978. Application of the Mathematical Model to Characterization of Dispersion Effect of Groundwater Quality. *Prog. Water Tech.* **10** (5): 443-454.

Perkins, T.K. and Johnston, O.C. 1963. A Review of Diffusion and Dispersion in Porous Media. *SPEJ* **3** (1): 70–84; *Trans.,* AIME, **228**. SPE-480-PA.

Pickens, J.F. and Grisak, G.E. 1981a. Scale-Dependent Dispersion in a Stratified Granular Aquifer. *Water Resources Research* **17** (4): 1191–1211.

Pickens, J.F. and Grisak, G.E. 1981b. Modeling of Scale-Dependent Dispersion in Hydrogeologic Systems. *Water Resources Research* **17** (6): 1701–1711.

Plumb, O.A. and Whitaker, S. 1988. Dispersion in Heterogeneous Porous Media. 1. Local Volume Averaging and Large-Scale Averaging. *Water Resources Research* **24** (7): 913-926.

Price, H.S., Cavendish, J.S., and Varga, R.S. 1968. Numerical Methods of Higher-Order Accuracy for Diffusion-Convection Equations. *SPEJ* **8**(3):293-303.

Rehfeldt, K.R. and Gelhar, L.W. 1992. Stochastic Analysis of Dispersion in Unsteady Flow in Heterogeneous Aquifers. *Water Resource Research* **28** (8): 2085-2099.

Rehfeldt, K.R., and Gelhar, L.W. 1992. Stochastic Analysis of Dispersion in Unsteady Flow in Heterogeneous Aquifers. *Water Resource Research* **28** (8): 2085-2099.

Rhodes, M.E., Bijeljic, B. and Blunt, M.J. 2007. A Rigorous Pore-to-Field-Scale Simulation Methodology for Single-Phase Flow Based on Continuous Time Random Walks. Paper SPE 10634 presented at the SPE Reservoir Simulation Symposium, Houston, TX.

Riazi, M.R. and Whitson, C.H. 1993. Estimating Diffusion Coefficients of Dense Fluids. *Industrial and Engineering Chemistry Research* **32**: 3081-3088.

Rigord, P., Calvo, A. and Hulin, J.P. 1990. Transition to Irreversibility for the Dispersion of a Tracer in Porous Media. *Physics of Fluids* **2** (5): 681-687.

Rubin, Y. 2003. *Applied Stochastic Hydrogeology*. New York: Oxford University Press.

Rubin, Y., Sun, A., Maxwell, R. and Bellin, A. 1999. The Concept of Block Effective Macro-Dispersivity and a Unified Approach for Grid-scale- and Plume-scale- dependent Transport. *J. Fluid Mechanic* **395**: 691-701.

Sahimi, M., Heiba, A.A., Hughes, B.D., Davis, H.T. and Scriven, L.E. 1982. Dispersion in Flow Through Porous Media. Paper SPE 10969 presented at the SPE Annual Technical Conference and Exhibition, New Orleans, LA.

Schwartz, F.W. 1977. Macroscopic Dispersion in Porous Media: The Controlling Factors. *Water Resources Research* **13** (4): 743-752.

Shook, M., Lake, L.W. and Li, D. 1992. Scaling Immiscible Flow Through Permeable Media by Inspectional Analysis. *In Situ* 16 (4): 311-349.

Sigmund, P.M. 1976. Prediction of Molecular Diffusion at Reservoir Conditions. Part I—Measurement and Prediction of Binary Dense Gas Diffusion Coefficients. *Journal of Canadian Petroleum Technology*, April-June: 48–57.

Smith L. and Schwartz F.W. 1980. Mass Transport 1. A Stochastic Analysis of Macroscopic Dispersion. *Water Resources Research* **16:**303-313.

Solano, R., Johns, R.T., and Lake, L.W. 2001. Impact of Reservoir Mixing on Recovery in Enriched-Gas Drives Above the Minimum Miscibility Enrichment. *SPEREE* **4** (5): 358–365. SPE-73829-PA.

Sorbie, K.S. and Clifford, P.J. 1991. The Inclusion of Molecular Diffusion Effects in the Network Modeling of Hydrodynamic Dispersion in Porous Media. *Chemical Engineering Science* **46** (10): 2525-2542.

Sorbie, K.S. and Tomlinson, C.J. 1993. Analytical Method for Evaluating the Effective Molecular Diffusion Coefficient within Porous Media. *Chemical Engineering Science* **48** (10): 1813-1818.

Stalkup, F. 1998. Predicting the Effect of Continued Gas Enrichment Above the MME on Oil Recovery in Enriched Hydrocarbon Gas Floods. Paper SPE 48949 presented at the SPE Annual Technical Conference and Exhibition, New Orleans, LA.

Stalkup, F.I. 1990. Effect of Gas Enrichment and Numerical Dispersion on Enriched-Gas Drive Predictions. *SPERE* **5** (4):647-655. SPE-18060-PA.

Sternberg, S. 2004. Dispersion Measurements in Highly Heterogeneous Laboratory Scale Porous Media. *Transport in Porous Media* **54** (1): 107–124.

Sternberg, S., Cushman, J.H., and Greenkorn, R.A. 1996. Laboratory Observation of Nonlocal Dispersion. *Transport in Porous Media* **23** (2): 135–151.

Sternberg, S.P.K. and Greenkorn, R.A. 1994. An Experimental Investigation of Dispersion in Layered Porous Media. *Transport in Porous Media* **15** (1): 15–30.

Su, N., Sander, G.C., Liu, F., Anh, V., Barry, D.A. 2005. Similarity Solutions for Solute Transport in Fractal Porous Media Using a Time and Scale Dependent Dispersivity. *Applied Mathematical Modeling* **29**: 852-870.

Sudicky E.A. and J.A. Cherry. 1979. Field Observations of Tracer Dispersion Under Natural Flow Conditions in an Unconfined Sandy Aquifer. *Water Polu. Res. Can.* **14** : 1-17.

Taylor, G.I. 1922. Diffusion by Continuous Movements. *Proceedings of the London Mathematical Society, series 2,* **20**: 196-212.

Taylor, G.I. 1953. Dispersion of Soluble Matter in Solvent Flowing Slowly Through a Tube. *Proceedings of the Royal Society of London, Series A: Mathematical and Physical Sciences* **219**: 186-203.

Theodoropoulou, M.A., Karoutsos, V., Kaspiris, C., Tsakiroglou, C.D. 2003. A New Visualization Technique for the Study of Solute Dispersion in Model Porous Media. *Journal of Hydrology* **274** (1-4): 176-197.

Van Gulijk, C. 1998. Using Computational Fluid Dynamics to Calculate Transversal Dispersion in a Structured Packed Bed. *Computers & Chemical Engineering* **22** (S1): S767-S770.

Wallstrom, T.C., Christie, M.A., Durlofsky, L.J., Sharp, D.H. 2002. Effective flux boundary conditions for upscaling porous media equations. *Transport in Porous Media* **46** (2-3): 139-153.

Walsh, B.W. and Orr, F.M. 1990. Prediction of Miscible Flood Performance: The Effect of Dispersion on Composition Paths in Ternary Systems. *In Situ* **14** (1): 19–47.

Webster, I.T. and Taylor, J.H. 1992. Rotational Dispersion in Porous Media Due to Fluctuating Flows. *Water Resource Research* **28** (1):109-119.

Wen, X.H, Chen, Y., Durlofsky, L.J. 2006. Efficient 3D implementation of local-global upscaling for reservoir simulation. *SPEJ* **11** (4): 443-453.

Wen, X.H., Durlofsky, L.J., Edwards, M.G. 2003. Upscaling of channel systems in two dimensions using flow-based grids. *Transport in Porous Media* **51** (3): 343-366.

Wheatcraft, S.W. and Tyler, S.W. 1988. An Explanation of Scale-Dependent Dispersivity in Heterogeneous Aquifers Using Concepts of Fractal Geometry. *Water Resources Research* **24**(4):566-578.

Whitaker, S. 1999. *The Method of Volume Averaging*. Dordrecht, The Netherlands: Theory and Applications of Transport in Porous Media, Kluwer Academic Publishers.

Wilke, C.R. and Chang, P. 1955. Correlation of Diffusion Coefficients in Dilute Solutions. *AIChE Journal* **1** (2): 264-270.

Wood, D.J., Lake, L.W., Johns, R.T. and Nunez, V. 2006. A Screening Model for CO2 Flooding and Storage in Gulf Coast Reservoirs Based on Dimensionless Groups. Paper SPE-100021 presented at the SPE/DOE Symposium on Improved Oil Recovery, Tulsa, Ok.

Vita

Gholamreza Garmeh was born in Bojnourd, Iran on April 9, 1980, son of Mr. R. Garmeh and Mrs. R. Soldouzi. After completing his high school education at I.H.M. pre-university, Bojnourd, Iran, in 1998, he entered the Petroleum University of Technology, Ahwaz, Iran. He received the degree of Bachelor of Science in Petroleum Engineering from P.U.T, Ahwaz, Iran, in May 2002. In September 2003, he entered The Graduate School at The University of Texas at Austin. In August 2005 he received his MS in Petroleum Engineering and subsequently he started his Ph.D. program.

Permanent Address: 12 Summar ave. 17 Shahrivar st.
Bojnourd, 94519
Iran

This dissertation was typed by the author.